Charge Transfer and Catalysis at the Metal–Support Interface

By

Lawrence Robert Baker

A dissertation submitted in partial satisfaction of the

requirements for the degree of

Doctor of Philosophy

in

Chemistry

in the

Graduate Division

of the

University of California, Berkeley

Committee in charge:

Professor Gabor A. Somorjai, Chair
Professor Martin Head–Gordon
Professor Peidong Yang
Professor Jeffrey Bokor

Fall 2012

Abstract

Charge Transfer and Catalysis at the Metal–Support Interface

by

Lawrence Robert Baker

Doctor of Philosophy in Chemistry

University of California, Berkeley

Professor Gabor A. Somorjai, Chair

Kinetic, electronic, and spectroscopic characterization of model Pt–support systems are used to demonstrate the relationship between charge transfer and catalytic activity and selectivity. The results show that charge flow controls the activity and selectivity of supported metal catalysts.

Using a Pt/n-Si Schottky junction, it is possible to externally control the electronic properties at the Pt/Si interface by applying bias or by exciting charge carriers with visible light. It is found that this device can control the rate of CO oxidation on Pt. Results show that negative charge on the Pt increases the reaction rate while positive charge on the Pt decreases the reaction rate. This is the first time that a solid-state device has been used to externally control the rate of a chemical reaction as determined by directly measuring the product yield. Similar experiments were performed for the H_2 oxidation reaction and analogous results were obtained.

Similarly, electronic control of catalyst performance can be achieved by substrate doping. It is shown that F doping can tune the electronic structure of TiO_2. When F is incorporated into TiO_2, the electrical conductivity is dramatically enhanced because F acts as an n-type dopant. It is shown that this highly n-type TiO_2 acts as an electronically active support for Pt catalysts, increasing the rate of CO oxidation by electronically activating surface O. It is further shown that for a multipath reaction, the electronic structure of TiO_2 also controls the reaction selectivity. The electronic activity of highly n-type TiO_2 serving as a Pt support for methanol oxidation selectively enhances the production of formaldehyde relative to CO_2.

Finally, sum frequency generation (SFG) vibrational spectroscopy is used to probe the molecular nature of strong metal–support interactions (SMSI). This is the first time that SFG has been used to probe the highly selective oxide–metal interface during catalytic reaction, and the results demonstrate that charge transfer from TiO_2 on a Pt/TiO_2 catalyst controls the product distribution of furfuraldehyde hydrogenation by an acid–base mechanism. SFG spectra reveal that a furfuryl-oxy intermediate forms on TiO_2 as a result of a charge transfer interaction. This furfuryl-oxy intermediate is a highly active and selective precursor to furfuryl alcohol, and spectral analysis shows that the Pt/TiO_2 interface is required primarily for H spillover. Density functional calculations predict that O-vacancies on the TiO_2 surface activate the formation of the furfuryl-oxy intermediate via an electron transfer to furfuraldehyde, drawing a strong analogy between SMSI and acid–base catalysis.

This dissertation builds on extensive existing knowledge of metal–support interactions in heterogeneous catalysis. The results show the prominent role of charge transfer at catalytic interfaces to determine catalytic activity and selectivity. Further, this research demonstrates the possibility of selectively driving catalytic chemistry by controlling charge flow and presents solid-state devices and doped supports as novel methods for obtaining electronic control over catalytic reaction kinetics.

Table of Contents

Acknowledgements

This research was supported by the U.S. Department of Energy, Office of Basic Energy Sciences, under Contract No. DE-AC02-05CH11231. I am grateful for this funding source and hope that continued scientific funding will be available for the important challenges of the future pertaining to renewable energy and energy conversion chemistry.

I am deeply grateful to the many individuals who have contributed to my education and who have supported me during an amazing experience in Berkeley. My experiences have far exceeded my most optimistic expectations when I moved here four years ago with my family, and it is a result of the very good people that have surrounded me.

I am grateful to Gabor Somorjai. In my first interactions with him, he radiated an influence that enthused me with a love for the research that we have shared, and this has motivated every choice and accomplishment since those early conversations. Following my first meeting with him during my site visit to Berkeley, I was so excited to join his research group that I kept a copy of C&EN News showing his picture on the cover with me constantly. Since that time he has taught me much about how to be a good chemist, a good mentor, and a good husband and father, and my life will be much better because of what I have learned from him. He once told me that in life, security multiplied by opportunity equals a constant, meaning that we can only increase our opportunities by sacrificing our security. However, he has raised the value of this constant significantly in my life and in the lives of numerous other students, and he is one of the great mentors that I aspire to emulate.

I am grateful to Inger who has taken good care of me. If Gabor is my scientific father, then Inger is my scientific mother. I remember shortly after coming to Berkeley, my wife, Catherine, was expecting our second child. I tried to obtain a parking permit at LBNL so that I could come home quickly when Catherine started labor. However, the badge office would not issue the permit, and I found myself in trouble when I responded disputatiously. Of course Inger calmed this storm and with her and Gabor's help, I received a permit. I have always been pleased to think that she is proud of my accomplishments, and I know that it was on the basis of her nomination that I received the Benjamin Boussert Award.

I am grateful to my lab partners, and I have learned much from my interactions with each one. Almost my entire Ph.D. experience has been spent in close work with Antoine Hervier. To me he is much more than a bright chemist; he is an honest friend. Our early experiences working together to use a catalytic photodiode to control the rate of H_2 oxidation is one of the fun memories of my Ph.D. I will always remember sitting with him at the computer anxiously watching as each data point confirmed or disproved our anticipated breakthrough. Griffin Kennedy is another lab partner whose contributions to our project have been invaluable. I will always be glad that he chose to join our project following our acquaintance in Chem 125. He is a talented student with a bright future and a good friend, and I am grateful for my close association with him. There have been many others with whom it has been a privilege to work. Getting to know each member of the Somorjai Group and learning their personal motivations for studying science has broadened my perspective and given me many worthy examples to follow.

I am most grateful to my family. When Catherine, Eliza, and I moved to Berkeley, we could not have anticipated the experiences we have had. During our time here, we have been joined by Stephen and Beth. I have loved each moment with this family, and they are my treasures. I hope that my hard work in this program will represent a good example to my children and that they will also be blessed to love learning as I have loved it. I am also grateful to my Mom and Dad and my siblings, Lyndsay, Ryan, Quinn, Luke, Spencer, and Brooke. My desire to honor them has been my motivation.

Chapter 1

Introduction

1.1 Background and Motivation

The first known commercialization of a catalyst came in the form of the Dobereiner lamp. This early household device consisted of a bottle of zinc metal in sulfuric acid to produce hydrogen. A platinum catalyst was located at the bottle's outlet. When the bottle was opened, the platinum would ignite the pressurized hydrogen to produce a small flame. Used as a kitchen lighter, this lamp was invented by Johann Wolfgang Dobereiner in 1823 at the University of Jena in Germany and remained in commercialization for about 60 years. The term "catalysis" was not used until 13 years after Dobereiner's invention, when the Swedish chemist, Jons Jacob Berzelius, observed that certain substances accelerate the rate of a reaction while themselves, remaining unchanged. To describe this phenomenon, Berzelius coined the term catalysis from the Greek word "καταλύειν," meaning to untie.

Since Dobereiner's invention almost two centuries ago, catalysis has become a $900 billion per year industry. Catalysis is used in processes as remote as the catalytic converter that reduces harmful emissions from automobiles to the synthesis of ammonia using the Haber process. It is clear that the quality of living would be dramatically different without catalysis. For example, the world's present population is largely sustained by agriculture enhanced by fertilizers synthesized using the Haber process. It is estimated that without the ability to catalyze ammonia synthesis, the present global population would be cut in half. Currently 90% of all commercially produced chemical products rely on catalysis in some form.

There currently exists an economic and environmental need to develop catalysts for chemical energy conversion toward the goal of alternative fuels and renewable energy. Development of catalytic processes for chemical energy conversion from renewable sources is proving to be one of the most pressing and challenging issues for modern science. At the heart of energy conversion is the correlation between charge flow and chemistry. At present, several processes exist that can convert a chemical reaction to a net charge flow (e.g., fuel cells and batteries) or that can use a charge flow to drive a chemical reaction (e.g., electrochemistry, photochemistry, and acid–base catalysis). However, it is clear that the efficiency and stability of these processes require improvement to meet the existing energy demand or that novel energy conversion processes will need to be developed. This has been the goal of the Helios Solar Energy Research Center which originally funded my research. Recently, Helios has been replaced by the Joint Center for Artificial Photosynthesis. Both of these initiatives are supported by the Department of Energy, Office of Basic Energy Sciences. A fundamental understanding of the correlation between charge flow and catalysis, as well as the ability to control charge flow to drive a chemical reaction, is key to the success of these projects, and this has been the motivation of my Ph.D. research.

1.2 Nanoscience and Heterogeneous Catalysis

Heterogeneous catalysis describes chemical reactions that occur on surfaces and, together with homogeneous and enzyme catalysis, composes one of the three major branches of catalysis science. The study of heterogeneous catalysis is closely linked with the evolution of surface science, because the correlation of surface structure with catalytic activity originally formed the foundation of this field.[1] Although some catalytic reactions are structure insensitive, many reactions depend strongly on the surface structure of the catalyst.[2] By studying catalytic reactions on single crystal model catalysts, it was discovered that low coordination sites occurring at step edges, kinks, and defects, are often more active than other highly coordinated surface sites.[3] A few examples of structure sensitive reactions include H_2–D_2 exchange on Pt,[4-6] furan and crotonaldehyde hydrogenation on Pt,[7,8] CO oxidation on Pt,[9] ammonia synthesis on Fe,[10] and CO hydrogenation on Ni.[11]

For single crystal model catalysts, the crystal face determines the surface structure. However, for nanoparticle catalysts, the relative concentration of step edges and kink sites depends on particle size and shape. Traditional methods for catalyst preparation (i.e. incipient wetness and ion exchange) use the reduction of a metal salt inside of a mesoporous oxide.[12,13] The result is a catalyst consisting of metal particles with a broad distribution of sizes and morphologies. This type of polydisperse heterogeneous catalyst masks the structure sensitivity inherent in heterogeneous catalysis because of the impossibility of selecting nanoparticles of a single size or shape. Recent advances in nanoscience have shown that colloidal synthetic methods can produce monodisperse nanoparticles with well-defined sizes and shapes.[14-18] This advance has marked a new era in heterogeneous catalysis where monodisperse nanoparticles are used as model catalysts.[19-21] The results of these studies show that nanoparticle size and shape control the catalytic activity and selectivity for many reactions.[22-27]

In colloidal synthetic methods, nanoparticles are necessarily encapsulated by an organic polymer or surfactant. This capping agent lowers the surface energy of the nanoparticle to prevent aggregation of the particles;[18] the cap may also help to control the size and shape of the nanoparticles.[28] This gives rise to an important question regarding the effect of the capping agent on the catalytic properties of the encapsulated nanoparticles. It is traditionally thought that the cap acts as a site blocking agent and lowers the metal surface area available for catalytic reaction.[29] In this light, it has been assumed that colloidal preparation methods are impractical for catalytic applications because the presence of the organic cap decreases the apparent metal dispersion. However, this is an incomplete assumption that considers the cap as a passive coating rather than a dynamic shell that restructures depending on reaction conditions. This work demonstrates that for certain reactions a capped nanoparticle is more active than its uncapped analog owing to reversible restructuring of carbonaceous material in various gas environments. When the capping layer is removed from a nanoparticle, the cap is replaced by a stable carbonaceous shell. This shell reversibly adopts an open, porous structure in H_2 and a closed, impermeable structure in O_2. Consequently, a capped nanoparticle is a more active catalyst for oxidation chemistry because the capping layer prevents formation of a deactivating carbonaceous deposit. This use of capping agents to control catalytic activity of a nanoparticle is reminiscent of homogeneous catalysis where ligands are used to tune the catalytic properties of single metal ions.[30]

1.3 Strong Metal–Support Interactions (SMSI)

1.3.1 Definitions of SMSI

Although metals alone are often catalytically active, most catalysts consist of metal particles supported on a porous oxide. This not only provides a high surface area for the heterogeneous catalyst, but as shown by many studies, the oxide support plays an important role in determining the activity and selectivity of the catalyst.[31-34] This phenomenon, known as the strong metal–support interaction (SMSI), has been widely studied and is an important topic in both science and industry. The term SMSI was first used by Tauster and Fung to refer to the dramatic reduction in chemisorption sites observed for noble metal catalysts supported on titanium oxide.[32] In their studies, Tauster and Fung showed evidence for a strong bonding interaction between metal nanoparticles and a reduced titanium oxide support, and they used the term SMSI to refer directly to this bonding interaction.[34] However, because this metal–support interaction is closely linked to the catalytic behavior of the metal involved, the definition of SMSI has since expanded to broadly refer to support-induced changes in the catalytic activity and selectivity of metal nanoparticles. In this work, the term SMSI refers to the ability of an inert support to mediate catalytic behavior of a metal without specific attention to bonding at the metal–support interface.

SMSI is known to play an important role in many catalytic reactions, including CO oxidation,[35-39] CO and CO_2 hydrogenation,[40,41] hydroformulation,[42] and partial hydrogenation reactions.[43-47] The catalyst support also plays an important role in activating molecular oxygen for selective partial oxidation reactions. Industrially relevant examples include the synthesis of aldehydes from primary alcohols,[48] the production of hydrogen peroxide from hydrogen,[49-53] and the conversion of methane to synthesis gas.[54-56] In these cases, molecular oxygen is preferred over other oxygen donors due to cost, energy efficiency, and environmental concerns.[48,56]

1.3.2 Mechanisms of SMSI

Several proposed mechanism exist to explain the role of an oxide to mediate the catalytic behavior of a supported metal nanoparticle. Because SMSI broadly refers a wide variety of experimental observations, these mechanisms are not mutually exclusive and each focuses on explaining a slightly different observation related to supported metal catalysts. Together, these observations describe a complex series of interactions showing how the metal–support interface can strongly influence surface chemistry and selectively amplify specific reaction pathways. The majority of proposed mechanisms for metal–support interactions fall into one of the following categories: 1) formation of active sites when the support wets (or decorates) the metal particle,[57,58] 2) activation and spillover from chemically active sites in the support,[59] and 3) electronic mediation through various forms of charge transfer.[37,60]

The concept that an oxide support could diffuse onto and eventually encapsulate a metal nanoparticle was first suggested to explain the loss of chemisorption sites when metal catalysts supported on reducible oxides were heated in H_2. Tauster and Fung showed that after reduction of a metal catalyst supported on titanium oxide at 773 K, H_2 and CO chemisorption decreased to nearly zero for Ru, Rh, Pd, Os, Ir, and Pt.[32] This was not a result of a structural collapse of the porous oxide support as the total surface area remained unchanged and the effect was reversible by oxidizing treatments. Baker et al. first showed by transmission electron microscopy (TEM)

that following reduction treatments, titanium oxide migrated over the metal surface in a way that would block metal sites from chemisorbing H_2 or CO.[61] Komaya et al. showed by TEM that as the reduction temperature increased, the coverage of titanium oxide on the metal catalyst increased resulting in total encapsulation by 773 K.[62] With continuously improving TEM resolution, evidence for metal encapsulation by a reduced support has become unquestionable.[63]

Although metal decoration by an oxide support can explain the loss of apparent metal surface area as measured by chemisorption experiments, it falls short of explaining how the oxide mediates the catalytic activity of the supported or encapsulated metal catalyst. A series of experiments by Boffa et al. are insightful for understanding how metal decoration by an oxide affects the surface catalytic reaction.[40,41] In these experiments, various oxides were deposited onto a Rh foil. This geometry with oxide islands on a planar metal support is referred to as an inverse catalyst and allows a high degree of control over the oxide–metal interface. Because the surface energy of the oxide is lower than the Rh, the oxide layer grows as a single monolayer islands on the metal without any multilayer formation until 95% surface coverage. This preparation method allows for precise control of the relative concentration of oxide and metal surface sites compared with previous SMSI catalysts prepared by high temperature reduction.

Assuming that the metal sites are catalytically active and that the oxide sites are not, linear deactivation of the Rh is expected with increasing oxide coverage. This is the case for the ethylene hydrogenation reaction. However, for CO and CO_2 hydrogenation reactions, a >10-fold rate enhancement occurs as the Rh metal is decorated with oxide islands. This rate enhancement reaches a maximum at 50% oxide coverage, suggesting that oxide–metal interface sites occurring at the perimeter of the oxide islands are orders of magnitude more active than the metal alone. By correlating the maximum rate enhancement with the Lewis acidity of the deposited oxide, Boffa hypothesized that a Lewis acid–base interaction of CO and CO_2 with the oxide is responsible for carbonyl bond activation. This idea of bond activation at the oxide–metal interface, coupled with the concept of metal decoration by a reduced oxide, shows one method by which an oxide support can mediate the catalytic properties of a metal nanoparticle.

Because adsorption energies of molecules can differ substantially between metals and oxides, the oxide–metal interface can also bring together reactants that would not co-adsorb on either an oxide or a metal alone. An example of this is found in the CO oxidation reaction on Pt. On Pt single crystals the activation energy of CO oxidation is as high as 42 kcal/mol, corresponding with the high heat of CO adsorption.[64,65] This indicates that the Pt surface is predominately CO covered and that the rate limiting step is desorption of CO to allow O_2 adsorption and dissociation. However, O_2 adsorption is much more competitive on oxides than on Pt. Consequently, for Pt supported on certain oxides, the Pt may be predominately CO covered while the oxide is predominately O covered. This means that at the metal–support interface the reaction proceeds without the need for CO desorption, and the activation energy is much lower than on a bulk Pt catalyst.[66,67]

Additionally, once adsorbed on one site, many reactants can migrate across the oxide–metal interface.[68] For example, H_2 will not dissociate on most oxide surfaces but will actively dissociate on many metals, including Pt.[69] Consequently, in the presence of small amounts of Pt, oxides can be permeated with atomic H as a result of dissociation on the Pt followed by migration across the Pt–support interface.[62] This allows the reaction of atomic H with any molecule preferentially adsorbed on the oxide support, and gives rise to reaction pathways that

do not exist on either the pure Pt or the pure oxide. Results presented in this work show that specific adsorption modes of aldehyde molecules on titanium oxide activate the carbonyl bond for selective hydrogenation which occurs via the spillover of atomic H from supported Pt. Consequently, Pt supported on titanium oxide is highly selective for formation of unsaturated alcohols from aldehydes, while Pt supported on silicon oxide is not active at all for this reaction pathway.

Previous studies have indicated that, at least in certain instances, catalytic oxidation reactions proceed by an electronically activated pathway.[70-75] Bonn et al.[70] showed that for CO oxidation on Ru, the activation of chemisorbed O occurs by charge transfer from the metal to form an active O^- intermediate. Because the active O^- species cannot form thermally until well above the desorption temperature of CO, a temperature ramp of a CO/O_2 co-adsorbed Ru surface produces CO and O_2, but not CO_2. However, a femtosecond laser pulse can produce very high electronic temperatures on the short time scale without significant lattice heating. This serves to electronically activate O without thermally desorbing CO, resulting in CO_2 formation. Although fundamentally insightful, this type of experiment employing a femtosecond laser cannot be scaled for high turnover applications. The research presented here shows that similar electronic O activation also occurs by electron spillover from a highly n-type catalyst support.[39,76,77] These results demonstrate the electronic nature of SMSI as well as the utility of metal–support interactions to electronically control the activity and selectivity of oxidation catalysts. In this work, it is also shown that non-thermal control of catalytic surface chemistry is possible by externally controlling the electronic structure at a metal–support interface using a solid-state charge-based device.[78]

1.4 Acid–Base Catalysis

Like SMSI, acid–base catalysis is often characterized by the selective enhancement of a single reaction pathway. This is because in acid–base catalysis, the generation of ionic reaction intermediates determines the reaction rate and selectivity, and the charged intermediate is often highly active for a specific pathway.[79-81] In the case of acid catalysis, charge is transferred to an organic molecule, usually by H^+ addition or H^- abstraction.[82] Bronsted acids work by H^+ addition and result in formation of a carbonium ion (i.e., a carbocation with a five-fold conjugation), while Lewis acids work by H^- abstraction and result in the formation of a carbenium ion (i.e., a carbocation with a three-fold conjugation). Scheme 1 depicts CH^{5+} and CH^{3+}, the simplest carbonium and carbenium ions, respectively. Typically carbonium ions quickly convert to carbenium ions by the evolution of molecular hydrogen. Consequently, H_2 evolution has been taken as a signature of Bronsted acidity, and this results in a stoichiometric, rather than catalytic, reaction unless H_2 is present to replenish the acidic sites. Because of the active nature of the resulting carbocations, strong acids are catalysts for isomerization,[83] alkylation,[84,85] polymerization,[86,87] and carbonylation[88] reactions.

The term superacid was first coined to describe the properties of SbF_5 in $HFSO_3$, and a superacid is defined as a material whose acidic strength is greater than 100% sulfuric acid.[89] Typically a pK_a value is used to describe the strength of an acid, where pK_a is simply proportional to the Gibbs free energy of change of a proton transfer. However, fundamentally pK_a does not exactly describe the strength of an acid; instead it describes the strength of an acid relative to a specific proton acceptor, meaning it quantifies the energetics of an acid–base

interaction. Because the base in the acid–base pair is always water for aqueous acids, the pK_a scale is useful for comparing the strength of typical aqueous acids. However, in acid catalysis, the reactant molecule acts as the proton acceptor. This means that acid catalysis requires an acid with sufficient strength to protonate the hydrocarbon reactant. Consequently, the pK_a scale breaks down for superacids because water will necessarily limit the activity of a superacid by replacing the reactant as the proton acceptor. Instead of pK_a, the Hammett acidity function (H_o) represents a measure of acidic strength for superacids, and this method relies on the use of aromatic nitro compounds as indicators.[90,91] However, there is still no way to directly measure the energetics of charge transfer in acid catalysis.

Carbonium Ion ***Carbenium Ion***

Scheme 1

The first superacids studied were anhydrous liquids. Addition of a strong Lewis acid such as SbF_5 to Bronsted acids like H_2SO_4 or $HFSO_3$ increases their acidic strength dramatically. This is because the SbF_5 destabilizes the proton on the Bronsted acid by an electron withdrawing interaction. The acidic strength of these mixed Lewis–Bronsted acids is sufficiently high to protonate hydrocarbons, and in these acids, carbocations are stable and have been observed by infrared, Raman, nuclear magnetic resonance, and x-ray photoelectron spectroscopies.[92] Because of the industrial advantages of heterogeneous catalysis compared to homogeneous catalysis, preparation of solid superacids has become an important area of research.[82] Several classes of solid superacids exist including liquid acids mounted on a solid support,[93] sulfate-activated metal oxides,[94-96] mixed salts,[97,98] and zeolites.[99]

Acid catalysis represents a unique chemistry that relies on charge transfer via protons and molecular ions, and many similarities appear to exist between SMSI and acid–base catalysis. The evolution of this work that began by measuring chemically induced charge flow at the oxide–metal interface[100-102] is quickly leading to a molecular level study of acid catalyzed chemistry with a focus on understanding the close relationship between charge flow and catalytic selectivity. Specifically, it is clear that a fundamental understanding of catalyst selectivity is closely related to understanding the flow of charge between various active sites on a catalyst. This charge flow occurs both by the migration of molecular ions and by electrical conduction. Additionally, by controlling the flow of charge at a catalyst interface, novel reaction pathways will become accessible, and these processes are central to the future of chemical energy conversion.

1.5 Summary of Dissertation

1.5.1 Experimental Methods

Experimental methods used in this research are discussed in Chapter 2 with a focus on catalyst preparation, characterization, and reaction studies. Catalyst preparation includes fabrication of solid-state catalytic devices, synthesis of colloidal nanoparticles, and deposition and processing of oxide thin-films used for metal catalyst supports. A range of techniques were used for catalyst characterization. Ex situ methods include electron microscopy, x-ray photoelectron spectroscopy (XPS), and electrical probe measurements. In situ methods include bias and photocurrent measurements and sum frequency generation (SFG) vibrational spectroscopy. Reaction studies were performed in gas phase batch mode reactors with gas chromatography (GC) detectors.

1.5.2 Solid-State Device for External Control of Catalytic Chemistry

Chapters 3 and 4 describe the development of a novel solid-state charge-based device for external electronic control of catalytic chemistry. Chapter 3 describes results for the CO oxidation reaction and Chapter 4 describes results for the H_2 oxidation reaction. Together these findings show that a bias-induced negative charge at the Pt surface enhances the rate of catalytic oxidation while a flux of photo-induced positive charges to the Pt surface decreases the rate of oxidation chemistry. This is the first time that a charge-based device has been shown to provide external control of a surface catalytic reaction as determined by directly measuring the product yield, and the results for CO oxidation have been published in *Nano Letters*.[78] The results for H_2 oxidation are yet unpublished owing to experimental difficulties affecting the signal quality.

1.5.3 Fluorine-Doped Titanium Oxide as an Electronically Active Platinum Support

Similar electronic effects in catalytic oxidation are possible by chemical doping, and Chapters 5–7 discuss the effects of F in titanium oxide films used as supports for Pt catalysts. Chapter 5 describes a method for n-type doping titanium oxide using plasma F insertion. F has two effects on the doped oxide: First, F passivates O-vacancies. In titanium oxide O-vacancies give rise to partially occupied midgap defect states that act as the primary conduction channel; these states also pin the Fermi energy well below the conduction band edge. When these O-vacancies are passivated by F doping, electrical conductivity decreases, and the Fermi energy approaches the conduction band edge. Second, F acts as an n-type dopant by donating electrons to the conduction band of titanium oxide. By these combined effects, F doping allows fabrication of titanium oxide films with a high Fermi energy and an electron transport channel in the true conduction band, and these effects on the electronic structure of titanium oxide have been published in *Nano Letters*.[76]

Chapters 6 and 7 show that supporting Pt catalysts on F-doped titanium oxide results in electronically mediated catalytic activity for CO oxidation and methanol oxidation. In the case of CO oxidation, electron density from the highly n-type support appears to activate surface O, resulting in an approximately two-fold increase in catalytic activity. This result is exactly analogous to the electronic effect observed by external bias in a catalytic solid-state device. In the case of methanol oxidation, a change in reaction selectivity occurs as a result of substrate doping. Methanol oxidation on Pt produces both formaldehyde and CO_2. It appears that

different surface O species give rise to the different reaction products, and the electronically activated surface O on the highly n-type support favors partial oxidation of methanol to formaldehyde. These results on the utility of F-doped titanium oxide as an electronically active support for Pt catalysts have been published in *Journal of Physical Chemistry C*.[39,77] In addition, two patents are pending based on the reported work with F-doped titanium oxide.[103,104]

1.5.4 Strong Metal–Support Interactions Probed by Sum Frequency Generation Vibrational Spectroscopy

Chapter 8 describes a molecular level investigation of strong metal–support interactions in furfuraldehyde hydrogenation on supported Pt nanoparticles. In this study, no support effect is observed on the reaction kinetics of Pt nanoparticles capped with poly(vinylpyrrolidone) (PVP) because PVP inhibits contact between Pt and the support. However, when the PVP cap is removed by UV cleaning, a 50-fold enhancement is observed in the selective production of furfuryl alcohol by Pt nanoparticles supported on TiO_2, while no effect is observed for Pt nanoparticles supported on SiO_2. Using SFG vibrational spectroscopy, the highly selective reaction pathway on the Pt/TiO_2 catalyst is correlated with the formation of a furfuryl-oxy intermediate on the TiO_2 support. It appears that the role of the Pt/TiO_2 interface is to allow H spillover to active sites on the support, and H spillover is directly observed during reaction as a change in the nonresonant intensity in the SFG spectrum. Density functional calculations predict that O-vacancies in the TiO_2 are the catalytically active sites and that selective furfuryl alcohol formation is activated by an electron transfer from a Ti^{3+} cation to the adsorbed furfuraldehyde molecule. This work draws a strong analogy between SMSI and acid–base catalysis and has been submitted for publication to *Journal of American Chemical Society*. A continuation of this work is currently in progress to compare the reaction kinetics and SFG spectra for furfuraldehyde, crotonaldehyde, and acetaldehyde hydrogenation on supported Pt catalysts.

1.5.5 The Role of an Organic Cap in Nanoparticle Catalysis

The organic cap used to stabilize colloidal nanoparticles also has an important role in mediating the surface chemistry of nanoparticle catalysts. Chapters 9 and 10 investigate this effect using SFG vibrational spectroscopy to probe the structure of the organic capping layer on Pt nanoparticles under reaction conditions. Chapter 9 shows that when UV cleaning is used to remove PVP from Pt nanoparticles, carbonaceous fragments remain on the surface. These fragments dynamically restructure in H_2 and O_2 and control the activity of Pt nanoparticles for ethylene hydrogenation and methanol oxidation across several orders of magnitude. These carbonaceous fragments form a tightly closed shell in O_2 that prevents access to the Pt surface, but this shell opens in H_2. From kinetic measurements on thermally cleaned PVP- and oleic acid-capped Pt nanoparticles, it appears that formation of this dynamic carbonaceous layer occurs regardless of the capping agent or cleaning method. This study contradicts conventional assumptions that the capping agent necessarily inhibits nanoparticle activity and shows that for methanol oxidation, capped nanoparticles are orders of magnitude more active than their cleaned analogues. A manuscript describing this discovery will be submitted soon for publication.

Chapter 10 investigates the thermal stability of PVP-capped Pt nanoparticles before and after UV cleaning. It is found that while the capped nanoparticles are thermally stable in reaction conditions up to 473 K, the UV-cleaned particles melt below 373 K. This loss of thermal stability after cap removal precludes UV cleaning for studies of size- and shape-

controlled Pt nanoparticles. However, SFG studies of capped nanoparticles during reaction are challenging because vibrational modes of the organic cap often overlap with vibrational modes of the reaction intermediates of interest. Solvent cleaning is suggested as an alternative method for PVP removal from Pt nanoparticles. It is shown that while solvent cleaning does not remove the cap in its entirety, the remaining PVP disorders in H_2 allowing clear SFG identification of reaction intermediates for cyclohexene hydrogenation. It is further shown that solvent cleaning preserves the thermal stability of the Pt nanoparticles, making this method a viable alternative to UV cleaning for SFG studies of size- and shape-controlled nanoparticles. This work is published in *Journal of Physical Chemistry C*.

1.6 References

(1) Somorjai, G. A.; Li, Y. *Introduction to surface chemistry and catalysis*; 2nd Edition ed.; Johns Wiley & Sons, Inc.: Hoboken, NJ, 2010.

(2) Somorjai, G. A.; Carrazza, J. *Industrial & Engineering Chemistry Fundamentals* **1986**, *25*, 63.

(3) Boudart, M. In *Advances in Catalysis*; D.D. Eley, H. P., Paul, B. W., Eds.; Academic Press: 1969; Vol. Volume 20, p 153.

(4) Ferrer, S.; Rojo, J. M.; Salmerón, M.; Somorjai, G. A. *Philosophical Magazine A* **1982**, *45*, 261.

(5) Salmeron, M.; Gale, R. J.; Somorjai, G. A. *The Journal of Chemical Physics* **1977**, *67*, 5324.

(6) Salmerona, M.; Gale, R. J.; Somorjai, G. A. *The Journal of Chemical Physics* **1979**, *70*, 2807.

(7) Kliewer, C. J.; Bieri, M.; Somorjai, G. A. *Journal of the American Chemical Society* **2009**, *131*, 9958.

(8) Kliewer, C. J.; Aliaga, C.; Bieri, M.; Huang, W.; Tsung, C.-K.; Wood, J. B.; Komvopoulos, K.; Somorjai, G. A. *Journal of the American Chemical Society* **2010**, *132*, 13088.

(9) McCrea, K. R.; Parker, J. S.; Somorjai, G. A. *The Journal of Physical Chemistry B* **2002**, *106*, 10854.

(10) Strongin, D. R.; Carrazza, J.; Bare, S. R.; Somorjai, G. A. *Journal of Catalysis* **1987**, *103*, 213.

(11) Andersson, M. P.; Abild-Pedersen, E.; Remediakis, I. N.; Bligaard, T.; Jones, G.; Engbwk, J.; Lytken, O.; Horch, S.; Nielsen, J. H.; Sehested, J.; Rostrup-Nielsen, J. R.; Norskov, J. K.; Chorkendorff, I. *Journal of Catalysis* **2008**, *255*, 6.

(12) *Preparation of Solid Catalysts*; Ertl, G.; Knozinger, H.; Weitkamp, J., Eds.; Wiley-VCH: Weinheim, Germany, 1999.

(13) Tsoncheva, T.; Dal Santo, V.; Gallo, A.; Scotti, N.; Dimitrov, M.; Kovacheva, D. *Appl Catal a-Gen* **2011**, *406*, 13.

(14) Ahmadi, T. S.; Wang, Z. L.; Green, T. C.; Henglein, A.; El-Sayed, M. A. *Science* **1996**, *272*, 1924.

(15) Peng, X.; Wickham, J.; Alivisatos, A. P. *Journal of the American Chemical Society* **1998**, *120*, 5343.

(16) Puntes, V. F.; Krishnan, K. M.; Alivisatos, A. P. *Science* **2001**, *291*, 2115.

(17) Oh, M.; Mirkin, C. A. *Nature* **2005**, *438*, 651.

(18) Yin, Y.; Alivisatos, A. P. *Nature* **2005**, *437*, 664.

(19) Song, H.; Kim, F.; Connor, S.; Somorjai, G. A.; Yang, P. *The Journal of Physical Chemistry B* **2004**, *109*, 188.
(20) Rioux, R. M.; Song, H.; Hoefelmeyer, J. D.; Yang, P.; Somorjai, G. A. *The Journal of Physical Chemistry B* **2004**, *109*, 2192.
(21) Song, H.; Rioux, R. M.; Hoefelmeyer, J. D.; Komor, R.; Niesz, K.; Grass, M.; Yang, P.; Somorjai, G. A. *Journal of the American Chemical Society* **2006**, *128*, 3027.
(22) Bratlie, K. M.; Lee, H.; Komvopoulos, K.; Yang, P.; Somorjai, G. A. *Nano Letters* **2007**, *7*, 3097.
(23) Kuhn, J. N.; Huang, W.; Tsung, C.-K.; Zhang, Y.; Somorjai, G. A. *Journal of the American Chemical Society* **2008**, *130*, 14026.
(24) Grass, M.; Rioux, R.; Somorjai, G. *Catalysis Letters* **2009**, *128*, 1.
(25) Grass, M. E.; Joo, S. H.; Zhang, Y.; Somorjai, G. A. *The Journal of Physical Chemistry C* **2009**, *113*, 8616.
(26) Witham, C. A.; Huang, W.; Tsung, C.-K.; Kuhn, J. N.; Somorjai, G. A.; Toste, F. D. *Nat Chem* **2010**, *2*, 36.
(27) Alayoglu, S.; Aliaga, C.; Sprung, C.; Somorjai, G. *Catalysis Letters* **2011**, *141*, 914.
(28) Zhang, Y.; Grass, M. E.; Kuhn, J. N.; Tao, F.; Habas, S. E.; Huang, W.; Yang, P.; Somorjai, G. A. *Journal of the American Chemical Society* **2008**, *130*, 5868.
(29) Kuhn, J. N.; Tsung, C.-K.; Huang, W.; Somorjai, G. A. *Journal of Catalysis* **2009**, *265*, 209.
(30) Gorin, D. J.; Sherry, B. D.; Toste, F. D. *Chemical Reviews* **2008**, *108*, 3351.
(31) Schwab, G. M. *Transactions of the Faraday Society* **1946**, *42*, 689.
(32) Tauster, S. J.; Fung, S. C.; Garten, R. L. *Journal of the American Chemical Society* **1978**, *100*, 170.
(33) Tauster, S. J.; Fung, S. C.; Baker, R. T. K.; Horsley, J. A. *Science* **1981**, *211*, 1121.
(34) Tauster, S. J. *Accounts of Chemical Research* **1987**, *20*, 389.
(35) Oh, S. H.; Eickel, C. C. *Journal of Catalysis* **1988**, *112*, 543.
(36) Zhu, H.; Qin, Z.; Shan, W.; Shen, W.; Wang, J. *Journal of Catalysis* **2004**, *225*, 267.
(37) Chen, M. S.; Goodman, D. W. *Science* **2004**, *306*, 252.
(38) Goodman, D. *Catalysis Letters* **2005**, *99*, 1.
(39) Baker, L. R.; Hervier, A.; Seo, H.; Kennedy, G.; Komvopoulos, K.; Somorjai, G. A. *The Journal of Physical Chemistry C* **2011**, *115*, 16006.
(40) Boffa, A. B.; Bell, A. T.; Somorjai, G. A. *Journal of Catalysis* **1993**, *139*, 602.
(41) Boffa, A.; Lin, C.; Bell, A. T.; Somorjai, G. A. *Journal of Catalysis* **1994**, *149*, 149.
(42) Yamada, Y.; Tsung, C.-K.; Huang, W.; Huo, Z.; Habas, S. E.; Soejima, T.; Aliaga, C. E.; Somorjai, G. A.; Yang, P. *Nat Chem* **2011**, *3*, 372.
(43) Vannice, M. A.; Sen, B. *Journal of Catalysis* **1989**, *115*, 65.
(44) Lin, S. D.; Sanders, D. K.; Albert Vannice, M. *Applied Catalysis A: General* **1994**, *113*, 59.
(45) Kijeński, J.; Winiarek, P. *Applied Catalysis A: General* **2000**, *193*, L1.
(46) Malathi, R.; Viswanath, R. P. *Applied Catalysis A: General* **2001**, *208*, 323.
(47) Kijeński, J.; Winiarek, P.; Paryjczak, T.; Lewicki, A.; Mikołajska, A. *Applied Catalysis A: General* **2002**, *233*, 171.
(48) Enache, D. I.; Edwards, J. K.; Landon, P.; Solsona-Espriu, B.; Carley, A. F.; Herzing, A. A.; Watanabe, M.; Kiely, C. J.; Knight, D. W.; Hutchings, G. J. *Science* **2006**, *311*, 362.

(49) Landon, P.; Collier, P. J.; Papworth, A. J.; Kiely, C. J.; Hutchings, G. J. *Chemical Communications* **2002**, 2058.
(50) Landon, P.; Collier, P. J.; Carley, A. F.; Chadwick, D.; Papworth, A. J.; Burrows, A.; Kiely, C. J.; Hutchings, G. J. *Physical Chemistry Chemical Physics* **2003**, *5*, 1917.
(51) Fu, Q.; Saltsburg, H.; Flytzani-Stephanopoulos, M. *Science* **2003**, *301*, 935.
(52) Edwards, J. K.; Solsona, B. E.; Landon, P.; Carley, A. F.; Herzing, A.; Kiely, C. J.; Hutchings, G. J. *Journal of Catalysis* **2005**, *236*, 69.
(53) Fan, S.; Yi, J.; Wang, L.; Mi, Z. *Reaction Kinetics and Catalysis Letters* **2007**, *92*, 175.
(54) Vernon, P. D. F.; Green, M. L. H.; Cheetham, A. K.; Ashcroft, A. T. *Catalysis Letters* **1990**, *6*, 181.
(55) Ashcroft, A. T.; Cheetham, A. K.; Green, M. L. H.; Vernon, P. D. F. *Nature* **1991**, *352*, 225.
(56) Nakagawa, K.; Ikenaga, N.; Suzuki, T.; Kobayashi, T.; Haruta, M. *Applied Catalysis A: General* **1998**, *169*, 281.
(57) Haruta, M. *Cattech* **2002**, *6*, 102.
(58) Pietron, J. J.; Stroud, R. M.; Rolison, D. R. *Nano Letters* **2002**, *2*, 545.
(59) Molina, L. M.; Rasmussen, M. D.; Hammer, B. *Journal of Chemical Physics* **2004**, *120*, 7673.
(60) Akubuiro, E. C.; Verykios, X. E. *Journal of Catalysis* **1988**, *113*, 106.
(61) Baker, R. T. K.; Prestridge, E. B.; McVicker, G. B. *Journal of Catalysis* **1984**, *89*, 422.
(62) Komaya, T.; Bell, A. T.; Wengsieh, Z.; Gronsky, R.; Engelke, F.; King, T. S.; Pruski, M. *Journal of Catalysis* **1994**, *149*, 142.
(63) Bernal, S.; Calvino, J. J.; Cauqui, M. A.; Gatica, J. M.; López Cartes, C.; Pérez Omil, J. A.; Pintado, J. M. *Catalysis Today* **2003**, *77*, 385.
(64) Berlowitz, P. J.; Peden, C. H. F.; Goodman, D. W. *The Journal of Physical Chemistry* **1988**, *92*, 5213.
(65) Su, X.; Cremer, P. S.; Shen, Y. R.; Somorjai, G. A. *Journal of the American Chemical Society* **1997**, *119*, 3994.
(66) Liu, L.; Zhou, F.; Wang, L.; Qi, X.; Shi, F.; Deng, Y. *Journal of Catalysis* **2010**, *274*, 1.
(67) Vayssilov, G. N.; Lykhach, Y.; Migani, A.; Staudt, T.; Petrova, G. P.; Tsud, N.; Skála, T.; Bruix, A.; Illas, F.; Prince, K. C.; Matolı´n, V. r.; Neyman, K. M.; Libuda, J. *Nat Mater* **2011**, *10*, 310.
(68) Takakusagi, S.; Fukui, K.-i.; Tero, R.; Asakura, K.; Iwasawa, Y. *Langmuir* **2010**, *26*, 16392.
(69) Conner, W. C.; Falconer, J. L. *Chemical Reviews* **1995**, *95*, 759.
(70) Bonn, M.; Funk, S.; Hess, C.; Denzler, D. N.; Stampfl, C.; Scheffler, M.; Wolf, M.; Ertl, G. *Science* **1999**, *285*, 1042.
(71) Lambert, R. M.; Cropley, R. L.; Husain, A.; Tikhov, M. S. *Chemical Communications* **2003**, 1184.
(72) Zhang, Y.; Kolmakov, A.; Chretien, S.; Metiu, H.; Moskovits, M. *Nano Letters* **2004**, *4*, 403.
(73) Zhang, J.; Liu, X.; Blume, R.; Zhang, A. H.; Schlogl, R.; Su, D. S. *Science* **2008**, *322*, 73.
(74) Kaden, W. E.; Wu, T. P.; Kunkel, W. A.; Anderson, S. L. *Science* **2009**, *326*, 826.
(75) Zhang, Z.; Yates, J. T. *Journal of the American Chemical Society* **2010**, *132*, 12804.
(76) Seo, H.; Baker, L. R.; Hervier, A.; Kim, J.; Whitten, J. L.; Somorjai, G. A. *Nano Letters* **2010**, *11*, 751.

(77) Hervier, A.; Baker, L. R.; Komvopoulos, K.; Somorjai, G. A. *The Journal of Physical Chemistry C* **2011**.
(78) Baker, L. R.; Hervier, A.; Kennedy, G.; Somorjai, G. A. *Nano Letters* **2012**, *12*, 2554.
(79) Jencks, W. P. *Accounts of Chemical Research* **1980**, *13*, 161.
(80) Greeley, J.; Norskov, J. K.; Mavrikakis, M. *Annu. Rev. Phys. Chem.* **2002**, *53*, 319.
(81) Olah, G. A.; Molnar, A. *Hydrocarbon Chemistry*; 2nd Edition ed.; John Wiley & Sons, Inc.: Hoboken, NJ, 2003.
(82) Yamaguchi, T. *Applied Catalysis* **1990**, *61*, 1.
(83) Takahashi, O.; Hattori, H. *Journal of Catalysis* **1981**, *68*, 144.
(84) Schmerling, L.; Vesely, J. A. *The Journal of Organic Chemistry* **1973**, *38*, 312.
(85) Guo, C.; Yao, S.; Cao, J.; Qian, Z. *Applied Catalysis A: General* **1994**, *107*, 229.
(86) Kovacic, P.; Kyriakis, A. *Journal of the American Chemical Society* **1963**, *85*, 454.
(87) Li, W.; Shen, Z.; Zhang, Y. *European Polymer Journal* **2001**, *37*, 1185.
(88) Volkova, G. G.; Plyasova, L. M.; Shkuratova, L. N.; Budneva, A. A.; Paukshtis, E. A.; Timofeeva, M. N.; Likholobov, V. A. In *Studies in Surface Science and Catalysis*; Xinhe, B., Yide, X., Eds.; Elsevier: 2004; Vol. Volume 147, p 403.
(89) Gillespie, R. J. *Accounts of Chemical Research* **1968**, *1*, 202.
(90) Gillespie, R. J.; Peel, T. E.; Robinson, E. A. *Journal of the American Chemical Society* **1971**, *93*, 5083.
(91) Gillespie, R. J.; Peel, T. E. *Journal of the American Chemical Society* **1973**, *95*, 5173.
(92) Olah, G. A. *Angewandte Chemie International Edition in English* **1973**, *12*, 173.
(93) Heinerman, J. J. L.; Gaaf, J. *Journal of Molecular Catalysis* **1981**, *11*, 215.
(94) Kayo, A.; Yamaguchi, T.; Tanabe, K. *Journal of Catalysis* **1983**, *83*, 99.
(95) Yamaguchi, T.; Jin, T.; Tanabe, K. *The Journal of Physical Chemistry* **1986**, *90*, 3148.
(96) Jin, T.; Yamaguchi, T.; Tanabe, K. *The Journal of Physical Chemistry* **1986**, *90*, 4794.
(97) Ono, Y.; Tanabe, T.; Kitajima, N. *Journal of Catalysis* **1979**, *56*, 47.
(98) Ono, Y.; Yamaguchi, K.; Kitajima, N. *Journal of Catalysis* **1980**, *64*, 13.
(99) Maxwell, I. E. *Catalysis Today* **1987**, *1*, 385.
(100) Park, J. Y.; Somorjai, G. A. *Chemphyschem* **2006**, *7*, 1409.
(101) Hervier, A.; Renzas, J. R.; Park, J. Y.; Somorjai, G. A. *Nano Letters* **2009**, *9*, 3930.
(102) Maximoff, S. N.; Head-Gordon, M. P. *Proceedings of the National Academy of Sciences* **2009**, *106*, 11460.
(103) Baker, L. R.; Seo, H.; Hervier, A.; Somorjai, G. 2011.
(104) Baker, L. R.; Seo, H.; Hervier, A.; Somorjai, G. 2011.

Chapter 2

Experimental Methods

2.1 Catalyst Fabrication and Synthesis

2.1.1 Thin Film Deposition and Processing

2.1.1.1 Electron Beam Evaporation—In this work thin film deposition was an important step in the fabrication of catalytic solid-state charge-based devices; oxide thin films also served as Pt supports for studying metal–support interactions. Two methods were used for thin film deposition: electron beam evaporation and magnetron sputtering. Electron beam evaporation uses an electron beam to melt and vaporize a target material. This vapor then expands into a vacuum and condenses on a desired substrate. Because the expansion of the target vapor into vacuum is directional, shadow masks can control the pattern of the thin film deposited on the substrate. This method is capable of depositing both metallic and insulating target materials. The target material is placed inside a crucible liner that rests in a water-cooled hearth. A high voltage (5 keV) is then applied between a W filament and the hearth. Subsequent ohmic heating of the filament results in electron emission, and the electrons are accelerated across the applied bias toward the hearth. The hearth is covered with a set of permanent magnets that direct the electron beam from the filament to the target. The high energy electron beam heats the target which first melts and then vaporizes into the vacuum. The pressure is maintained at 10^{-5} Torr or less to allow the vapor to ascend directionally to the top of the chamber. The substrate is suspended at the top of the chamber, and as the target vapor ascends, it deposits as a thin film on the substrate.

2.1.1.2 Magnetron Sputtering—Magnetron sputtering uses the collision of ions on a target material to eject atoms from the target to the gas phase, and these atoms subsequently deposit on a substrate. This technique requires a backpressure of gas (usually Ar) in the tens of mTorr range to generate ions for bombarding the target. The magnetron consists of a cathode and anode, and a high voltage serves to ionize the Ar gas and accelerate the positive ions toward the target. A magnetic field is typically present to control the trajectory of gas phase ions to further enhance ionization by secondary collisions. The collision of Ar ions on the target ejects neutral target atoms into the gas phase, and these atoms deposit on a substrate that is suspended in the chamber above the magnetron. Magnetron sputtering can deposit both metallic and insulating thin films. For metal deposition, a DC magnetron is typically used. For insulator deposition, an AC magnetron operating at an RF frequency prevents charging of the insulating target. To control the oxidation state of a deposited film, it is possible to leak in a backpressure of O_2 during sputtering.

2.1.1.3 Quartz Crystal Microbalance—In both electron beam evaporation and magnetron sputtering, the film thickness can be monitored during growth using a quartz crystal microbalance. A quartz crystal microbalance uses quartz as a piezoelectric material. An oscillating voltage applied to the crystal causes it to oscillate; a resonant oscillation frequency exists that is a function of adsorbed mass on the crystal surface according to the Sauerbrey

equation. By measuring the resonant frequency of oscillation, it is possible to extract the mass on the surface of the crystal monitor. This mass is then converted to an average film thickness on the substrate using the density and a geometric scaling factor (Z factor). The Z factor depends on the relative positions of the crystal monitor and the substrate inside the deposition chamber.

2.1.1.4 Rapid Thermal Annealing—The crystallinity of the oxide thin films can be enhanced after deposition by rapid thermal annealing (RTA). RTA uses high intensity lamps to achieve fast substrate heating; temperatures in excess of 1,000 K are possible with ramp times less than 1 min. The flow of gasses over the sample during annealing also provides a degree of control over the oxidation state. Starting from an O deficient oxide film, the O stoichiometry can be increased by annealing in O_2. Alternately, RTA in an inert gas can increase the film crystallinity without changing the oxidation state.

2.1.1.5 Plasma Fluorine Doping—F doping to titanium oxide thin films was achieved in a parallel plate reactive ion etch (RIE) chamber. Gasses are introduced in the chamber by mass flow controllers and the chamber is differentially pumped to maintain a pressure in the tens of mTorr range. An electromagnetic field oscillating at RF frequencies generates an inductively coupled plasma inside the chamber; this plasma serves as a supply of reactive ions. F ions are generated at low concentration in the plasma by introducing a trace amount of SF_6 in a background of N_2. A DC bias between the top and bottom plates directs the negative ions from the plasma downward toward the sample. This bias is in the range of 150 V and serves to drive negatively charged F ions into the titanium oxide thin film.

2.1.2 Preparation of 2-Dimensional Model Catalysts from Colloidal Nanoparticles

2.1.2.1 Colloidal Synthesis of Nanoparticles—Two methods are used for the colloidal synthesis of Pt nanoparticles. Both methods rely on the reduction of chloroplatinic acid in ethylene glycol. In one case chloroplatinic acid hexahydrate and PVP are combined in ethylene glycol in a 1:4 mass ratio and heated to 438 K under a flow of Ar for 1 h. This results in 4.5 nm PVP-capped Pt nanoparticles. These nanoparticles are washed by precipitation in hexanes followed by redispersion in ethanol, and the number of washes determines the amount of PVP left on the nanoparticles. The other method does not use a capping agent during synthesis. Instead chloroplatinic acid is reduced in a solution of NaOH in ethylene glycol. Chloroplatinic acid hexahydrate and NaOH are combined in ethylene glycol in a 1:1 mass ratio and heated to 433 K for 3 h. This results in 1.7 nm uncapped Pt nanoparticles. These nanoparticles are precipitated by neutralizing the solution with 2 M HCl. The nanoparticles are then re-dispersed in ethanol containing a desired capping agent. This synthesis allows for the preparation of identical Pt nanoparticles where the only variable between samples is the capping agent.

2.1.2.2 Langmuir Blodgett Deposition—Formation of 2-dimensional films of monodisperse nanoparticles to serve as model catalysts was achieved by Langmuir Blodgett (LB) deposition. The nanoparticles are suspended in a hydrophobic solvent such as chloroform and dispersed onto a water surface. Time is given for the solvent to evaporate, leaving a 2-dimensional dispersion of nanoparticles. The nanoparticle film is then compressed with a mobile barrier, and the surface pressure is monitored as a function of decreasing surface area. The surface pressure corresponds to the density of nanoparticles on the water. When the desired surface pressure is reached, a substrate is pulled out from under the surface of the water, and the

film of nanoparticles is deposited onto the substrate. The final density of nanoparticles on the substrate can be controlled by controlling the surface pressure during deposition.

2.1.2.3 Organic Cap Removal by UV Cleaning—UV cleaning was used to remove the organic cap from the Pt nanoparticles. This increases the Pt surface area available for reaction. This also brings the Pt into close contact with the support for studying metal–support interactions. Two low-pressure mercury (Hg) lamps (Lights Sources Inc., model number GPH357T5VH/4P) are used as the UV source; the Hg lamps emit two lines at 184 and 254 nm. The two lamps are aligned parallel to each other 2.5 cm apart in a clean Al box. The sample sits 1.2 cm below the lamps. By varying the time of UV exposure, it is possible to control the amount of organic cap removed from the Pt nanoparticles. This cleaning is believed to be the combined effect of direct photodecomposition of the organic cap and oxidation of the cap by ozone produced from the 184 nm Hg line.

2.2 Catalyst Characterization

2.2.1 Electrical Probe Measurements

Electrical probe measurements were used to characterize the performance of solid-state devices and as well as the surface conductivity of titanium oxide thin films. All electrical probe measurements were performed using Keithley 2400 Sourcemeter. To evaluate the performance of Schottky diode and heterojunction devices, current–voltage (IV) curves were measured by scanning a probe voltage and measuring the current passed through the sample. From an IV curve it is possible to determine many of the device properties including the rectification factor, built-in potential, and photovoltaic efficiency. Rectification factor is taken as the ratio of current passed at equal forward and reverse bias voltages. This value characterizes the efficiency of a diode which is designed to pass current only in one direction. The built-in potential of a device describes the difference in Fermi energy between the two active layers in a diode structure. It is given as the voltage showing current onset in the forward bias direction of an IV curve. The determination of rectification factor and built-in potential from an IV curve is depicted in Fig. 1A.

Photovoltaic efficiency is determined by the IV curve of a photodiode during illumination. The power output of the device is given as the area above the IV curve during illumination integrated along the voltage axis from zero bias (i.e., closed circuit current) to the intercept on the current axis (i.e., open circuit voltage) as shown in Fig. 1B. Normalizing this value to the known power of the incident light gives the power conversion efficiency of the photovoltaic device. Alternately, the quantum efficiency can be calculated by normalizing the current flow during illumination to the number of incident photons. Quantum efficiency is usually reported for closed circuit, zero bias conditions, but an applied bias can tune the quantum efficiency of a device.

Conductivity of oxide thin films was also determined by IV measurements. In this case, the slope of an IV curve represents the sample conductance. Conductivity is simply given by normalizing the conductance to the dimensions of the conduction channel as shown in Eq. 1.

$$\sigma = \frac{G \cdot L}{A} \qquad \text{Eq. 1}$$

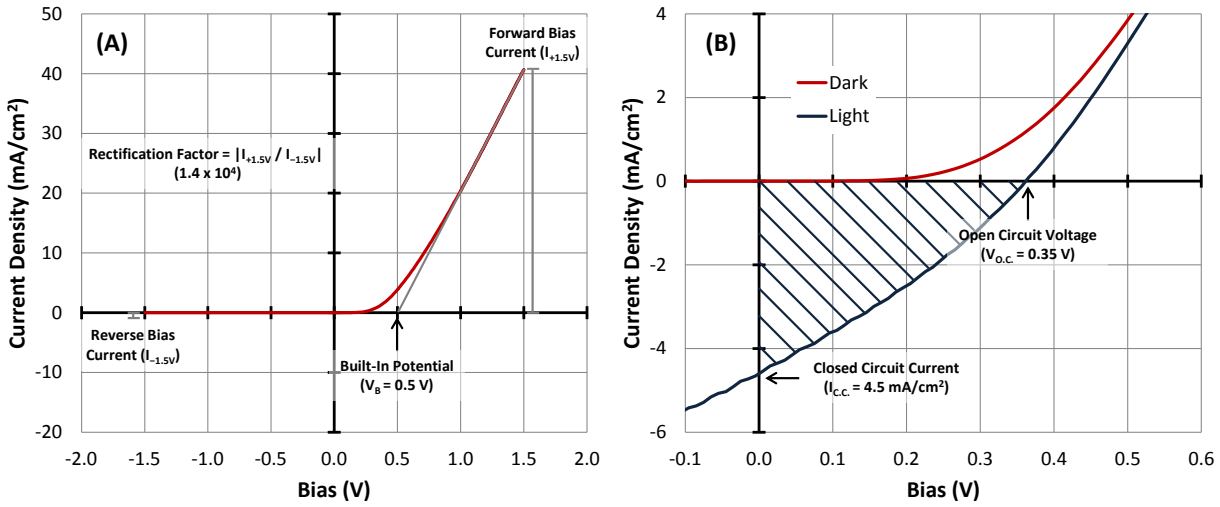

Fig. 1 (A) *IV curve of Pt/n-Si catalytic diode. From the IV curve the built-in potential and rectification factor of the device are easily determined.* **(B)** *IV curves of Pt/n-Si catalytic diode in dark and during illumination. The power output of the device is determined by integrating the shaded area of the curve between the closed circuit current and the open circuit voltage.*

where σ is the material conductivity, G is the sample conductance, L is the length of the conduction channel, and A is the area of the conduction channel.

2.2.2 X-Ray Photoelectron Spectroscopy

X-ray photoelectron spectroscopy (XPS) provides elemental analysis of surfaces. XPS can also resolve oxidation states of the various elements. The technique works using a monochromatic x-ray source (usually from an Al or Mg anode) to excite core electrons from a sample into the vacuum. The kinetic energy of these photoelectrons is measured using an electron energy analyzer. The difference between the x-ray energy and the kinetic energy of the photoelectron is equal to the binding energy of the electron in the sample. Because core electrons in each element have a characteristic binding energy, this method provides elemental surface analysis. Shifts in this binding energy are characteristic of the oxidation state of the element. The surface sensitivity of XPS is determined by the mean free path of photoelectrons escaping from the sample. Depending on the material and the kinetic energy of the photoelectron, the mean free path is on the order of 1–2 nm, so XPS typically probes ~10 atomic layers deep.

The monochromatic x-ray source is usually generated from an Al or Mg anode. A high voltage (30–50 keV) between a W filament and the anode leads to electron emission from the filament and collision on the anode. This collision of high energy electrons results in excitation of core electrons. Subsequent electron relaxation leads to emission of well-defined x-ray lines depending on the anode material. A filter or grating then selects a single emission line (usually K-alpha) for use as the x-ray source.

A hemispherical analyzer is used to analyze the kinetic energy of photoelectrons ejected from the sample. A hemispherical analyzer uses a magnetic field to bend the photoelectrons in

an arc. The radial trajectory of an electron in the analyzer depends on the strength of the magnetic field and the kinetic energy of the electron. If a slit is placed in front of an electron detector located inside the analyzer, only electrons of a specified kinetic energy will pass through the slit and impinge on the detector for a given magnetic field strength. When the magnetic field is scanned, electrons across a range of energies are detected resulting in a photoemission spectrum.

XPS usually requires ultra-high vacuum to allow transmission of photoelectrons from the sample to the energy analyzer. However, a differential pumping system allows for collection of photoelectron spectra at pressures up to hundreds of mTorr. The differential pumping system consists of three differentially pumped chambers. A nose cone that opens to the high pressure sample cell is placed less than 1 mm from the sample surface. A series of magnetic lenses focus the photoelectron beam through the apertures of each differential pumping stage and into the electron energy analyzer. An outline of this detection system is shown in Scheme 1. This technique known as ambient pressure XPS allows for in situ characterization of a catalyst at moderate reaction pressures, and these experiments are performed using synchrotron radiation from the Advanced Light Source at Lawrence Berkeley National Lab. Ex situ XPS used in this study was performed at ultra-high vacuum on a commercial system (Physical Electronics, PHI 5400 ESCA/XPS) with an Al anode source at 1486.6 eV.

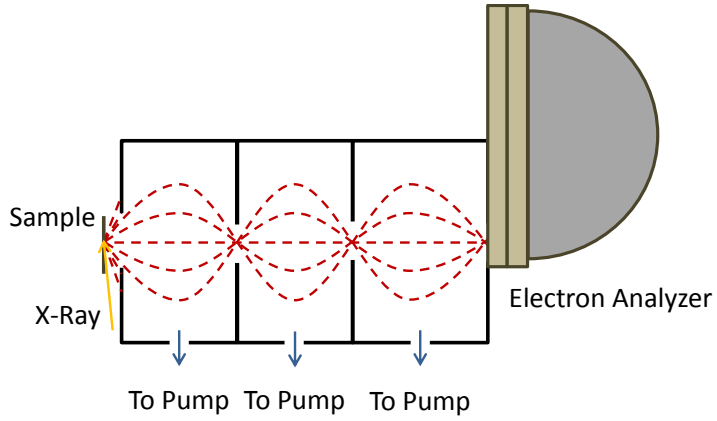

Scheme 1

2.2.3 Electron Microscopy

Catalyst morphology was examined before and after catalytic reactions using transmission electron microscopy (TEM) and scanning electron microscopy (SEM). TEM imaging was performed on a JOEL 2100 microscope operating at 200 kV. SEM imaging was performed on a Zeiss Gemini Ultra-55 microscope operating at 5 kV.

2.2.4 Sum Frequency Generation Vibrational Spectroscopy

Sum frequency generation (SFG) vibrational spectroscopy is a nonlinear optical spectroscopy that, by selection rules, is inherently surface or interface specific. In this work, SFG was used to observe the vibrational spectrum of reactant molecules on a catalyst surface during reaction; it is also used to probe the vibrational spectrum of organic capping agents on

catalytic nanoparticles in various reaction conditions. In SFG, an IR beam and a visible beam overlap in time and space on the sample surface and a third beam is generated in reflection with a frequency equal to the sum of the two input frequencies (see Scheme 2).

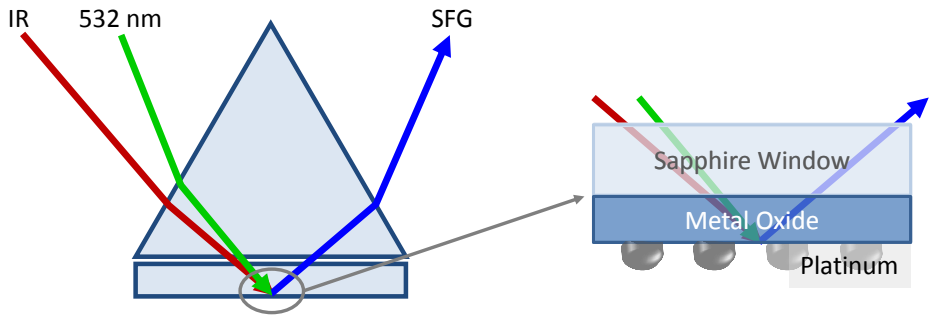

Scheme 2

The SFG signal intensity is proportional to the factor of the two input intensities as shown in Eq. 2.

$$I_{SFG} \propto X^{(2)} \cdot I_{IR} \cdot I_{VIS} \qquad \text{Eq. 2}$$

$X^{(2)}$ is a tensor representing the second order polarizability of the sample, I_{IR} is the IR beam intensity and I_{VIS} is the visible beam intensity. $X^{(2)}$ represents a spatial average of molecular hyperpolarizabilities, B, weighted by the number of molecules, N, on the surface as shown in Eq. 3.

$$X^{(2)} = N\langle B \rangle \qquad \text{Eq. 3}$$

An energy diagram for an SFG process is shown in Scheme 3. This shows SFG as the coherent combination of an IR absorption event and a Stokes Raman scattering event. Accordingly, the hyperpolarizability, B, of a molecule is given as the dot product of the dipole transition moment, μ (i.e., IR cross section), and the first order polarizability, α (i.e., Raman cross section), as shown in Eq. 4.

$$\beta_{abc} = \alpha_{ab} \cdot \mu_c \qquad \text{Eq. 4}$$

Molecular Cartesian coordinates are denoted as subscripts a, b, and c. SFG signal is enhanced when μ diverges at a vibrational resonance, so fixing the frequency of the visible beam and scanning the IR beam frequency across a range of interest produces the vibrational spectrum of a sample.

The surface sensitivity of SFG is given by the following relationships involving $X^{(2)}$. The first relationship given in Eq. 5 is an intrinsic property of $X^{(2)}$.

$$\chi^{(2)}_{-I-J-K} = -\chi^{(2)}_{IJK} \qquad \text{Eq. 5}$$

Here I, J, and K represent lab coordinates, and this relationship can be derived from a coordinate transformation of Eq. 3 and Eq. 4. In fact this relationship is true of all even order terms in the

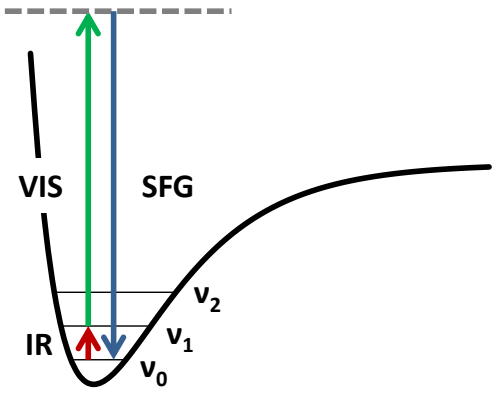

Scheme 3

polarizability expansion. The second relationship of $X^{(2)}$ is given in Eq. 6 and is true only of centrosymmetric media.

$$\chi^{(2)}_{-I-J-K} = \chi^{(2)}_{IJK} \qquad \text{Eq. 6}$$

Substituting Eq. 5 into Eq. 6 shows that in centrosymmetric media

$$\chi^{(2)}_{IJK} = -\chi^{(2)}_{IJK} = 0 \qquad \text{Eq. 7}$$

Because $X^{(2)}$ is zero for centrosymmetric media, SFG is only sensitive to a break in inversion symmetry which usually occurs at a surface or interface, and this relationship defines the surface sensitivity of SFG.

Nonlinear spectroscopy means that the signal intensity does not depend linearly on the intensity of a single probe beam such as in Raman or IR spectroscopy. In IR or Raman spectroscopy, if the intensity of the input beam doubles, then the signal intensity also doubles (i.e., the Raman scattering intensity in the case of Raman, or the absorption intensity in the case of IR). In SFG if the beam input intensity doubles (i.e., I_{IR} and I_{VIS} each double) then the signal intensity increases by a factor of 4 as shown in Eq. 2. That is why SFG is referred to as a nonlinear spectroscopy. This dictates certain experimental requirements for SFG, specifically high intensity pump lasers with ps or fs pulse widths. If the pulse width of the pump beams is increased to the ns time-scale, the signal intensity decreases by the square of the intensity drop. This loss in signal intensity is only compensated by a linear increase in the integration time, so the signal loss would be approximately 2–3 orders of magnitude. This relationship coupled with the relatively low cross-section for an SFG process (~10^{-6}) precludes any source other than ps or fs lasers for this experiment.

For SFG experiments, an active/passive mode-locked Nd:YAG laser (Leopard D-20, Continuum) produces a 20 ps pulse at a 20 Hz repetition rate. The fundamental output at 1064 nm is passed through an optical parametric generator/amplifier to generate a tunable infrared (IR) beam (2700–3600 cm^{-1}) and a second harmonic visible (VIS) beam (532 nm). The IR (100 μJ) and VIS (100 μJ) beams are spatially and temporally overlapped on the back surface of

a sapphire window containing the Pt nanoparticles supported on SiO_2 or TiO_2 thin films. The VIS and IR beam are incident on the sample at 40° and 50° degrees, respectively, relative to surface normal. The generated SFG signal is then collected and sent to a photomultiplier tube. A gated integrator enhances the signal-to-noise. To collect a spectrum, the IR beam is scanned across the spectral range of interest.

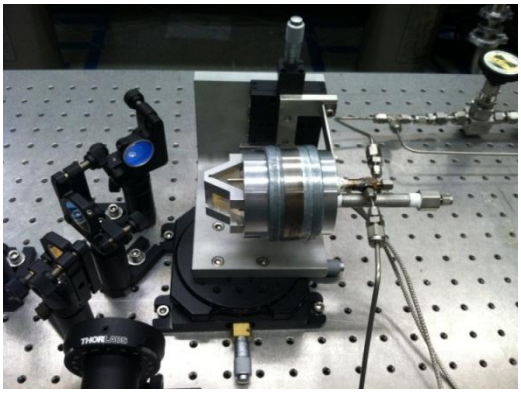

Fig. 2 *Reactor cell for in situ SFG measurements. The catalyst temperature can be controlled up to 523 K, and the cell can hold pressures up to 20 bar.*

The beams are directed onto the sample using a sapphire prism as shown above in Scheme 2. A solution of deuterated polystyrene (d8) in deuterated decalin (d18) serves as an index matching liquid that does not interfere with transmission of the IR beam at the C–H stretch frequency. The catalyst surface iss pressed into thermal contact with an aluminum heating block to heat the catalyst to reaction temperature. A recess in the heating block allows for the flow of reaction gasses across the catalyst surface. A metal bellows circulation pump provides gas mixing. A gas tight seal is made between the sapphire window and the heating block using a Kalrez O-ring. A picture of this system is shown in Fig. 2.

2.3 Catalytic Reaction Studies

Three identical stainless steel batch mode reactors were used for gas phase reaction studies. Batch mode reactors allow products to accumulate over time during reaction and were necessary to measure reaction kinetics on 2-dimensional catalysts because of their relatively low surface area. Compared to high surface area 3-dimensional catalysts, 2-dimensional samples were preferable for these studies because their planar geometry makes them compatible with the characterization techniques described above. Batch reactor volumes were each 1 L. Prior to each reaction, the chamber was evacuated to 10^{-5} Torr with a turbomolecular pump. The catalysts were heated during reaction using a resistive boron nitride substrate heater with a graphite filament (Momentive Performance Materials), and gas mixing was achieved using a metal bellows circulation pump (Senior Flexonics). Catalysts were typically tested over the course of several hours and reaction products were monitored as a function of time using gas chromatography (GC) with thermal conductivity and flame ionization detectors. Conversion was kept below approximately 10% to avoid the observation of secondary reaction pathways. An internal gas sampling loop in the GC was placed in line of the recirculation pump to allow automatic gas sampling at specified intervals during reaction. A diagram of the reactor system is shown in Scheme 4, and a picture is shown in Fig. 3.

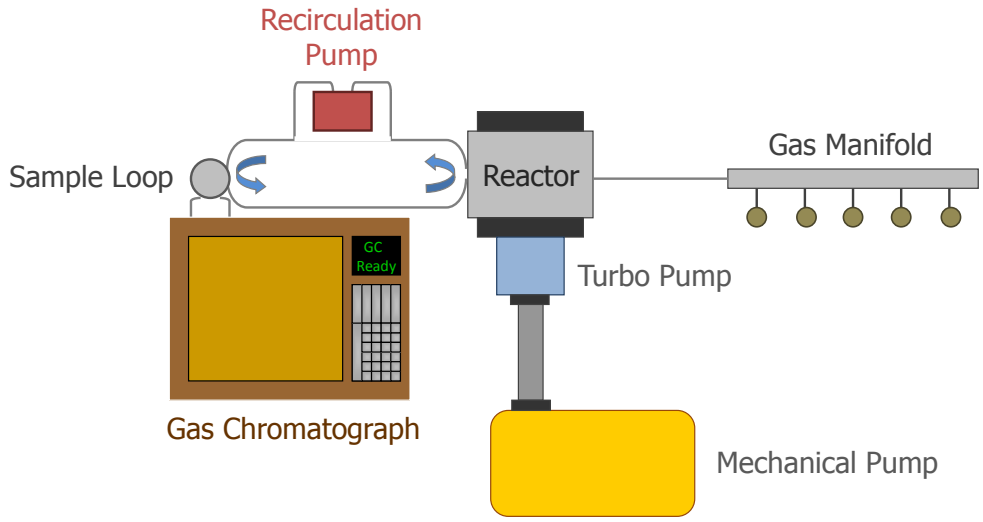

Scheme 4

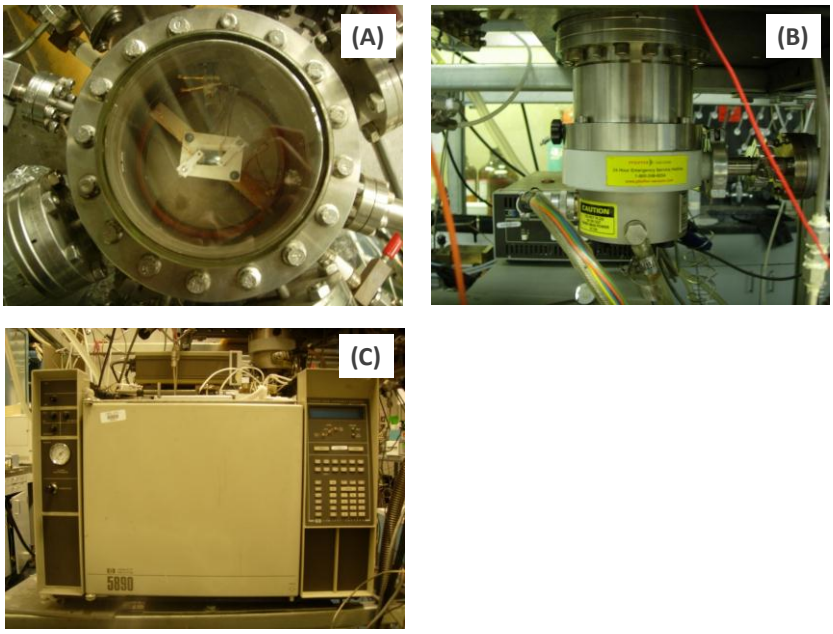

Fig. 3 (A) *Arial view of batch reactor with Pt/Si catalyst on the boron nitride substrate heater.* **(B)** *Turbomolecular pump used evacuate the reactor to 10−5 Torr prior to reaction.* **(C)** *Gas chromatograph used to detect reaction products.*

Chapter 3

Solid-State Charge-Based Device for Control of Catalytic Carbon Monoxide Oxidation on Platinum Nanofilms Using External Bias and Light

3.1 Abstract

Using a Pt/Si catalytic nanodiode, we externally control the rate of CO oxidation on a Pt nanofilm. The catalytic reaction can be turned on and off by alternating between bias states of the device. Additionally, the reaction rate is sensitive to photocurrent induced by visible light. The effects of both bias and light show that negative charge on the Pt increases catalytic activity, while positive charge on the Pt decreases catalytic activity for CO oxidation.

3.2 Introduction

The development of more efficient catalysts depends on the ability to control electronic interactions for the selective enhancement of desired reaction pathways.[1-3] Driving catalytic chemistry with a charge flow already forms the basis of electrochemistry, photochemistry, and acid-base catalysis.[4-9] However, an unexplored approach to charge-mediated catalysis is to use a solid state device to externally control the catalyst electronic structure with an applied bias or a photo-induced current. In this work, we demonstrate the viability of using a Pt/Si nanodiode to control the rate of CO oxidation.

Many industrial catalysts consist of metal nanoparticles dispersed on a porous support. Because the support is often chemically inert without the metal, the metal is usually considered the active catalyst. However, numerous studies have demonstrated that the electronic properties of the support play a major role in determining the activity and selectivity of the metal/support system.[10-15] This complex interaction between a metal and its support has been widely studied and is commonly called the strong metal-support interaction (SMSI).[16-20] We are interested in SMSI because these interactions often give rise to highly active and selective reaction pathways.[3,21]

SMSI affects a wide range of catalytic reactions, including CO and CO_2 hydrogenation[19-21], CO oxidation[1,22-24], selective hydrogenation[25-27], and selective partial oxidation reactions.[2,28-30] We have recently demonstrated that for CO oxidation and methanol oxidation, the Pt/TiO_2 interaction is controlled by electron transfer from the TiO_2, which can be modified by chemical doping.[24,30]

The ability to control the electric field and charge flow at a metal/support interface using a solid state charge based device would provide nonthermal, electronic control of a catalytic reaction.[31-34] From SMSI studies, it is clear that charge flow at the metal/support interface has a major influence on the rate and selectivity of a catalytic reaction. If this approach is viable, solid

state device technology could soon find major applications in the field of catalysis for tunable control of selective surface chemistry.

The goal of activating nonthermal chemical processes electronically using a solid state device is an active area of research, and attempts to drive nonthermal surface chemistry have focused primarily on using a tunneling junction to emit hot electrons into a metal thin film.[31,35-41] When the thickness of the metal thin film is less than the mean free path of the hot electron, it is assumed that the electron reaches the surface before scattering to low energy electron hole pairs and subsequent lattice vibrations (a process that occurs in ~1 ps).[42] Several studies have demonstrated the ability of these hot electron emitters to induce a chemical reaction involving a single pre-adsorbed monolayer of reactant.[35-37] However, no reports have been made that demonstrate the ability to electronically activate a catalyst operating in steady state turnover by directly measuring the product yield.

We have previously reported the production of hot electron flow during CO oxidation using a catalytic nanodiode.[43,44] In that work a catalytic reaction was used to drive a current flow across a nanodiode. We demonstrate in this paper that the opposite is also possible: Using a catalytic nanodiode, an externally applied bias and a photo-induced current flow are used to control the rate of the catalytic reaction. We find that applying a negative charge to the Pt increases the reaction rate, while a flux of photo-induced positive charges to the Pt decreases the reaction rate. In both cases, the rate change is reversible under conditions of steady state turnover.

3.3 Experimental

To fabricate the catalytic Schottky diode, Pt was deposited on n-type Si (100) by electron beam evaporation. The n-type Si substrate was phosphorus doped to achieve a conductivity of 1–10 Ω cm. The Pt film was 4 nm thick as measured by quartz crystal microbalance. The chamber base pressure for electron beam deposition was $>1 \times 10^{-5}$ Torr. No etching of the Si native oxide was performed. We found that the native oxide did not act as a significant tunneling barrier to charge flow. This was verified by two observations: 1) linear ohmic contact to the n-Si with Al metal and 2) high photocurrent efficiency showing easy charge flow between the n-Si substrate and the Pt active area.

Using a shadow mask, the Pt was deposited as a 4 × 6 mm rectangle which served as the device active area. An aluminum (Al) pad provided ohmic contact to the n-type Si, and a gold (Au) pad provided contact to the Pt active area. Both the Al and Au contact pads were 100 nm thick. A layer of SiO_2 (150 nm) insulated the Au pad from the Si substrate. These Al, Au and SiO_2 layers were each deposited by electron beam evaporation using shadow masks.

A halogen lamp was used to illuminate the catalytic diode through a sapphire window on the reaction chamber. Lamp power was 1.35 W, the numerical aperture was 0.3, and the distance from the lamp to the diode was 8 cm. This resulted in approximately 60 mW/cm^2 of radiation over the active area of the diode. The spectral profile of the lamp closely followed the solar spectrum.

A batch mode reactor with a boron nitride substrate heater was used to determine activity of the catalytic diode for CO oxidation. A 2:5 ratio of CO to O_2 was used in the chamber in a background of He. A metal bellows circulation pump provided gas mixing. Reactions were performed at several temperatures between 423 and 443 K as measured by a type-K thermocouple. CO_2 production was monitored as a function of time using a gas chromatograph with a thermal conductivity detector.

Electrical connections were made between the contact pads of the device and BNC feedthroughs on the chamber using Au wire. Depending on the activity of the catalytic diode for a given reaction condition, up to three diodes were connected in parallel to increase the catalytic device area. A Keithley 2400 Sourcemeter was used to control the electrical bias across the device, measure photocurrent, and obtain IV curves of the device during reaction.

Reaction rates are reported in turnover frequency (TOF) as CO_2 molecules produced per Pt site per minute. All error bars represent the 95% confidence interval based on the rate of CO_2 production normalized to the estimated number of Pt sites. The number of Pt sites was estimated by assuming a uniform (111) surface structure over the entire catalyst area. Although this calculation is approximate, it provides a consistent normalization to the catalyst area and yields a reasonable estimate of the absolute TOF.

3.4 Results and Discussion

3.4.1 Electrical and Photo Properties of Catalytic Diode

The Pt served as the catalyst, and a Schottky barrier formed at the Pt/Si interface. The Pt film was 4 nm thick. We found this was thin enough to transmit visible light, so the device was also an efficient photodiode showing power conversion efficiency (PCE) of 1.5% and a spectrally averaged incident photon to current conversion efficiency (IPCE) of 15%. Fig. 1A shows the device architecture; Fig. 1B shows the current-voltage (IV) curves of the device in the dark and during illumination by a halogen lamp (~60 mW/cm^2) at room temperature. The spectral profile of the lamp closely followed the solar spectrum.

3.4.2 Bias Effect on Catalytic Activity

Fig. 2A shows the effect of applied bias on the catalytic activity of the device for CO oxidation. The experiment was performed in 40 Torr CO and 100 Torr O_2 at 443 K. Exposing the device to reaction conditions for approximately 10 h serves as a pretreatment necessary to observe a rate enhancement by bias. During the pretreatment, the device which is initially active in open circuit (i.e. no applied bias) deactivates as a result of Pt oxidation. Previous work has shown that the activity of the oxidized nanofilm can be reactivated by heating to 523 K in CO to reduce the Pt catalyst.[24] However, we find that although the oxidized Pt nanofilm is not active in open circuit, it responds to an applied bias. Following the pretreatment, we find that the catalyst activity can be enhanced by applying a reverse bias across the device. As shown in Fig. 2A this effect is reversible, so that the reaction rate can be turned on and off simply by switching the applied bias. In the experiment shown, a 1 V reverse bias is used to enhance the catalytic reaction rate, and the device is switched back and forth between an applied bias and an open circuit (i.e. no applied bias) state corresponding to high catalyst activity and no activity,

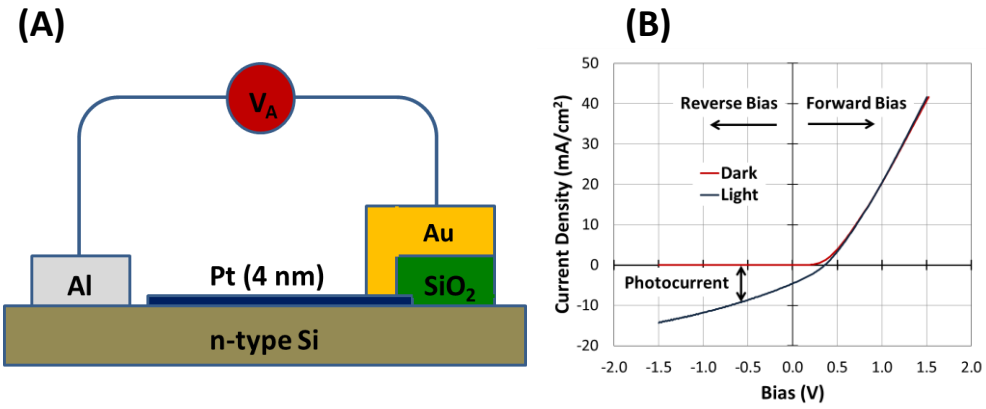

Fig. 1 (A) ***S****chematic of the catalytic nanodiode* **(B)** *IV curves of the catalytic nanodiode in the dark (red curve) and during illumination with visible light (blue curve) at room temperature. The light source is a halogen lamp emitting 60 mW/cm*^{2} *with a spectral profile similar to the solar spectrum.*

respectively. This effect was observed under steady-state turnover conditions for approximately 8 h.

We attempted to perform similar experiments to observe how the magnitude of applied bias affects the catalyst activity. For example, we may assume that applying a 0.5 V bias rather than a 1 V bias would result in a smaller rate enhancement, while a 2 V bias would yield a greater rate enhancement. The major challenge of this experiment is that the bias effect is sensitive to the oxidation state of the Pt nanofilm which is changing during reaction, and we find that the rate enhancement is more sensitive to the oxidation state of the catalyst than it is to the magnitude of the applied bias. Consequently, we could not quantify the magnitude of rate enhancement as a function of applied bias in a way that is statistically significant.

The direction of the applied bias is important because of the rectifying nature of the diode. A forward bias induces a current flow, and we find that under conditions of high current flow induced by a forward bias, the device is unstable in reaction. However, because of the Schottky barrier between the Pt and n-type Si, a reverse bias does not induce a current flow. Rather an electric field is generated at the Pt/Si interface with a negative charge build-up on the Pt and a positive charge build-up on the Si as shown in Fig. 2B. It appears that the negative charge on the Pt enhances catalytic activity. Our studies of hot electron flow during CO oxidation using a Pt/TiO_2 catalytic nanodiode could be explained by density functional theory showing that the reaction proceeds via a negatively charged CO_2^- transition state.[45] This finding implicates the important role of negatively charged reaction intermediates leading to a correlation of turnover rates with electron flow.[43,44] Accordingly, it is not surprising that generating negatively charged intermediates by external bias leads to an enhancement of the turnover rate.

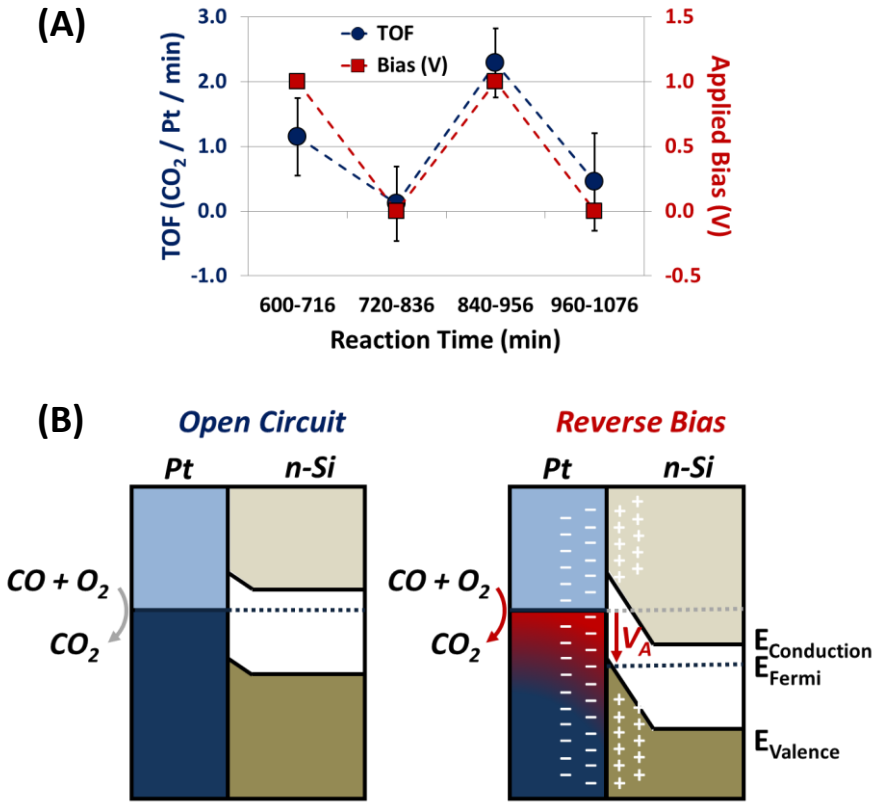

Fig. 2 (A) *Effect of bias on the catalytic activity of the nanodiode for CO oxidation. Red squares show the reverse bias that was externally applied to the device during CO oxidation. Blue circles show the corresponding turnover frequencies (TOF). The error bars represent 95% confidence intervals for the TOF measurements.* **(B)** *Band diagrams of the nanodiode in open circuit and during reverse bias. During reverse bias, positive charge builds-up on the Si and negative charge builds-up on the Pt. This increases band bending in the Si and results in a high electric field at the Pt/Si interface.*

3.4.3 Light Effect on Catalytic Activity

We also explored the possibility of using visible light to control the reaction rate by generating a photocurrent across the device. Fig. 3A shows the reaction rate for CO oxidation on the catalytic device first in the dark, then under illumination, then in the dark again. Fig. 3A also shows the corresponding photocurrent measurements made during the reaction. The results show that the photocurrent decreases the reaction rate by a factor of ~3. As with the bias, this effect is reversible, and the rate increases again when the light is turned off.

The photochemistry experiment was performed in 8 Torr CO and 20 Torr O_2 at 423 K. During this experiment, the reverse bias was kept fixed at 0.6 V. The role of the bias was to increase the reaction rate as well as the efficiency of photocurrent generation which scales with reverse bias. It is important to note that prior to the reaction, the device was subjected to an oxidizing pretreatment at 473 K. We found that the oxidizing pretreatment greatly increased the reaction rate at reverse bias (the same as in the above case showing a turnover rate increase by

external bias without light), and this pretreatment was necessary to observe an effect by light on the reaction rate. Again, this implicates the important role of Pt oxidation in observing an effect of charge flow on the catalytic reaction rate.

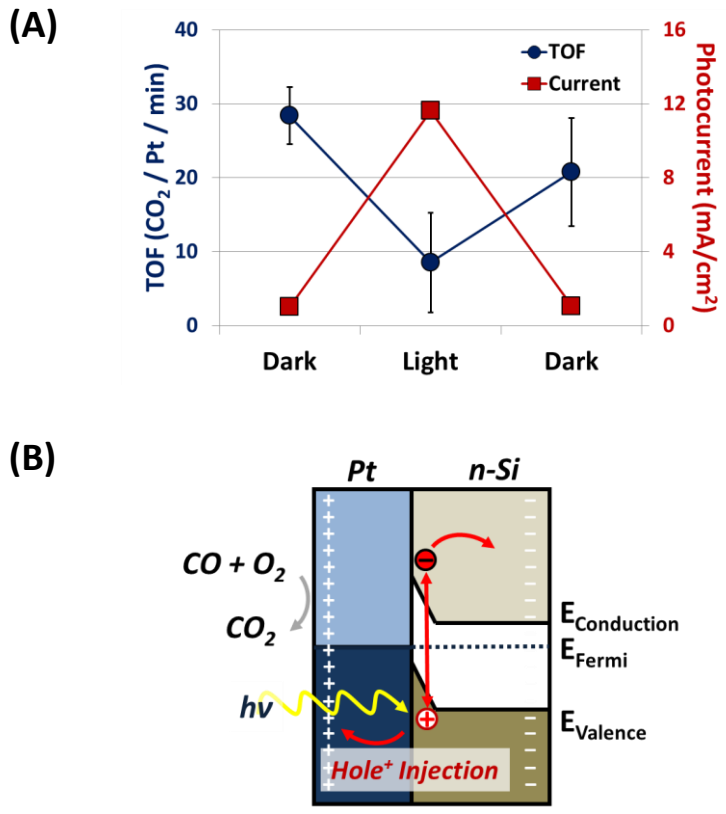

Fig. 3 (A) *Effect of photocurrent on the catalytic activity of the nanodiode for CO oxidation. Red squares show the current flow across the device in the dark and during illumination under reaction conditions. Blue circles show the corresponding TOF. The error bars represent 95% confidence intervals for the TOF measurements. During this experiment, the reverse bias was kept fixed at 0.6 V.* **(B)** *Band diagram of the device showing the mechanism of photocurrent generation. The 4 nm Pt film is thin enough to transmit visible which is absorbed in the Si, generating electron-hole pairs. Because of the interface potential, the holes move across the Pt/Si interface resulting in a flow of positive charge to the Pt surface.*

The mechanism of photocurrent flux is generation of an electron-hole pair in the Si followed by hole injection to the Pt as shown in Fig. 3B. Accordingly, photocurrent represents a flux of positive charge to the Pt catalyst and negative charge to the Si support. By bias we showed that a negative charge on the Pt increases the reaction rate; now we show that a flux of positive charge to the Pt decreases the reaction rate.

We found the chemical changes of the device under reaction conditions played an important role in determining both the bias effect and the photon effect. The bias effect shown in Fig. 2A was reversible for about 8 h prior to losing control of the device. The photon effect shown in Fig. 3A was shorter, lasting for only about 1 h. However, in both cases, the device was

effective long enough to control the chemistry for at least several hundred turnover events per active site. There appears to be a window in the oxidation state of Pt that shows a dramatic effect by bias and light on the catalytic activity for CO oxidation. At a lower oxidation state of the Pt nanofilm, the device is less sensitive to the applied bias and the photocurrent flux, while at a higher oxidation state, the catalytic activity to too low to measure. In both the bias and the light experiments, the device pretreatments were empirically optimized to yield the greatest effect by bias and light, and a detailed description of device hysteresis is discussed below.

3.4.4 Device Stability and Hysteresis

We found that the history of the device in various gas conditions played a major role in determining both the bias effect and the photon effect. Specifically, we observed switching behavior by the device induced by treatment in oxidizing conditions, especially during forward bias. Fig. 4 shows the IV curve of the device under reaction conditions initially and again following extended time in reaction conditions. We find that the same switching occurs following extended treatment in pure O_2 at reaction temperature (443 K). The initial state of the device, which we call state A, is characterized by a high forward bias current and good rectification. The final state of the device, which we call state B, is characterized by a low forward bias current and an almost symmetrical IV curve with respect bias. We found that the longer the device was exposed to oxidizing conditions, the more likely it was to fall into state B, although, there were several instances that we were able to induce a switch back to state A for a short amount of time by applied bias.

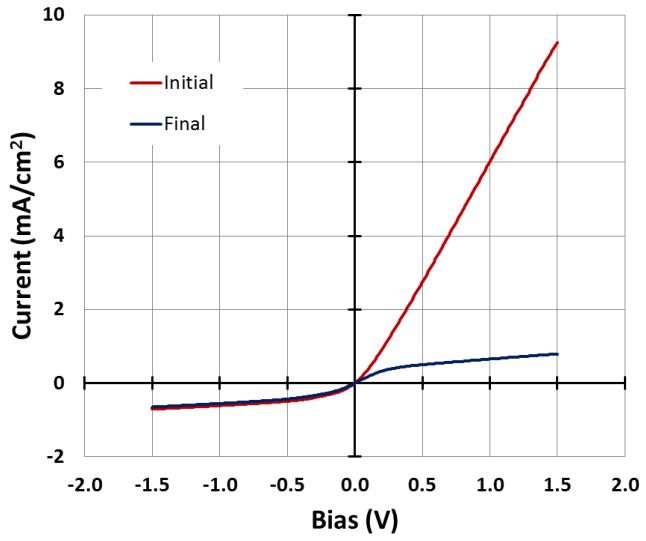

Fig. 4 *Current-voltage curves of the device initially and after extended time in reaction conditions.*

Forward bias seems to promote the switching behavior. Fig. 5 shows a current-time (IT) curve of the device under reaction condition at a fixed forward bias. The sudden drop in current at 14 s indicates the switch from state A to B. Fig. 6 shows the same type of switch occur during an IV curve measurement where at 0.7 V forward bias, the device suddenly switches from state A to B. The switch from state A to B corresponds to the incorporation of subsurface O into the

Pt catalyst. This explains why extended treatment in oxidizing conditions is necessary to induce the switch and explains the drop in forward bias conductivity after the switch.

We find that the switch also corresponds with a major change in the catalytic behavior of the device. Fig. 7 shows the reaction rate measured over time while the device is alternated between open circuit and a 1 V reverse bias. Each time the bias was changed, the IV curve of the device was measured to determine its state, and the switch from state A to B occurred at 596 min of time in reaction. Before the switch, we find that the device is catalytically active in open circuit, and the activity is decreased when a reverse bias is applied. However, after the switch, the device is inactive in open circuit, and the activity is increased when a reverse bias is applied.

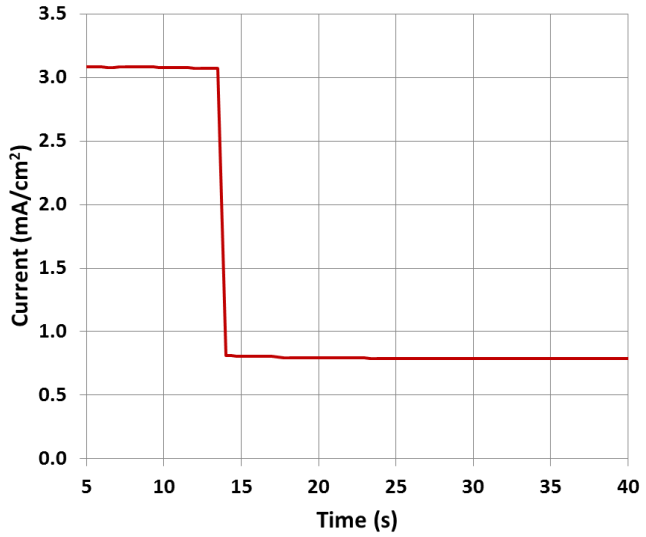

Fig. 5 *Current-time curve at 1 V forward bias showing a sudden switch of the device from its initial conductive state to an insulating state.*

We suggest the following explanation: Initially the Pt is metallic and the CO oxidation reaction is rate limited by activation of the Pt-C bond of the adsorbed CO. It was recently demonstrated by Wolf and coworkers that in a similar Pt/TiO_2 Schottky diode system, a reverse bias results in a red shift of the vibration frequency of adsorbed CO.[34] This red shift corresponds to electron back donation to the π^* orbital of the CO. This orbital is anti-bonding with respect to C-O, but is bonding with respect to Pt-C. Consequently, we can assume that the effect of reverse bias is to weaken the C-O bond but to strengthen the Pt-C bond. On metallic Pt where the reaction rate is limited by activating adsorbed CO, strengthening the Pt-C bond by reverse bias results in a decreased reaction rate.

However, the reaction kinetics change upon incorporation of subsurface O in the Pt. In this case, the reaction proceeds via a Mars-van Krevelen mechanism in which adsorbed CO reacts with O in the Pt lattice, and Pt-O bond activation is rate limiting. Our group and others have demonstrated that metal-O bond activation occurs by negative charge.[24,42,46] This explains why in state B, the device is only active when a negative bias is applied to the Pt, and the activity decreases during illumination when a flux of positive charge moves from the Si substrate to the Pt surface.

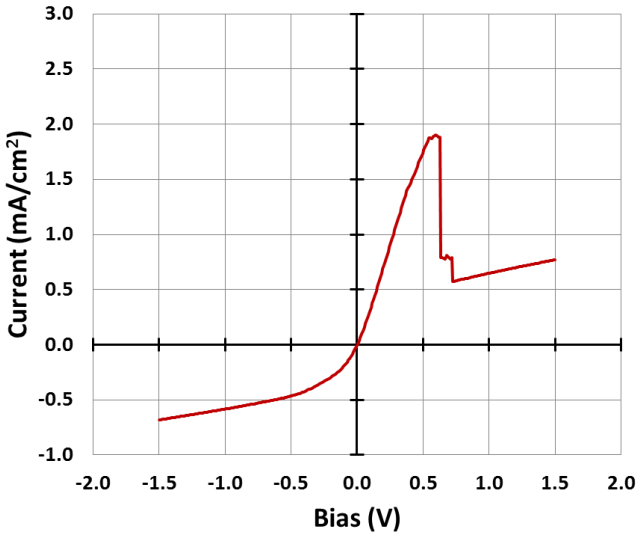

Fig. 6 *Current-voltage curve of the device showing a sudden switch from a conductive state to an insulating state at 0.7 V forward bias.*

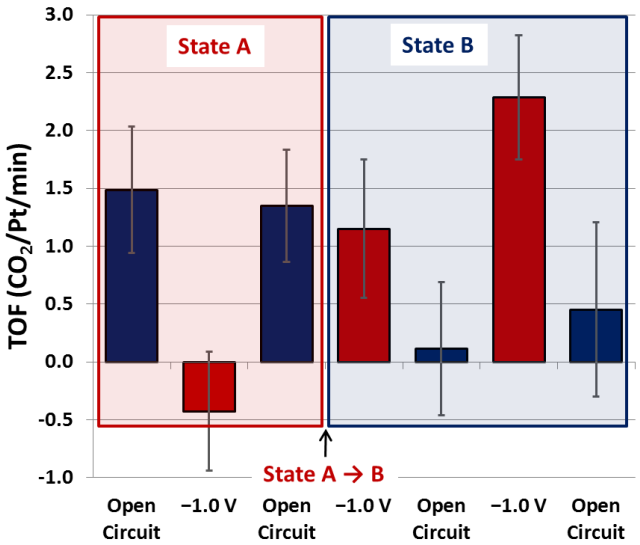

Fig. 7 *Turnover frequency (TOF) for CO oxidation on the catalytic diode as the bias is switched between open circuit and 1 V reverse bias. Between each TOF measurement a current-voltage curve is measured to determine the state of the device. A switch occurs from state A (conductive) to state B (insulating) during the experiment. We find that the effect of bias on catalytic activity depends strongly on the state of the device.*

3.5 Conclusions

This work demonstrates direct control of catalytic CO oxidation using a catalytic nanodiode. This is the first time that a charge-based device has been shown to provide external control of a surface catalytic reaction as determined by measuring the product yield, and this was achieved using both applied bias and visible light. Based on these results, we believe that

charge-based device technology will be further developed for catalytic applications in energy conversion and selective chemistry.

3.6 References

(1) Chen, M. S.; Goodman, D. W. *Science* **2004**, *306*, 252.
(2) Enache, D. I.; Edwards, J. K.; Landon, P.; Solsona-Espriu, B.; Carley, A. F.; Herzing, A. A.; Watanabe, M.; Kiely, C. J.; Knight, D. W.; Hutchings, G. J. *Science* **2006**, *311*, 362.
(3) Yamada, Y.; Tsung, C.-K.; Huang, W.; Huo, Z.; Habas, S. E.; Soejima, T.; Aliaga, C. E.; Somorjai, G. A.; Yang, P. *Nat Chem* **2011**, *3*, 372.
(4) Fujishima, A.; Honda, K. *Nature* **1972**, *238*, 37.
(5) Ni, M.; Leung, M. K. H.; Leung, D. Y. C.; Sumathy, K. *Renewable and Sustainable Energy Reviews* **2007**, *11*, 401.
(6) Osterloh, F. E. *Chemistry of Materials* **2007**, *20*, 35.
(7) Jencks, W. P. *Accounts of Chemical Research* **1980**, *13*, 161.
(8) Greeley, J.; Norskov, J. K.; Mavrikakis, M. *Annu. Rev. Phys. Chem.* **2002**, *53*, 319.
(9) Olah, G. A.; Molnar, A. *Hydrocarbon Chemistry*; 2nd Edition ed.; John Wiley & Sons, Inc.: Hoboken, NJ, 2003.
(10) Herrmann, J. M.; Pichat, P. *Journal of Catalysis* **1982**, *78*, 425.
(11) Meriaudeau, P.; Ellestad, O. H.; Dufaux, M.; Naccache, C. *Journal of Catalysis* **1982**, *75*, 243.
(12) Sexton, B. A.; Hughes, A. E.; Foger, K. *Journal of Catalysis* **1982**, *77*, 85.
(13) Resasco, D. E.; Haller, G. L. *Journal of Catalysis* **1983**, *82*, 279.
(14) Benvenutti, E. V.; Franken, L.; Moro, C. C.; Davanzo, C. U. *Langmuir* **1999**, *15*, 8140.
(15) Jochum, W.; Eder, D.; Kaltenhauser, G.; Kramer, R. *Top Catal* **2007**, *46*, 49.
(16) Schwab, G. M. *Transactions of the Faraday Society* **1946**, *42*, 689.
(17) Tauster, S. J.; Fung, S. C.; Garten, R. L. *Journal of the American Chemical Society* **1978**, *100*, 170.
(18) Tauster, S. J.; Fung, S. C.; Baker, R. T. K.; Horsley, J. A. *Science* **1981**, *211*, 1121.
(19) Tauster, S. J. *Accounts of Chemical Research* **1987**, *20*, 389.
(20) Somorjai, G. A.; Li, Y. *Introduction to surface chemistry and catalysis*; 2nd Edition ed.; Johns Wiley & Sons, Inc.: Hoboken, NJ, 2010.
(21) Boffa, A.; Lin, C.; Bell, A. T.; Somorjai, G. A. *Journal of Catalysis* **1994**, *149*, 149.
(22) Oh, S. H.; Eickel, C. C. *Journal of Catalysis* **1988**, *112*, 543.
(23) Goodman, D. *Catalysis Letters* **2005**, *99*, 1.
(24) Baker, L. R.; Hervier, A.; Seo, H.; Kennedy, G.; Komvopoulos, K.; Somorjai, G. A. *The Journal of Physical Chemistry C* **2011**, *115*, 16006.
(25) Vannice, M. A.; Sen, B. *Journal of Catalysis* **1989**, *115*, 65.
(26) Lin, S. D.; Sanders, D. K.; Albert Vannice, M. *Applied Catalysis A: General* **1994**, *113*, 59.
(27) Malathi, R.; Viswanath, R. P. *Applied Catalysis A: General* **2001**, *208*, 323.
(28) Edwards, J. K.; Solsona, B. E.; Landon, P.; Carley, A. F.; Herzing, A.; Kiely, C. J.; Hutchings, G. J. *Journal of Catalysis* **2005**, *236*, 69.
(29) Nakagawa, K.; Ikenaga, N.; Suzuki, T.; Kobayashi, T.; Haruta, M. *Applied Catalysis A: General* **1998**, *169*, 281.
(30) Hervier, A.; Baker, L. R.; Komvopoulos, K.; Somorjai, G. A. *The Journal of Physical Chemistry C* **2011**.

(31) Gadzuk, J. W. *Phys Rev Lett* **1996**, *76*, 4234.
(32) Gergen, B.; Nienhaus, H.; Weinberg, W. H.; McFarland, E. W. *Science* **2001**, *294*, 2521.
(33) Zhang, Y.; Kolmakov, A.; Chretien, S.; Metiu, H.; Moskovits, M. *Nano Letters* **2004**, *4*, 403.
(34) Deshlahra, P.; Schneider, W. F.; Bernstein, G. H.; Wolf, E. E. *Journal of the American Chemical Society* **2011**, *133*, 16459.
(35) Sharpe, R. G.; Dixon-Warren, S. J.; Durston, P. J.; Palmer, R. E. *Chemical Physics Letters* **1995**, *234*, 354.
(36) Wadayama, T.; Kojim, A.; Hatta, A. *Applied Physics A: Materials Science & Processing* **2004**, *79*, 1891.
(37) Wadayama, T.; Yokawa, M. *Chemical Physics Letters* **2006**, *428*, 348.
(38) Diesing, D.; Janssen, H.; Otto, A. *Surface Science* **1995**, *331–333, Part A*, 289.
(39) Diesing, D.; Kritzler, G.; Stermann, M.; Nolting, D.; Otto, A. *Journal of Solid State Electrochemistry* **2003**, *7*, 389.
(40) Thomsen, L. B.; Nielsen, G.; Vendelbo, S. B.; Johansson, M.; Hansen, O.; Chorkendorff, I. *Physical Review B* **2007**, *76*, 155315.
(41) Ray, M. P.; Lake, R. E.; Thomsen, L. B.; Nielson, G.; Hansen, O.; Chorkendorff, I.; Sosolik, C. E. *Journal of Physics: Condensed Matter* **2010**, *22*, 084010.
(42) Bonn, M.; Funk, S.; Hess, C.; Denzler, D. N.; Stampfl, C.; Scheffler, M.; Wolf, M.; Ertl, G. *Science* **1999**, *285*, 1042.
(43) Park, J. Y.; Somorjai, G. A. *Chemphyschem* **2006**, *7*, 1409.
(44) Hervier, A.; Renzas, J. R.; Park, J. Y.; Somorjai, G. A. *Nano Letters* **2009**, *9*, 3930.
(45) Maximoff, S. N.; Head-Gordon, M. P. *Proceedings of the National Academy of Sciences* **2009**, *106*, 11460.
(46) Zhang, Z.; Yates, J. T. *Journal of the American Chemical Society* **2010**, *132*, 12804.

Chapter 4

Controlling the Rate of Hydrogen Oxidation on Platinum/Silicon Catalytic Nanodiodes by Photocurrent Generation with Visible Light

4.1 Abstract

We report here that turnover frequency of hydrogen oxidation on a Pt/TiO_2 nanodiode can be decreased by exposing the device to visible light. The magnitude of this effect could not be measured accurately, since the heater used for the experiment desorbed a measurable amount of hydrogen under illumination, which interfered with the measurement. However, applying a reverse bias to the device enhances the effect of light, indicating that the light is in fact modifying catalysis on the surface of the diode.

4.2 Introduction

Solar energy is an increasingly attractive alternative to fossil fuels, but it presents the major disadvantage of only being available during the day. One of the solutions to this problem is to use solar energy to drive a chemical reaction on a photocatalytic device. The reaction product can then be used to regenerate electricity when solar energy is unavailable, or as transportation or heating fuel.[1] The device must be able to generate electron–hole pairs from visible light, separate those charges in order to avoid their recombination, and finally use the electrons, the holes, or both to drive a chemical reaction. This is often achieved by placing catalytic particles in contact with a photovoltaic assembly, where it can collect electrons and holes, all of this on the nanoscale.[2-5]

A typical solar cell uses a p–n junction to separate charges, but nanodiodes have been proposed as an alternative architecture.[6] The Schottky barrier at a metal–oxide interface serves the role of the charge separator. Depending on the direction of the band bending, electrons or holes are injected into the metal, where they can affect surface chemistry. These charges have overcome the Schottky barrier, and have energies in significant excess of the Fermi level. If the metal is thinner than their mean free path, these charges may interact with adsorbates before they relax, providing additional energy to do chemistry. This idea of collecting charge carriers while they are still hot has already been suggested for purely photovoltaic solar cells as a strategy for increasing efficiency.[7]

We report here that a 4 nm Pt film deposited on Si acts as a photodiode and that its catalytic activity can be affected by light. Visible light excites electron-hole pairs in Si, and the holes are injected into Pt. We show that under hydrogen oxidation conditions, the rate of formation of water is decreased under illumination, indicating that the flow of charges to the surface interferes with the reaction mechanism. Unfortunately, illumination of the diode also caused the boron nitride sample heater to desorb H_2 into the reactor. Becuase the reaction rate

was measured by following the decrease in the amount of H_2 by gas chromatography, this artifact interfered with the observation of the effect of light on the diode.

Nonetheless, the effect of light is enhanced by applying a reverse bias to the Pt/Si diode, which shows that some of the change in reactivity can be attributed to the effect of light.

4.3 Experimental

To fabricate the catalytic Schottky diode, Pt was deposited on n-type Si (100) by electron beam evaporation. The n-type Si substrate was phosphorus doped to achieve a conductivity of 1–10 Ω cm. The Pt film was 4 nm thick as measured by quartz crystal microbalance. The chamber base pressure for electron beam deposition was $>1 \times 10^{-5}$ Torr. No etching of the Si native oxide was done prior to Pt deposition, because the native oxide acted as a tunneling barrier to increase the rectification of the diode. Using a shadow mask, the Pt was deposited as a 4×6 mm rectangle which served as the device active area.

An aluminum (Al) pad provided ohmic contact to the n-type Si, and a gold (Au) pad provided contact to the Pt active area. Both the Al and Au contact pads were 100 nm thick. A layer of SiO_2 (150 nm) insulated the Au pad from the Si substrate. These Al, Au and SiO_2 layers were each deposited by electron beam evaporation using shadow masks.

The nanodiode is placed on a ceramic heater, and the temperature is monitored by a thermocouple, fluctuating by less than 0.5 K. The turnover of water molecules was obtained by monitoring the amount of H_2 during the reaction, using a gas chromatograph connected to the chamber by a sample loop equipped with a metal bellows circulation pump. Hydrogen oxidation was carried out in 10 Torr H_2, 30 Torr O_2, and 720 Torr He, at 423 K. Prior to reaction, samples were heated to 423 K in 100 Torr O_2 for one hour. This pretreatment led to increased turnover, facilitating the measurements.

The nanodiode's electrodes are connected to an electrical circuit with gold wires, making it possible to characterize the device by measuring its IV curve. This was done with a Keithley Sourcemeter, which was also used to measure chemicurrent passing through the diode while the chemical reaction is taking place. No voltage bias is applied to the diode.

A halogen lamp was used to illuminate the catalytic diode through a sapphire window on the reaction chamber. Lamp power was 1.35 W, the numerical aperture was 0.3, and the distance from the lamp to the diode was 8 cm. This resulted in approximately 60 mW/cm^2 of radiation over the active area of the diode. The spectral profile of the lamp closely followed the solar spectrum. On a typical diode, current at 443 K was on the order of 0.5 mA in dark conditions, and 1.5 mA under illumination, for an active area of 24 mm^2. Current in dark conditions is likely due to thermionic emission from Pt to Si.

4.4 Results and Discussion

Fig. 1 shows the rate of hydrogen oxidation on a Pt/Si diode, measured by gas chromatography, in the dark and under illumination at 423 K. Before each on/off cycle, the reactor was evacuated down to a pressure of 10^{-5} Torr, and the mixture introduced was

comprised of 10 Torr H_2, 30 Torr O_2 and 740 Torr N_2. The rate under illumination is consistently lower than in the dark.

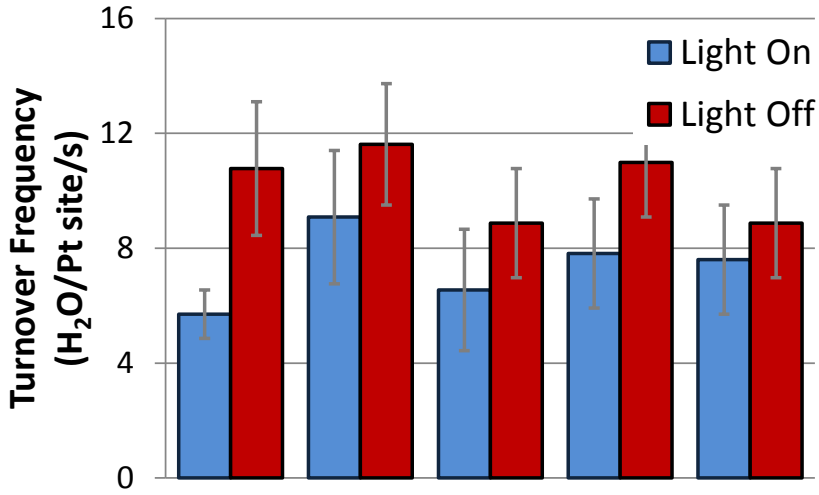

Fig. 1 *Turnover frequency of hydrogen oxidation in 10 Torr H_2, 30 Torr O_2 and 740 Torr He at 423 K. Turnover is calculated based on the rate of decrease of the hydrogen peak height in the chromatogram. In between each on/off cycle, the chamber was pumped down to 10^{-5} Torr. Error bars represent 95% confidence intervals.*

As a control experiment, the same procedure was carried out in the absence of O_2. In these conditions, no reaction is occurring on the surface of the diode, and yet fluctuations in the H_2 concentration in the reactor still correlate with light exposure, as shown in Fig. 2. These fluctuations disappeared when the boron nitride sample heater was covered in aluminum foil, suggesting that the heater takes up H_2, and desorbs it continuously under illumination.

Any effect on the reaction from illuminating the diode cannot be separated from this artifact. However, since the diode is connected into a circuit through electrical feedthroughs on the reactor, it can be subjected to a voltage bias. In another set of experiments, H_2 oxidation was performed in the same conditions while different voltage biases were applied to the diode. Fig. 3 shows the rates under illumination and in the dark at 0, −0.6, −0.3 and −0.9 V. Again, the rates under illumination are lower than in the dark, but the ratio between the two decreases with applied bias. The ratio of the light on rate to the light off rate is plotted versus voltage in the graph in Fig. 4.

Turnover rates tend to change over time: the active surface area and the surface coverage may change as a poison takes up surface sites, and the film may anneal or oxidize under the harsh conditions used for the reaction. To avoid confusing any of these effects with the effect from bias, the voltages were not applied in decreasing order, but instead in the following order: 0, −0.6, −0.3 and −0.9 V. The decrease in turnover by light is enhanced with greater reverse bias. A final measurement was then performed at 0 V again, and showed a value similar to the initial 0 V measurement.

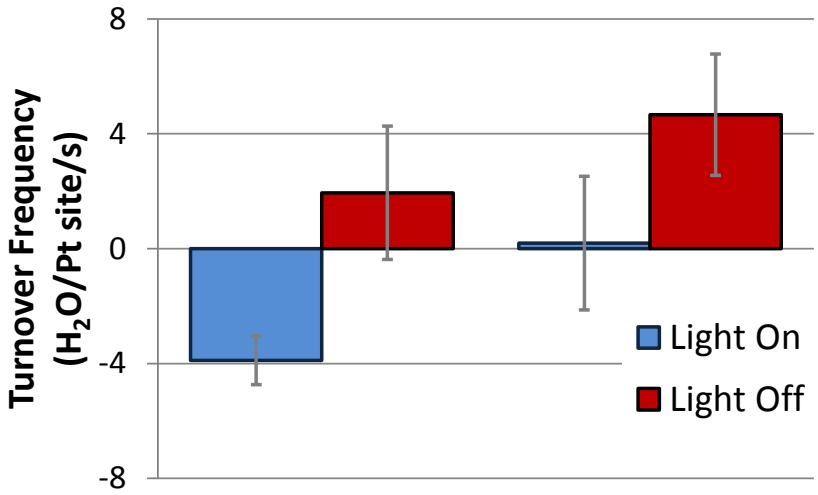

Fig. 2 *Turnover frequency of hydrogen oxidation in 10 Torr H_2, 770 Torr He and no O_2 at 423 K. In the absence of O_2, there should be no turnover, and the non-zero values observed are the result of H_2 leaking from the reactor, reacting with traces of O_2, and desorbing from the heater under illumination.*

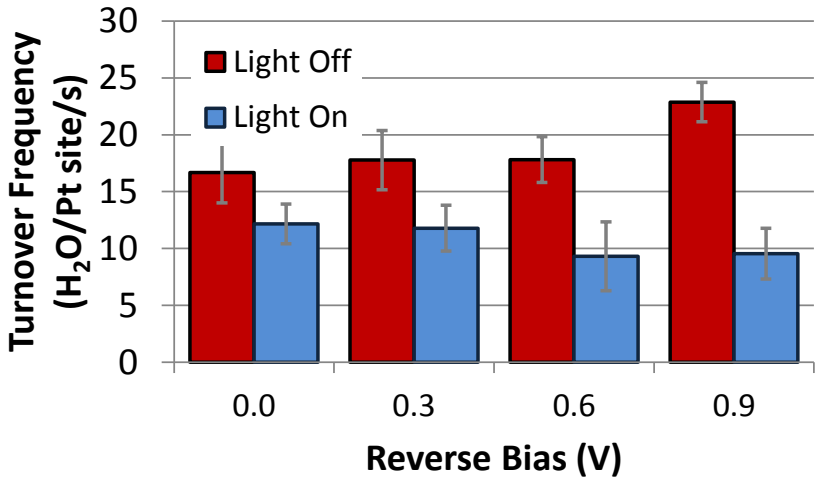

Fig. 3 *Turnover frequency for hydrogen oxidation in 10 Torr H_2, 30 Torr O_2 and 740 Torr He at 423 K, over a series of on / off cycles with different bias voltages applied to the diode. In order to avoid artifacts in device history, the chronological order of the voltages applied was 0 V, −0.6 V, −0.3 V and −0.9 V.*

The effect from bias shows that the light does affect the surface chemistry of the diode. The Pt film is 4 nm thick, and transmits most of the light through to the Si substrate. Si, with its bandgap of 1.1 eV, absorbs visible light, resulting in the formation of electron hole pairs.[8] The direction of band bending in a Pt/n-Si is such that excited electrons in the conduction band remain in the silicon, while excited holes are accelerated towards the metal.

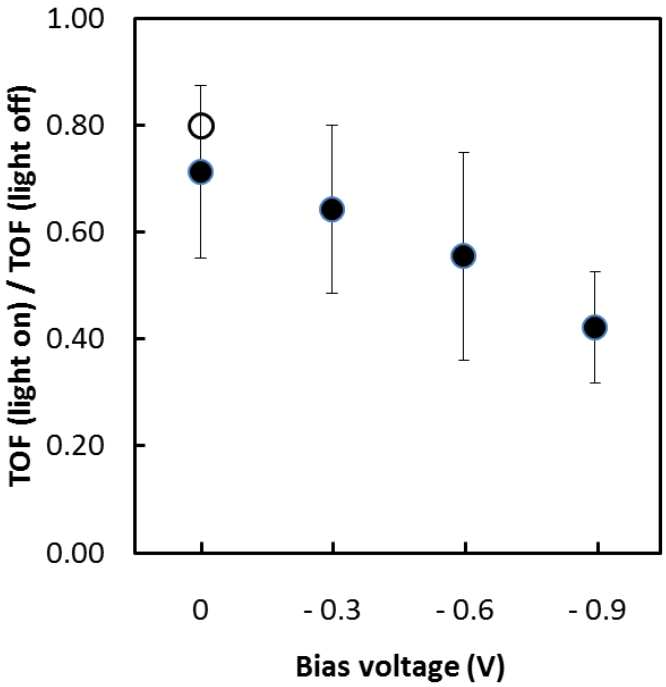

Fig. 4 *Ratio of turnover frequency under illumination to turnover frequency in the dark at different bias voltages, calculated from the values plotted in Fig. 3 (full circles). Empty circle represents a final on/off cycle at 0 V carried out after the four others.*

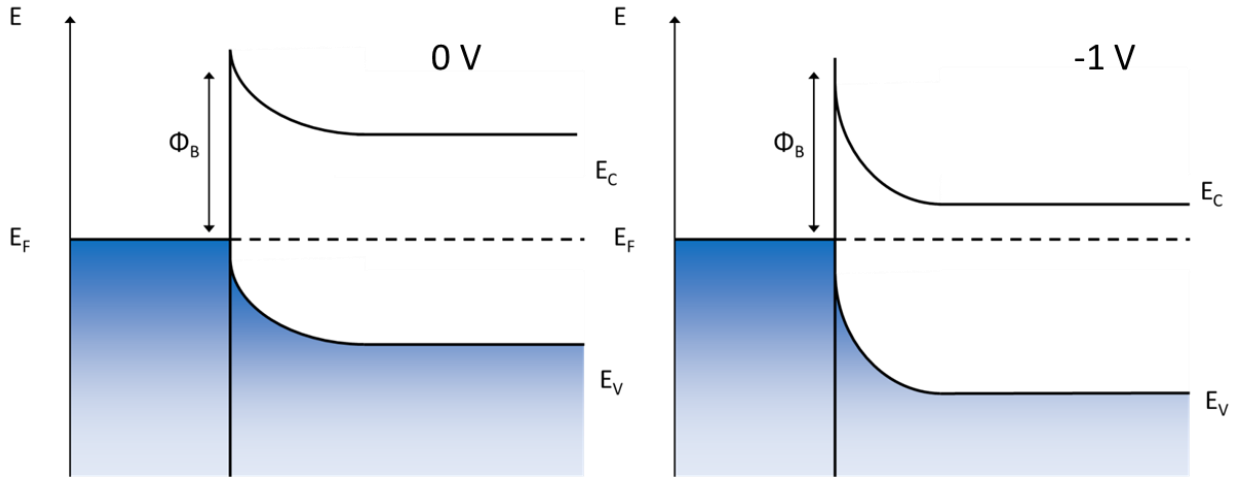

Fig. 5 *Schematic band energy diagrams for a Pt/Si diode at 0 V and −1V voltage biases, respectively.*

The Si wafers used were covered in an insulating layer of SiO_2 several nanometers thick. The bandgap of SiO_2 is 9 eV, so excited holes in Si must tunnel through this native oxide to reach the Pt film.[9] This decreases the efficiency of the diode. The SiO_2 film can be etched away with HF. However, this film grows back to 1 nm thickness in air in only 1 hour.[10] Fabricating a diode with no tunneling barrier for the holes is therefore quite difficult. Because photocurrent

obtained with the native oxide present is substantial enough to affect the catalysis, no attempt was made to remove it.

Illuminating the diode would also increase its temperature, from photon absorption, and from Joule heating due to the photocurrent. This can safely be ruled out as a cause of the change in turnover, since an increase in temperature under illumination would increase turnover, not decrease it.

It would be useful to know the efficiency of the process by which light hinders turnover in order to understand the mechanism at play. The efficiency for generation of photocurrent in the diode is known, as is the number of reaction events occurring on the surface. It would therefore be possible to know how many reaction events are prevented for each hole that is injected from Si into Pt. Desorption of H_2 from the sample heater unfortunately prevents us from making this calculation, and more experiments are needed to better understand this phenomenon. Chapter 6 covers similar, more succesful experiments performed with CO oxidation.

4.5 Conclusions

Despite the sample heater interfering with the results, we have shown that turnover for hydrogen oxidation can be significantly reduced on a Pt/TiO_2 photodiode by exposing the diode to visible light. This is not due to heating of the catalyst under illumination, but instead to a steady-state flow of hot holes to the surface. The mechanism for this process is not well understood, and further experiments are required. Without the effect of H_2 desorbing from the heater under illumination, it would be possible to calculate the efficiency for this process, which would be useful in understanding the mechanism. A comparison of D_2 and H_2 oxidation would also be particularly useful in this regard.

This work shows that a catalytic device can be designed that allows us to tune surface chemistry with light. Using different diode materials, and with a different reaction, it may be possible to use light to increase activity, or achieve higher selectivity in the case of a multi-path reaction.

4.6 References

(1) Lewis, N. S.; Nocera, D. G. *Proceedings of the National Academy of Sciences* **2006**, *103*, 15729.
(2) Yan, H.; Yang, J.; Ma, G.; Wu, G.; Zong, X.; Lei, Z.; Shi, J.; Li, C. *Journal of Catalysis* **2009**, *266*, 165.
(3) Amirav, L.; Alivisatos, A. P. *J. Phys. Chem. Lett.* **2010**, *1*, 1051.
(4) Maeda, K.; Xiong, A.; Yoshinaga, T.; Ikeda, T.; Sakamoto, N.; Hisatomi, T.; Takashima, M.; Lu, D.; Kanehara, M.; Setoyama, T.; Teranishi, T.; Domen, K. *Angewandte Chemie International Edition* **2010**, *49*, 4096.
(5) Zong, X.; Han, J.; Ma, G.; Yan, H.; Wu, G.; Li, C. *J. Phys. Chem. C* **2011**, *115*, 12202.
(6) McFarland, E. W.; Tang, J. *Nature* **2003**, *421*, 616.
(7) Ross, R. T. *Journal of Applied Physics* **1982**, *53*, 3813.
(8) Kittel, C. *Introduction to solid state physics*; Wiley, 2005.

(9) DiStefano, T. H.; Eastman, D. E. *Solid State Communications* **1971**, *9*, 2259.
(10) Raider, S. I.; Flitsch, R.; Palmer, M. J. *Journal of The Electrochemical Society* **1975**, *122*, 413.

Chapter 5

Generation of Highly n-Type Titanium Oxide Using Plasma Fluorine Insertion

5.1 Abstract

True n-type doping of titanium oxide without formation of mid-gap states would expand the use of metal oxides for charge-based devices. We demonstrate that plasma-assisted F insertion passivates defect states and that fluorine acts as an n-type donor in titanium oxide. This enabled us to modify the Fermi level and transport properties of titanium oxide outside the limits of O vacancy doping. The origin of the electronic structure modification is explained by ab initio calculation.

5.2 Introduction

The application of transition metal oxide (TMO) semiconductors for charge-based devices is becoming prevalent for chemical, electrical, and energy applications.[1–3] Among TMOs, titanium oxide has been widely studied for photocatalysis,[4] light harvesting,[5] resistive switching memory,[6] and chemical sensing,[7] as an intrinsic n-type semiconductor. The charge transport/transfer in titanium oxide is highly sensitive to O vacancy defects that exist as the lattice bonding defects in single-crystals and as surface and grain boundary defects in polycrystalline films.[8] In previous studies, O vacancies, equivalent to Ti^{3+} states, have been used as intrinsic donors to create a transport channel for increased conductivity.[9,10]

O vacancies give rise to partially occupied Ti^{3+} states below the conduction band (CB) edge and act as n-type donors. Consequently, limited control of titanium oxide conductivity and Fermi level (E_F) is possible by the manipulation of O vacancies. However, the intrinsic doping of titanium oxide through Ti^{3+} defect sites is equivalent to the formation of a reduced oxide. Although, the reduced oxide is often highly conductive, Ti^{3+} mid-gap states act as a barrier to CB transport and result in E_F pinning.[11] Additionally, the electric activity (e.g. charge trapping) and chemical reactivity of O vacancies create problems for material reliability. Consequently, highly conductive titanium oxide is seldom useful for device architecture, and fabrication of highly conductive, defect-free titanium oxide remains an important challenge.

The extrinsic chemical doping of titanium oxide using impurity dopants (e.g. N, S, and C) by colloidal synthesis methods to modify the electronic structure and achieve visible light absorption has been actively studied for photocatalytic applications.[12,13] Additionally, metal impurity (e.g. V, Ni, and Nb) doping to titanium oxide has been used to modify E_F and increase the conductivity.[14,15] However, in each of these cases, the semiconductor properties of titanium oxide are compromised by the formation of metallic mid-gap states. To the best of our knowledge, no one has reported n-type doping of a metal oxide without simultaneously decreasing the bandgap. This ability would be analogous to phosphorus or arsenic doping of silicon where carrier concentration is changed without significant band structure modification.

Here we report the use of plasma-assisted F insertion to passivate defects and act as an extrinsic n-type donor in titanium oxide. Electrical analysis shows that F insertion is an excellent method to achieve highly conductive, low defect titanium oxide suitable for TMO device applications. Theoretical calculations also investigate the concept of n-type doping to metal oxides by F insertion and suggest the mechanism by which F generates a highly conductive surface channel.

5.3 Experimental

Titanium oxide films were deposited by direct current magnetron sputtering. During sputtering, plasma power was 400 W, bias voltage was 450 V, Ar flow was 50 SCCM, and O_2 flow was 3 SCCM. Two different film thicknesses and substrates were used in this work: 100 nm films deposited on an insulating substrate and 10 nm films deposited on highly doped (0.01–0.02 Ω·cm) p-type Si (100) with native oxide. As deposited, the titanium oxide films were highly O deficient.

Rapid thermal annealing (RTA) was then used to tune the O vacancy concentration. Three pre-conditions were prepared for F insertion with sub-oxide concentrations ranging from 41 to < 3% (measured as the ratio of Ti^{4+} to Ti^{3+} peak areas in the Ti 2p XPS spectrum). To achieve this distribution of sub-oxide concentrations, all samples were first annealed in N_2 at 500 °C to increase crystallinity. Following RTA in N_2, annealing in O_2 at different temperatures served to increase the O stoichiometry in the film. No O_2 annealing produced films with 41% sub-oxide; RTA in O_2 at 350 °C produced films with 8% sub-oxide; and RTA in O_2 at 500 °C produced films with <3% sub-oxide. It should be noted that the actual stoichiometries varied from one deposition to another. Consequently, all results reported here are taken from a single deposition. Although the exact values may vary, the trends reported are consistent between depositions.

F insertion was achieved by plasma treatment in N_2 gas with trace SF_6. Trace SF_6 was introduced into the chamber by flowing a 9:1 mixture of SF_6 and O_2 followed by pumping to chamber base pressure (5 mTorr). After pumping, a small background pressure of SF_6 remained in the chamber. N_2 gas was then introduced at 80 SCCM for plasma treatment. Plasma power was 20 W with 130 V DC substrate bias. F concentration is tunable with the length of the plasma treatment.

X-ray photoelectron spectroscopy (XPS) was used to analyze the chemical binding states and valence band edge of the titanium oxide films (Physical Electronics, PHI 5400 ESCA/XPS system with an Al anode source at 1486.6 eV). The energy resolution for each point is 0.05 eV. The analyzer was positioned at 50 degrees relative to sample normal. All binding energies were calibrated to the C 1s peak state.

The real and imaginary parts of the complex dielectric constant, $\varepsilon_c = \varepsilon_1 + i\varepsilon_2$, and absorption coefficients for titanium oxide samples were determined by visible-ultra violet spectroscopic ellipsometry in a rotating compensator enhanced spectrometer. The monochromatic light source from a Xenon lamp at photon energies of 1.5–6 eV was used with spectral resolution of 15 meV.

Two types of electrical measurements were made. First, current-voltage (IV) curves were measured for 10 nm titanium oxide films on highly doped p-Si. Second, surface resistivity was measured for 100 nm titanium oxide films on insulating supports. Ohmic contact was made to the titanium oxide using thin film electrodes consisting of 10 nm Ti and 100 nm Au. For the TiO_2/p-Si heterojunction devices, ohmic contact was made to the backside of p-Si with 30 nm Pt. All metals were deposited by electron beam evaporation. Measurements were made with a Keithley 2400 sourcemeter.

5.4 Results and Discussion

Based on the relative intensities of the Ti^{3+} and Ti^{4+} states in the Ti 2p XPS spectrum, we refer to the three pre-conditions to F insertion as $TiO_{1.7}$, $TiO_{1.9}$, and TiO_2 (see Fig. 1).

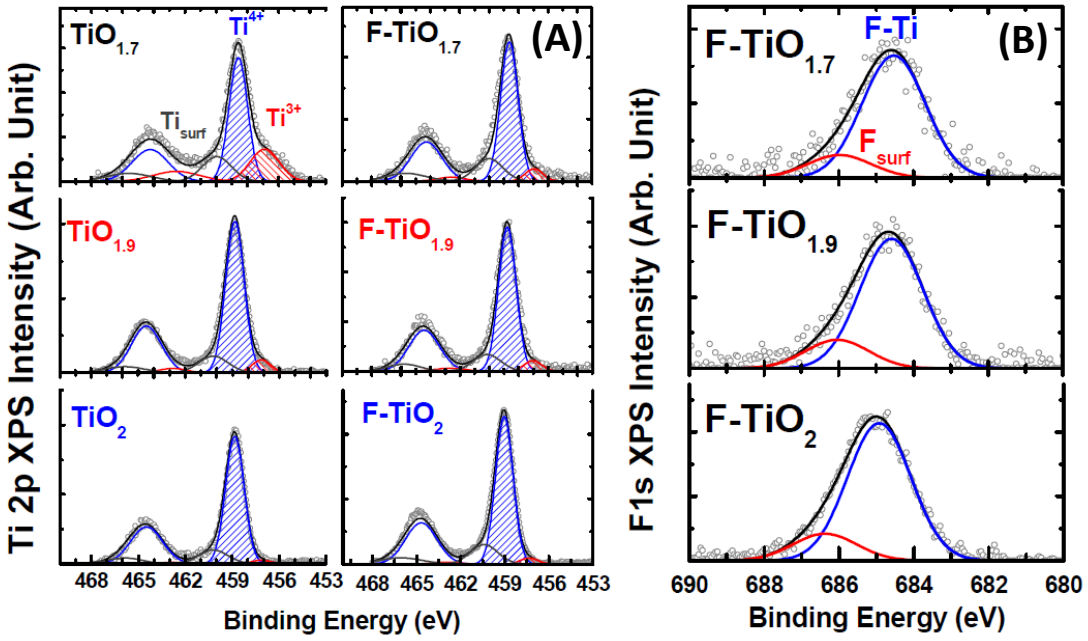

Fig. 1 (A) *Ti 2p and* **(B)** *F 1s XPS spectra of undoped and F-doped $TiO_{1.7}$, $TiO_{1.9}$, TiO_2. Open circles show the raw data, and lines show the results of a Gaussian deconvolution.*

Fig. 2A shows surface conductivity measurements at room temperature for $TiO_{1.7}$ and TiO_2 before and after F insertion. In the case of $TiO_{1.7}$, the high density of suboxide states associated with the O vacancies leads to a metallic conduction (resistivity ~0.1 Ω·cm) but the conductivity decreases slightly with F insertion. This is because F passivation of O vacancies decreases the density of suboxide states used for transport in these materials. However, in the case of TiO_2, F insertion increased conductivity (i.e., decreased resistivity) by a factor of 40. Before discussing these results, it is insightful to note that for O vacancy doped TiO_X, transport occurs in the suboxide band structures induced by O vacancy defects. This is clearly evident in the activation energy of charge transport which is < 0.1 eV for these samples (see Figs. 2B and 3). Polycrystalline TiO_2 will always show activation energy for CB transport of ~ 0.3 eV because of localized electron traps at grain boundaries.[16] We cannot measure the activation

energy for transport in the TiO_2 sample because it is highly insulating. This serves to illustrate that in oxide materials true CB transport is almost impossible to observe because high conductivity in oxides is usually only achievable by reducing the O stoichiometry to create a suboxide band structure. For the F inserted TiO_2 (F-TiO_2) sample we observe a transport activation energy of 0.3 eV consistent with CB transport in polycrystalline TiO_2 (see Fig. 3).

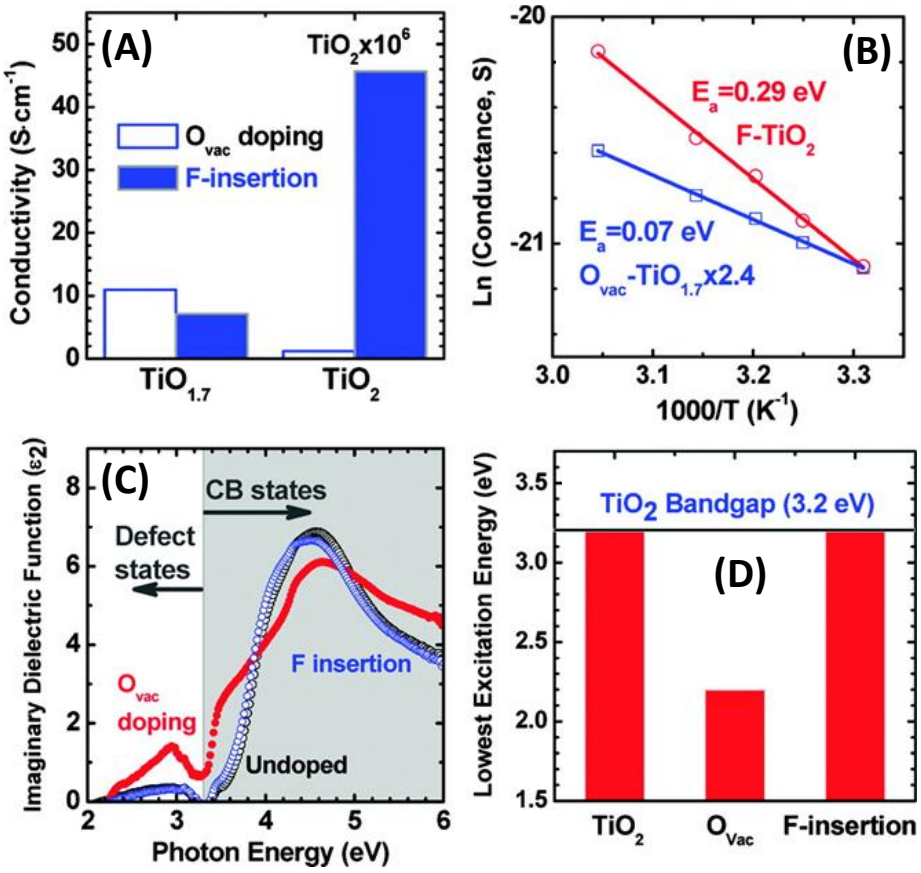

Fig. 2 (A) *Conductivity ($S \cdot cm^{-1}$) measurements at room temperature for 100 nm TiO_X on insulating substrates.* **(B)** *Ln (Conductance, S) as a function of temperature for O vacancy doped $TiO_{1.7}$ and F-inserted TiO_2 diodes. The Ln (S) values of O vacancy doped $TiO_{1.7}$ is normalized to the value of F-inserted TiO_2 at 28.7 °C (i.e. 1000/T = 3.31 K^{-1}). The slope is proportional to the activation energy (E_a) for transport.* **(C)** *Imaginary dielectric functions (ε_2) as a function of photon energy for undoped TiO_2, O vacancy doped $TiO_{1.7}$, and F inserted TiO_2 taken by spectroscopic ellipsometry measurements. CB absorption (shaded in grey) shows an onset at 3.2 eV and is nearly identical for the F inserted and undoped TiO_2 sample. At photon energies below 3.2 eV, absorption is due to O vacancy associated mid-gap states.* **(D)** *Lowest excitation energy of TiO_2, O vacancy doped $TiO_{1.7}$, and F inserted TiO_2 from absorption coefficient spectra. The reference absorption onset for each excitation is ~ 10^5 cm^{-1}.*

It is likely that this conduction is highly localized to the surface of the film. Due to the method for F insertion, we consider that F incorporates in the film primarily in the top 3 ± 1 nm as confirmed in the XPS depth profile. By acting as an n-type donor (to be discussed later) to raise E_F toward CB edge, F represents a positive space charge in the near surface region resulting

in downward band bending toward the surface. If the band bending is such that the CB drops below E_F, then a shallow 2-dimensional electron gas (2DEG) forms. We suggest that the 2DEG is the mechanism for the dramatic increase in conductivity for the F-TiO_2 sample. According to this theory, the surface channel resistivity is much lower than shown in Fig. 2A, where we conservatively consider the entire film thickness (100 nm) in determining the area of the transport channel. If the 2DEG is localized to the top 1 nm of the film as is likely, then true resistivity calculated from the device channel area could easily be two orders lower (~ 10^2 Ω·cm) than that determined by considering the entire film thickness (~10^4 Ω·cm). Note that the F appears to be stable over long periods of time. We have repeated surface conductivity measurements after storing the samples in dry N_2 for 5 months and observe no measurable loss in surface conductivity induced by F. The purpose of storing in dry N_2 is to prevent water adsorption that significantly modifies the surface electronic structure of titanium oxide.

Fig. 2C shows the photon energy dependent imaginary dielectric functions obtained by spectroscopic ellipsometry for undoped titanium oxide (i.e. TiO_2), O vacancy doped titanium oxide (i.e. $TiO_{1.7}$), and titanium oxide after F insertion (i.e F-TiO_2). This allows us to compare the effects of O vacancy doping and F insertion on the CB structure and minimum excitation energy. The CB edge shows an onset at 3.2 eV for TiO_2 and F-TiO_2 samples, indicating that F insertion does not change the bandgap. Absorption at photon energies below 3.2 eV is the result of electron excitation from the valence band (VB) to mid-gap states associated with a suboxide band structure. By looking at the relative absorption coefficients converted from the dielectric functions, it is possible to compare the density of mid-gap states induced by O vacancy doping and by F insertion under the joint density of states theory (see below). The relative absorption of mid-gap states in $TiO_{1.7}$ (~10^5 cm^{-1}) is an order of magnitude higher than that (~10^4 cm^{-1}) of TiO_2. The lowest excitation energy for each film in Fig. 2C is plotted in Fig. 2D. While O vacancy doped $TiO_{1.7}$ shows the significant destabilization of intrinsic TiO_2 band structure with the low excitation energy (from top of VB to empty subgap O vacancy states) at 2.2 eV, F insertion does not induce any of change in CB edge states, stabilizing the bandgap energy at 3.2 eV. As will be discussed later, this stabilized CB edge state of F-TiO_2 is due to the higher excitation energy of molecular orbital states of Ti-F bonds than 3.2 eV bandgap energy of TiO_2.

The conduction band (CB) edge states of titanium oxide thin films were analyzed from the absorption spectra taken by a rotating compensator enhanced spectroscopic ellipsometry (SE). SE determines the complex reflectance ratio, $\rho=r_p/r_s$, where r_p and r_s are the complex reflectance of waves in the polarized light that are parallel (p) and perpendicular (s) to the plane of incidence, respectively. Monochromatic light from a xenon lamp provides visible and ultraviolet light having an energy range from 1.5 eV (8267 Å) to 6 eV (2066 Å). This light excites electrons from the top of the valence band to the conduction band in the overlayer (i.e. titanium oxide) material. From ρ, optical properties such as index of reflection (n), extinction coefficient (k), and dielectric function (ε) are determined. To extract the dielectric function of the titanium oxide overlayer from the pseudodielectric function of the whole stack (air/TiO_2/Si) a three phase model was applied such that the dielectric function of Si was analyzed first, and the dielectric functions of the titanium oxide overlayer was subsequently extracted. The generalized equation for the optical three phase model is expressed as follows:

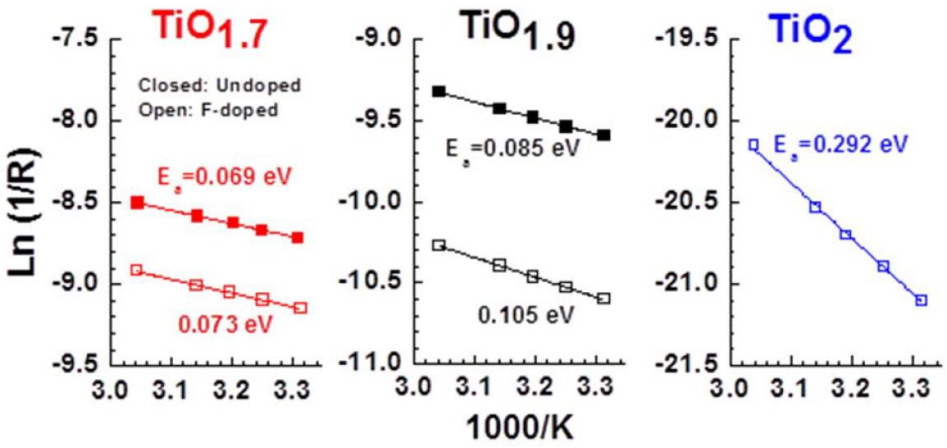

Fig. 3 *Arrhenius Plot of Ln(1/resistance, Ω^{-1}) against 1000/temperature (K) for undoped and F-doped $TiO_{1.7}$, $TiO_{1.9}$, TiO_2. Squares show raw data, and lines show linear fits. The slope of the fit is proportional to the activation energy for thermally activated charge transport.*

$$<\varepsilon>=\varepsilon_s+\frac{4\pi d n_a}{\lambda}\frac{\varepsilon_s(\varepsilon_s-\varepsilon_o)(\varepsilon_o-\varepsilon_a)}{\varepsilon_o(\varepsilon_s-\varepsilon_a)}\left(\frac{\varepsilon_s}{\varepsilon_a}-\sin^2\phi\right)^{1/2} \qquad \text{Eq. 1}$$

where $<\varepsilon>$ is the measured pseudo dielectric function, ε_s is the substrate (Si) dielectric function, ε_a is the air dielectric function, ε_o is the overlayer (titanium oxide) dielectric function, d is the overlayer thickness, n_a is the index of reflectance for air, λ is the wavelength of incident polarized light, and φ is the angle of incidence (fixed at 67.08°). Because all parameters except ε_o are already known, ε_o can be obtained by iterative calculation using Eq. 1

The absorption coefficient, α is obtained from the λ and k values by the conversion equation:

$$\alpha=4\pi k/\lambda \qquad \text{Eq. 2}$$

where k is the extinction coefficient and λ is the wave length of light. Fig. 4 shows the resulting graphs of the extinction coefficients for the different oxide films.

Fig. 5A shows current-voltage (IV) curves for diodes consisting of TiO_x on highly doped p-Si. We present results for TiO_2 and $TiO_{1.7}$ before and after F insertion. Without F insertion, both TiO_2 and $TiO_{1.7}$ heterojunction devices show almost symmetrical IV curves where the reverse bias leakage current is nearly as high as the forward bias current. This is the result of two factors. First, the high density of subgap states in $TiO_{1.7}$ provide a path for carrier transport in the reverse bias direction. Second, the low n-type character (i.e., low E_F level) of O vacancy doped TiO_X closely aligns with E_F in p-Si resulting in minimal interface band bending. For TiO_2 and $TiO_{1.7}$, the reverse bias current decreases and the forward bias current increases with F insertion. This is the combined effect of defect state passivation by F and increased E_F in the F-TiO_X layer to achieve greater band bending at the p-Si interface. In Fig. 5B, the rectifying factor (taken as the ratio of forward to reverse bias current) increases with F insertion by a factor of 3

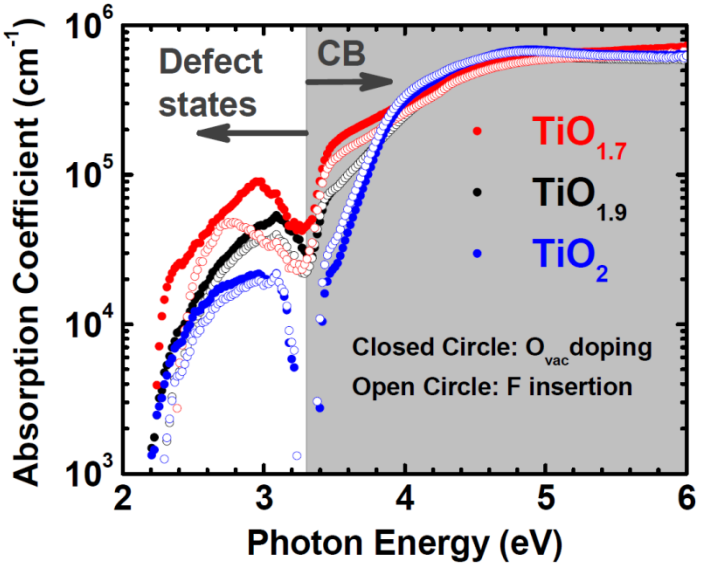

Fig. 4 *Absorption coefficient spectra for undoped and F-doped $TiO_{1.7}$, $TiO_{1.9}$, TiO_2 taken by SE measurement and three-phase analysis. Closed circles show undoped TiO_X, and open circles show F doped TiO_X.*

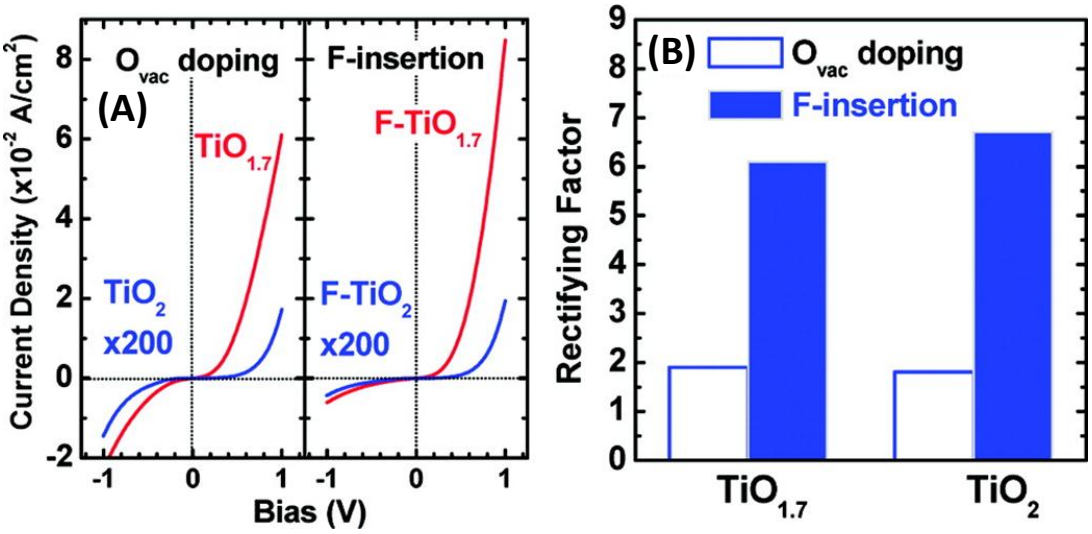

Fig. 5 (A) *Current-voltage (IV) curves for ~ 10 nm TiO_X on highly doped (0.01 Ω cm) p-Si. Red lines show $TiO_{1.7}$ samples, and blue lines show TiO_2. The current density values of all TiO_2 diodes were multiplied by a factor of 200.* **(B)** *Rectifying factor for TiO_2 and $TiO_{1.7}$ before and after F doping. Rectifying factors are the ratio of forward to reverse bias current. For O vacancy doped TiO_X, low rectifying factors are the result of a high concentration of defect states and low Fermi level (E_F). By passivating defects and raising E_F, F doping increases the rectifying factor for each precondition by more than a factor of 3.*

for both cases. A similar trend was observed for $TiO_{1.9}$ (not shown), except that the rectifying factor before F insertion was 3.4 and increased to 22.4 after F insertion. This is much higher

than for TiO_2 and $TiO_{1.7}$. We do not fully understand this anomaly but believe it is in part a result of the higher EF in $TiO_{1.9}$ before F insertion compared to either TiO_2 or $TiO_{1.7}$ as discussed below. It may seem counterintuitive that surface F doping could affect rectification at the buried Si-TiO_X interface. However, the thickness of the TiO_X layer (i.e. 10 nm) is much smaller than the depletion width. Consequently, n-type doping to the surface will still effect rectification due to the mean field across the depletion region of this p-n heterojunction.

Fig. 6A shows E_F for TiO_2, $TiO_{1.9}$, and $TiO_{1.7}$ before and after F insertion. We determined E_F by fitting the valence band edge XPS spectra (see Fig. 7). It is insightful to first consider the effect of O vacancies on the Femi level before considering the effect of F doping. In the case of stoichiometric TiO_2, we measured E_F to be 2.4 eV. Doping by O vacancies initially introduces partially occupied Ti^{3+} states about 0.3~0.5 eV below the CB edge,[17] and these states serve to pin E_F at approximately 2.8 eV in the $TiO_{1.9}$ sample. However, if the oxide is further reduced, semi-metal states form that pin E_F at a much lower energy. This is evident in the $TiO_{1.7}$ sample that shows E_F to be 2.1 eV. We note that this value is in excellent agreement with the spectroscopic ellipsometry spectra that showed a minimum excitation at 2.2 eV (see Fig. 2D). Although this reduced oxide is highly conductive, transport occurs in the metallic band structure of the suboxide, and it is not possible to use this material as a semiconductor because of the high density of mid-gap states.

Fig. 6A also shows that F insertion raises E_F for each pre-condition by up to 1 eV. In the case of $TiO_{1.7}$, where E_F is initially pinned at 2.1 eV by the semi-metal states of the suboxide, F insertion increases E_F to 3.1 eV, just below the CB edge. This is partly the result of F passivation of suboxides states in the bandgap. However, the resulting E_F is 0.7 eV greater than undoped, stoichiometric TiO_2. We conclude that in addition to passivating defects, F acts as an n-type donor. These results demonstrate the ability of F insertion to tune E_F outside the limits of O vacancy doping. Comparing E_F after F insertion for each pre-condition shows that E_F scales with the atomic ratio of F to Ti determined by XPS (see Fig. 6B). This indicates that F binding to an O vacancy gives rise to a free CB electron in titanium oxide. We call this effect n-type doping by F insertion. Fig. 6B also indicates another binding state of F which we assign as interstitial insertion. Theoretical calculations discussed below explain the origin of these two binding states and discuss their respective contributions to modifying the bulk electronic properties. We note that E_F scales with the concentration of a F binding state at 684.9 eV that we assign as O substitution (or binding to a preexisting O vacancy).

Fig. 6C shows the Ti 2p spectrum for O vacancy doped and F inserted $TiO_{1.7}$. The peak binding state at 458.5 eV is characteristic of the Ti^{4+} states in the stoichiometric oxide, while the shoulder at lower binding energy (BE, 456.9 eV) represents Ti^{3+} and Ti^{2+} states in the suboxides. Comparison of the Ti 2p spectra of $TiO_{1.7}$ before and after F insertion shows a decrease in Ti^{3+} states from 41% to 9%. This is a dramatic reduction in the density of defect states with F insertion, and is direct evidence that F passivates O vacancies by binding Ti^{3+}. Fig. 6D shows the absorption ratio of mid-gap to CB states before and after F insertion for each TiO_X pre-condition based on spectroscopic ellipsometry measurements. This provides additional evidence that F binding is primarily to O vacancies, and that F passivates defect states in non-stoichiometric oxides. Because the chemical instability of O vacancies is one of the primary

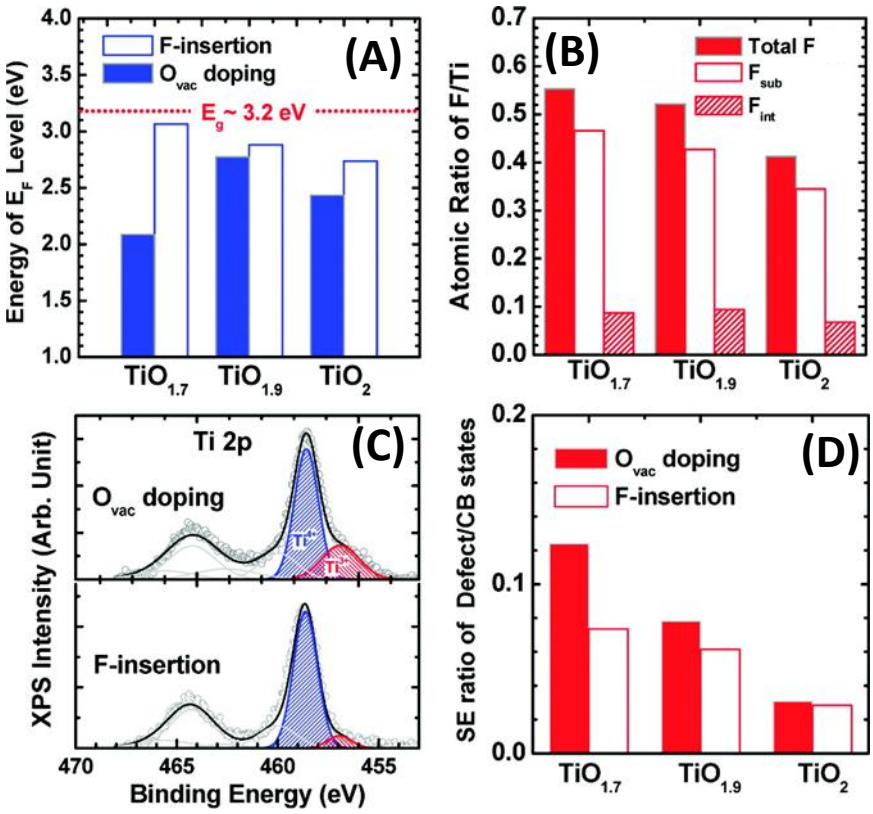

Fig. 6 (A) *Fermi level (E_F) before and after F insertion for each TiO_X precondition determined by fits to the valance band edge XPS spectra (see Fig. 8).* **(B)** *The atomic ratio of F to Ti after 3 min. plasma treatment for each TiO_X precondition. Atomic ratios are shown for two different binding states identified by XPS (see Fig. 8B) and for total F. We assign these two binding states as F substituted for O and as interstitial F. Substitutional F concentration depends strongly on the initial O vacancy concentration before plasma treatment and appears to determine E_F after F insertion.* **(C)** *Ti 2p XPS spectrum of $TiO_{1.7}$ before and after F insertion. Open circles show the raw data, and lines show the results of a Gaussian deconvolution. The peak state at 458.5 eV is the Ti^{4+} state in stoichiometric TiO_2. The lower binding energy peak at 456.9 eV is the Ti^{3+} state and is a marker for O vacancy induced defect states. The decrease in Ti^{3+} state concentration with F insertion indicates that F passivates defects by binding to Ti^{3+} at O vacancies.* **(D)** *Ratio of defect state to CB absorption measured by spectroscopic ellipsometry before and after F insertion for $TiO_{1.7}$, $TiO_{1.9}$, and TiO_2. Defect state/CB absorption was taken as the maximum absorption coefficient below/above 3.2 eV. The trend shows that F passivates O vacancies that give rise to defect states.*

factors that limit TMO device reliability, we believe that F insertion may greatly improve the chemical stability of TMO semiconductor devices. However, we have not yet investigated the effect of F insertion on chemical stability. Note that in the case of stoichiometric TiO_2, F insertion does not significantly change the O vacancy concentration because it is already so low.

We note that SF_6 can etch TiO_2 by formation of TiF_4 which has a vapor pressure at room temperature. Fracassi et al. showed that during SF_6 plasma etching a layer of TiF_3 and TiF_4 forms on the surface of the oxide.[18] TiF_4 leaves the surface by sublimation which is likely

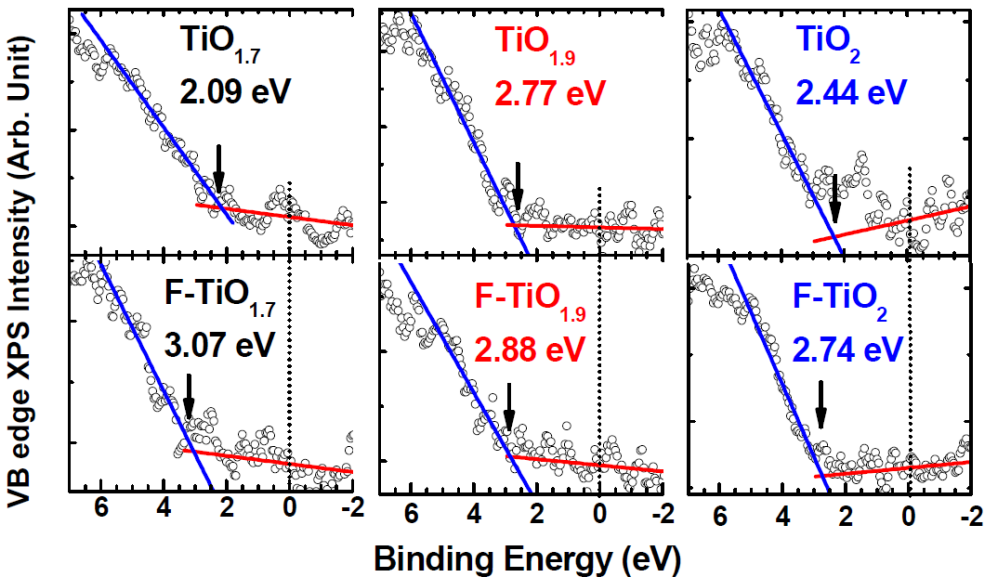

Fig. 7 *VB edge XPS spectra for undoped and F-doped $TiO_{1.7}$, $TiO_{1.9}$, TiO_2. Open circles show raw data, and lines show fitting used to determine Fermi level.*

assisted by ion sputtering in the plasma. Consequently, the formation of titanium fluorides(TiF_X) and subsequent etching represents an upper limit to F doping in TiO_2. For our plasma exposures, the F concentration stayed beneath the limit for formation of TiF_4 as can be seen by atomic fractions of F to Ti below 0.6. Fracassi et al. also showed that formation of TiF_3 and TiF_4 during etching is easily visible in the Ti 2p XPS spectrum by a 3–5 eV shift to higher BE.[19] We observe no significant shift (< 0.2 eV) in the Ti 2p BE with plasma treatment. This suggests true chemical doping by F insertion rather than formation of a fluoride phase.

Theoretical calculations are carried out using a high level, many-electron theory in order to investigate fundamental properties of TiO_2. This is a well-established method for investigating the electronic structure of metal oxides.[20] The theoretical model considers three different modifications to TiO_2: a) interstitial F, b) F substitution for oxygen or c) an O vacancy. Of particular interest are effects on the electronic excitation spectrum and induced spin states that accompany changes in the occupancy of Ti d orbitals. We use a geometry optimized $Ti_{18}O_{36}$ nanoparticle to investigate these effects. While the nanoparticle differs in detail from bulk TiO_2, the interior sites involve the same basic electronic structure. Fig. 8A depicts $Ti_{18}O_{36}$ nanoparticle model with an interstitial F site. In other calculations, a subsurface vacancy is created by removing a neutral O atom at the interior of the particle, and a F atom is substituted for O.

In all three systems, the lowest energy excitation is best described as exciton, with a hole that is largely localized on a single O2p and an electron that is transferred to the d-shell of a nearest neighbor Ti. In the nanoparticle, the oxygen vacancy and interstitial F alter the excitation energy or "bandgap" from the ~3eV of the unmodified $Ti_{18}O_{36}$. Substitutional F increases the excitation energy while an O vacancy decreases the excitation energy (see Table 1). This explains why F insertion does not alter the minimum excitation energy observed experimentally.

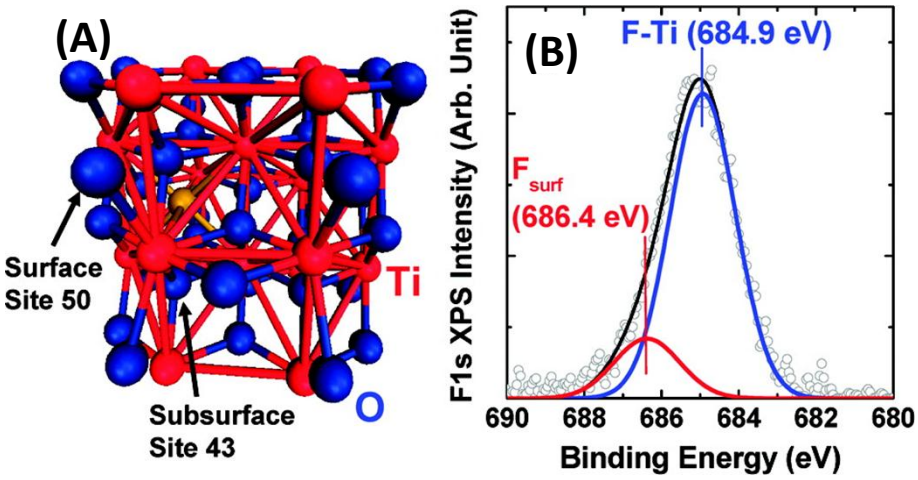

Fig. 8 (A) *$Ti_{18}O_{36}$ nanoparticle model with interstitial F (yellow ball) used for theoretical calculation. In this site, F sits in a distorted octahedral formed by six Ti atoms. In this case charge transfer to the F ion is primarily from a surface O atom (shown as site 50) because the nearest neighbor Ti atoms are already fully oxidized. The substitutional F site and O vacancy site (shown as site 43) have three Ti nearest neighbors.* **(B)** *F 1s XPS spectrum of TiO_2 after 3 min. F insertion. Open circles show the raw data, and lines show the results of a Gaussian deconvolution. The peak state at 684.9 eV indicates Ti-F bonding as a result of O subsitution. We assign the state at 686.5 eV as interstitial F. The relative energies of the two binding states are explained by the qualitatively different charge exchange between F and either Ti or O depending on the insertion site.*

Although F insertion creates new states in the bandgap, the lowest excitation energy is still the difference between the unmodified valance and conduction band edges of stoichiometric TiO_2.

The calculations also reveal major differences in the concentration of free carrriers: an O vacancy and substitutional F induce unpaired electron spin in the d-shell of a nearest neighbor Ti, while interstitial F induces unpaired spin on nearby oxygen. One of the key findings that relates to the present investigation is the difference in behavior of subsurface species in the creation of surface electronic states involving oxygen atoms that are substantially undercoordinated, e.g., 2-fold coordinated, on the surface of TiO_2. O atoms on the surface can serve as receptors of unpaired spins generated internally and are strongly affected by nearby subsurface modifications. To summarize, substitutional F is responsible for the increase of electron density in CB of TiO_2 in contrast to the increase in mid-gap states by O vacancy doping. Furthermore, interstitial F leads to an unpaired spin in the O2p orbital of surface O that draws free carriers to the surface and acts as a surface conduction.

To emphasize the high level of correlation between the experimental results and the theoretical study, we briefly discuss the nature of F binding states in TiO_2 as identified by XPS spectra. Fig. 8B shows the F 1s XPS spectrum for TiO_2 after F insertion. The peak is composed of two binding states centered at 684.9 and 686.4 eV. This spectrum is identical to previous reports for F insertion of TiO_2 by solution phase methods.[19] The peak state at 684.9 eV indicates Ti-F bonds by substitutional F doping. The shoulder at higher BE is a F surface state, and previous reports have hypothesized as to its exact origin.[19] We propose that the higher BE state

Table 1

	O Vacancy	Substitutional F	Interstitial F
Increase in number of Ti 3d electrons*	1.58	0.89	0.00
Increase in number of unpaired O 2p electrons*	0.00	0.00	0.93
F population	—	9.55	9.62
Change in O2p-Ti3d excitation energy (eV)*	−0.3	+0.8	+0.2

represents interstitial F insertion (i.e. F insertion without removal of an O atom). In the case of O substitution, F coordinates to a partially oxidized Ti atom, electron density is transferred from the Ti to the F, and the Ti atom assumes a 4+ oxidation state. However, if F is inserted or bound to the surface without the removal of O, F could not draw electron density from a Ti nearest neighbor because all nearest neighbor Ti atoms are fully oxidized. In this case, the calculation suggests that F attracts electron density from a nearby O atom creating a partially unoccupied O2p state. This is what we term interstitial insertion. The relative energies of the two binding states are explained by the qualitatively different charge exchange between F and either Ti or O depending on the insertion site.

In Fig. 1B, two F binding states are resolved at 684.9 eV and 686.4 eV. Based on Ti 2p XPS data in Fig. 1A, Ti^{3+} species is reduced by F passivation forming Ti-F bonds. At this bond, F attracts about one electron from the neighboring Ti because the electronegativity of F is higher than Ti. This F-induced charge exchange causes the shift of binding energy of Ti higher than Ti^{3+} and that of F lower than neutral F. This Ti-F formation is equivalent to the substitutional F doping either replacing the lattice oxygen (O) site or passivating O-vacancy sites. The theoretical calculation (to be discussed later) predicts the origin of this kind of Ti-F bond as the substitutional F-doping by replacing (i) the top-surface O site having two near-neighboring Ti atoms and (ii) the sub-surface O or O-vacancy site having three near-neighboring O sites with F. For all cases, F attracts electron from Ti, causing the singly occupied 3d electron in Ti. Thus, the F 1s biding state at 684.9 eV is assigned as the substitutional F doping to Ti. On the other hand, the F 1s bonding state at 686.4 eV is assigned as the surface F ($F_{surface}$) because it has a higher concentration at the more surface region. The theoretical calculation considers the interstitial F at subsurface. The interstitial F occupies the octahedral sites formed by Ti ions. F attracts electron density because of its electronegativity but since Ti is already depleted by its normal bonding with O, the electron attracted to F comes from O2p electron density of top-surface undercoordinated O, which leads to the unpaired electron in O2p orbital. However, the electronegativity of O is far higher than Ti, the electron density that F attracted from O is a partial electron density smaller than that for Ti-F case. This partial charge exchange causes the higher binding energy of interstitial F than that of substitutional F. Therefore, the density of surface-segregated $F_{surface}$ binding state in XPS data and theoretical result strongly suggest that F 1s bonding state at 686.4 eV is due to the interstitial F.

Considering the two binding states to be equivalent to substiutional and interstitial F insertion considered by the theoretical calculations, we find excellent agreement between the theoretical conclusions and the experimental findings. First, we observe that substitutional F (i.e. binding state at 684.9 eV) scales with the O vacancy concentration before doping while interstitial F (i.e. binding state at 686.4 eV) shows little dependence on the precondition to plasma treatment. Second, we find that E_F scales closely with the concentration of substitutional F which theory predicts to generate a free electron in the Ti d shell, unlike interstitial F. Finally, the role of interstitial F to increase surface conductivity by drawing free charge carriers to the surface can explain the enhancement of surface conductivity in stoichiometric TiO_2 after F insertion.

5.5 Conclusion

This study demonstrates that F passivates O vacancy defects and acts as an extrinsic n-type donor for titanium oxide, resulting in greatly enhanced CB transport. This effect is stable at ambient temperature with no measureable loss of surface conductivity over several months. It is likely that F will have the same effect on other TMO semiconductors. The ability to remove mid-gap states and tune E_F while stabilizing the intrinsic TiO_2 band structure can result in a highly conductivity oxide suitable for device architecture and overcomes the limitations of current O vacancy doping technology for oxide semiconductors. The highly conductive surface electronic structure of n-type titanium oxide with F insertion, free of E_F level pining, is promising for many metal-oxide applications including solar cells, resistive switching memory, transparent oxide transistors, sensors, and catalysts.

5.6 References

(1) Wager, J. F. *Science* 2003, *300*, 1245.
(2) Xie, X.; Li, Y.; Liu, Z.-Q.; Haruta, M.; Shen, W. *Nature* 2009, *458*, 746.
(3) Park, J. Y.; Lee, H.; Renzas, J. R.; Zhang, Y.; Somorjai, G. A. *Nano Lett.* 2008, *8*, 2388.
(4) Fujishima, A.; Honda, K. *Nature* 1972, *238*, 37.
(5) Bach, U.; Lupo, D.; Comte, P.; Moser, J. E.; Weissortel, F.; Salbeck, J.; Spreitzer, H.; Gratzel, M. *Nature* 1998, *395*, 583.
(6) Kwon, D.-H.; Kim, K. M.; Jang, J. H.; Jeon, J. M.; Lee, M. H.; Kim, G. H.; Li, X.-S.; Park, G.-S.; Lee, B.; Han, S.; Kim, M.; Hwang, C. S. *Nat Nano* 2010, *5*, 148.
(7) Peng, X.; Chen, A. *J. Mater. Chem.* 2004, *14*, 2542.
(8) Di Valentin, C.; Pacchioni, G.; Selloni, A. *J. Phys. Chem. C* 2009, *113*, 20543.
(9) Zhang, Y.; Kolmakov, A.; Chretien, S.; Metiu, H.; Moskovits, M. *Nano Lett.* 2004, *4*, 403.
(10) Frederikse, H. P. R. *Journal of Applied Physics* 1961, *32*, 2211.
(11) Cao, F.; Oskam, G.; Searson, P. C.; Stipkala, J. M.; Heimer, T. A.; Farzad, F.; Meyer, G. J. *J. Phys. Chem.* 1995, *99*, 11974.
(12) Asahi, R.; Morikawa, T.; Ohwaki, T.; Aoki, K.; Taga, Y. *Science* 2001, *293*, 269 -271.
(13) Chen, X.; Burda, C. *J. Am. Chem. Soc.* 2008, *130*, 5018.
(14) Choi, W.; Termin, A.; Hoffmann, M. R. *J. Phys. Chem.* 1994, *98*, 13669.
(15) Janisch, R.; Gopal, P.; Spaldin, N. A. *Journal of Physics: Condensed Matter* 2005, *17*, R657.

(16) Cox, P. A. *Transition Metal Oxides: An Introduction to Their Electronic Structure and Properties*; Oxford University Press, 2010.
(17) Lucovsky, G.; Seo, H.; Lee, S.; Fleming, L. B.; Ulrich, M. D.; Lüning, J.; Lysaght, P.; Bersuker, G. *Japanese Journal of Applied Physics* 2007, *46*, 1899.
(18) Fracassi, F.; d' Agostino, R. *Pure and Applied Chemistry* 1992, *64*, 703.
(19) Czoska, A. M.; Livraghi, S.; Chiesa, M.; Giamello, E.; Agnoli, S.; Granozzi, G.; Finazzi, E.; Valentin, C. D.; Pacchioni, G. *J. Phys. Chem. C* 2008, *112*, 8951.
(20) Lucovsky, G.; Whitten, J. L. *Surface Science* 2007, *601*, 4138.

Chapter 6

Highly n-Type Titanium Oxide as an Electronically Active Support for Platinum in the Catalytic Oxidation of Carbon Monoxide

6.1 Abstract

The role of the oxide-metal interface in determining the activity and selectivity of chemical reactions catalyzed by metal particles on an oxide support is an important topic in science and industry. A proposed mechanism for this strong metal-support interaction is electronic activation of surface adsorbates by charge carriers. Motivated by the goal of using electronic activation to drive non-thermal chemistry, we investigated the ability of the oxide support to mediate charge transfer. We report an approximately twofold increase in the turnover rate of catalytic carbon monoxide oxidation on platinum nanoparticles supported on stoichiometric titanium dioxide (TiO_2) when the TiO_2 is made highly n-type by fluorine (F) doping. However, for non-stoichiometric titanium oxide ($TiO_{X<2}$) the effect of F on the turnover rate is negligible. Studies of the titanium oxide electronic structure show that the energy of free electrons in the oxide determines the rate of reaction. These results suggest that highly n-type TiO_2 electronically activates adsorbed oxygen (O) by electron spillover to form an active O^- intermediate.

6.2 Introduction

Although metals alone are often catalytically active, most industrial catalysts consist of metal particles supported on a porous oxide. This not only provides a high surface area for the heterogeneous catalyst, but as shown by many studies, the oxide support plays an important role in determining the activity and selectivity of the catalyst.[1-4] This phenomenon, known as the strong metal-support interaction (SMSI), has been widely studied and is an important topic in both science and industry.[5]

SMSI affects a wide range of catalytic reactions, including carbon monoxide (CO) and carbon dioxide (CO_2) hydrogenation[4-6], selective hydrogenation[7-9], and CO oxidation[10-13]. Although not traditionally termed SMSI, the catalyst support also plays an important role in activating molecular oxygen for selective partial oxidation reactions. Industrially relevant examples include the synthesis of aldehydes from primary alcohols[14], the production of hydrogen peroxide from hydrogen[15-19], and the conversion of methane to synthesis gas[20-22]. In all of these cases, molecular oxygen is preferred over other oxygen donors due to cost, energy efficiency, and environmental concerns.[14,22]

Titanium oxide is perhaps the best known example of an SMSI support.[2,4] Additionally, titanium oxide is a common support for catalysts demonstrating high selectivity toward partial oxidation.[14,18,22] The majority of proposed mechanisms for the role of titanium oxide fall into

one of the following categories: 1) formation of active sites when the support wets (or "decorates") the metal particle[23,24], 2) oxygen (O) activation and/or spillover from chemically active defects in the support[25], and 3) electronic mediation through various forms of charge transfer[12,26]. Although each of these mechanisms can play an important role, this study focuses on the role of charge transfer and electronic mediation due to its importance in energy conversion reactions.

Previous studies have indicated that, at least in certain instances, catalytic oxidation reactions proceed by an electronically activated pathway.[27-32] Bonn *et al.*[27] showed that for CO oxidation on Ru, the activation of chemisorbed O occurs by charge transfer from the metal. Because the active O species cannot form thermally until well above the desorption temperature of CO, a temperature ramp of a CO/O_2 co-adsorbed Ru surface produces CO and O_2, but not CO_2. However, a femtosecond laser pulse can produce very high electronic temperatures on the short time scale without significant lattice heating. This serves to activate the O without CO desorption, resulting in CO_2 formation.

Although fundamentally insightful, this type of experiment employing a femtosecond laser cannot be scaled for high turnover applications. Another approach to achieve electronic activation is to use an electronically modified catalyst. Several variables can tune the electronic structure of a catalyst including size[31], support[32], and doping[30]. The objective of this study was to identify the role of the support in electronic activation of surface chemistry. Here we demonstrate the ability to modify the electron transport properties of titanium oxide by controlling the O stoichiometry and by fluorine (F) doping. We find that stoichiometric titanium dioxide (TiO_2) modified by F doping is an electronically active support for CO oxidation on platinum (Pt) under conditions of high pressure and temperature (760 Torr and 443 K). However, the highly conductive reduced oxide shows little or no electronic activity toward CO oxidation, with or without F.

We have previously reported the production of hot electron flow during catalytic CO oxidation using the Pt/TiO_2 nanodiode system.[33] In that work we demonstrated that there is an electron flow from the Pt to the TiO_2 in proportion to the catalytic turnover. We now find that the opposite effect occurs by F doping TiO_2. In this case, an electron flow from the titanium oxide to the surface adsorbates significantly increases the catalytic reaction rate by activating surface O for reaction with CO.

6.3 Experimental

6.3.1 Catalyst Preparation

Thin films of titanium oxide with variable oxygen (O) vacancy concentrations served as supports for the platinum (Pt) catalyst. First, titanium oxide films (100 nm) were deposited on Si(100) wafers with a 500-nm-thick thermal oxide by direct-current magnetron sputtering. Sputtering conditions were 400 W plasma power, 450 V bias voltage, 50 sccm Ar flow, and 3 sccm O_2 flow. As deposited, the titanium oxide films were highly O deficient. Rapid thermal annealing in O_2 at temperatures between 623 and 773 K was used to vary the O concentration in the films. To avoid grain size variations due to annealing at different temperatures, all samples were annealed in nitrogen (N_2) at 773 K. Titanium oxide films with three stoichiometries were

prepared: TiO_2, $TiO_{1.9}$, and $TiO_{1.7}$, as determined from the ratio of Ti^{3+} and Ti^{4+} in the Ti 2p X-ray photoelectron spectra (XPS) shown in Chapter 5 Fig. 1A.

Fluorine (F) insertion was achieved by plasma treatment in N_2 gas with trace sulfur hexafluoride (SF_6). Trace SF_6 was introduced into the chamber by flowing a 9:1 mixture of SF_6 and O_2 followed by pumping to chamber base pressure (5 mTorr). After pumping, a small background pressure of SF_6 remained in the chamber. N_2 gas was then introduced at 80 sccm for plasma treatment. Plasma power was 20 W and DC substrate bias was 130 V. F concentration was tunable with the length of the plasma treatment. Two samples of each TiO_X stoichiometry were fabricated, and one of each type was plasma treated. This produced six supports for subsequent Pt deposition: TiO_2, $TiO_{1.9}$, and $TiO_{1.7}$, each with and without F. Fig. 1B in Chapter 5 shows the F 1s XPS spectra for each of the F-doped supports. All samples were stored under a dry N_2 atmosphere until the reaction rate measurements.

Pt nanoparticles were deposited onto the samples by electron beam evaporation. Vapor deposited, rather than colloidally synthesized, nanoparticles were used to avoid the presence of an insulating polymer capping layer between the metal nanoparticles and the support. For electron beam evaporation the chamber base pressure was less than 10^{-5} Torr, and the deposition rate was 0.02 Å/s. The average film thickness monitored by quartz crystal microbalance was 1 nm. SEM showed that at this average thickness the Pt nanoparticles left ~50% of the support exposed as shown in Figure S2 (supporting information).

6.3.2 Catalyst Characterization

The electronic structure of the titanium oxide supports was characterized by XPS, spectroscopic ellipsometry, and measurements of surface conductivity and activation energy for charge transport.

XPS was used to analyze the chemical binding states of the titanium oxide films and the supported Pt catalysts both before and after reaction (Physical Electronics, PHI 5400 ESCA/XPS system with an Al anode source at 1486.6 eV). The analyzer was positioned at 50° relative to sample normal. All binding energies were calibrated to the Ti 2p peak state.

The real and imaginary parts of the complex dielectric constant, $\varepsilon c = \varepsilon_1 + i\varepsilon_2$, and absorption coefficients for titanium oxide samples were determined by visible-ultra violet spectroscopic ellipsometry in a rotating compensator enhanced spectrometer. The monochromatic light source from a Xenon lamp at photon energies of 1.5–6 eV was used with spectral resolution of 15 meV.

To measure surface conductivity of the titanium oxide films, ohmic contact was made to the titanium oxide using thin film electrodes consisting of 10 nm Ti and 100 nm Au. All metals were deposited by electron beam evaporation. Measurements were made with a Keithley 2400 sourcemeter.

6.3.3 Reaction Rate Measurements

A batch mode reactor with a boron nitride substrate heater was used to determine the reaction rates of CO oxidation on each of the above described catalysts. A metal bellows

circulation pump provided gas mixing. Gas pressures were 40 Torr CO and 100 Torr O_2 in a background of He. The catalyst temperature was 443 K. Each catalyst was tested for 112 min and CO_2 production was monitored as a function of time using a gas chromatograph with a thermal conductivity detector.

Reaction rates are reported in turnover frequency (TOF) as CO_2 molecules produced per Pt site per minute. All error bars represent the 95% confidence interval based on the rate of CO_2 production normalized to the estimated number of Pt sites. The number of Pt sites was estimated by assuming a uniform (111) surface structure over the entire catalyst area. Although this calculation is approximate, it provides a consistent normalization to the catalyst area and yields a reasonable estimate of the absolute TOF.

6.4 Results and Discussion

Fig. 1 shows the effect of F on the reaction rate and on the surface conductivity of each stoichiometry. In the case of stoichiometric TiO_2, F doping increased the reaction rate by 61%, while F doping to $TiO_{1.7}$ and $TiO_{1.9}$ decreased the reaction rate by 21 and 8%, respectively. There is a surprising similarity between the effect of F on the turnover rate, and the effect of F on the surface conductivity of the titanium oxide support. As in the turnover rate measurements, F doping to TiO_2 dramatically increased (40-fold) the surface conductivity, while F doping to $TiO_{1.7}$ and to $TiO_{1.9}$ resulted in only a slight decrease (approximately twofold) in surface conduction. We can explain these results by considering the electronic structure of stoichiometric and reduced titanium oxide. We characterized the electronic structure using two measurements: the activation energy of surface conduction and the optical absorption spectrum.

To understand how the activation energy of transport relates to the electronic structure, it is necessary to consider the role of grain boundary defects in polycrystalline TiO_2. Grain boundaries produce defects in the band structure of titanium oxide with a localized defect state ~0.3 eV below the conduction band edge. Consequently, this is the activation energy for conduction in polycrystalline TiO_2 because electrons thermally trap and de-trap at grain boundaries during transport. In contrast, O vacancies at high concentrations form a sub-oxide band structure at a reduced energy. This sub-oxide band shows semi-metal, or nearly unactivated, electron transport.[34]

Fig. 2A shows the activation energies for electron transport in $TiO_{1.7}$ and TiO_2. As expected, the highly reduced oxide shows low activation energy for conduction (0.07 eV) consistent with semi-metal transport in a low energy sub-band, while F-doped TiO_2 shows activation energy of 0.29 eV, consistent with conduction band transport across grain boundaries. TiO_2 without F was too insulating to accurately measure the activation energy of transport. However, F insertion to $TiO_{1.7}$ did not change the transport mechanism.

Fig. 2B compares the optical absorption of $TiO_{1.7}$ and TiO_2. To illustrate the differences between these samples, we show the minimum excitation energy having a fixed absorption coefficient of 2×10^4 cm^{-1}. Full spectra are shown in Fig. 4 of Chapter 5. We find that $TiO_{1.7}$ has a strong absorption located ~0.7 eV below the conduction band edge that arises from excitation of electron-hole pairs in the sub-oxide band. This measurement reflects the decrease

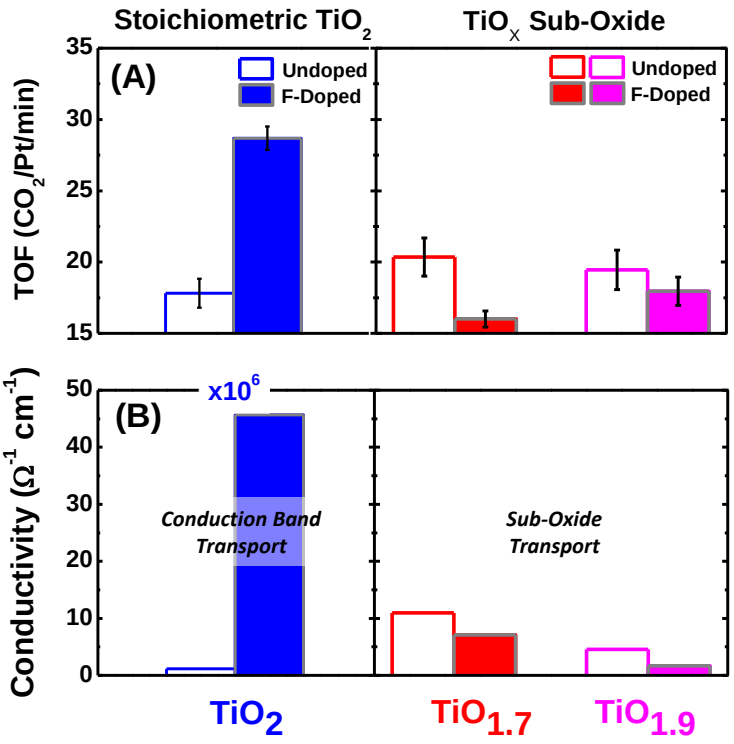

Fig. 1 (A) *Turnover frequencies (TOF) for CO oxidation on Pt nanoparticles supported on the six titanium oxide supports: TiO_2, $TiO_{1.9}$, and $TiO_{1.7}$, each with and without F insertion. Reaction occurred in 40 Torr CO, 100 Torr O_2, and 620 Torr He at 443 K. TOF data reflect the stable rate after ~30 min of deactivation. Error bars represent 95% confidence intervals.* **(B)** *Surface conductivity measurements for all six titanium oxide supports before Pt nanoparticle deposition. Comparison of* **(A)** *and* **(B)** *shows a surprising similarity between the effect of F on the TOF and on the surface conductivity.*

in bandgap energy for the reduced oxide and shows the difference in the energy of free electrons in the two supports.

Fig. 3A is a diagram of the two band structures of stoichiometric and reduced titanium oxide based on the above measurements. In the cases of both $TiO_{1.7}$ and $TiO_{1.9}$, F doping decreased the surface conductivity. The reason for this is that F binds to Ti at the sites of O vacancies resulting in passivation of defect states. Conduction in these samples occurs primarily in the sub-oxide band structure induced by the high concentration of O vacancies. Consequently, a decrease in the O vacancy concentration partially removes the conduction channel in these two samples. However, F insertion in the TiO_2 sample increased conductivity by a factor of 40. This is because F acts as an extrinsic n-type donor in metal oxide semiconductors, increasing the concentration of free electrons in the conduction band of TiO_2.[35]

Assuming a reaction mechanism where the rate limiting step is activated by a conduction band electron from the titanium oxide support, the electronic structure of the titanium oxide explains the observed trend in reactivity. In the case of $TiO_{1.7}$ and $TiO_{1.9}$, the presence of F

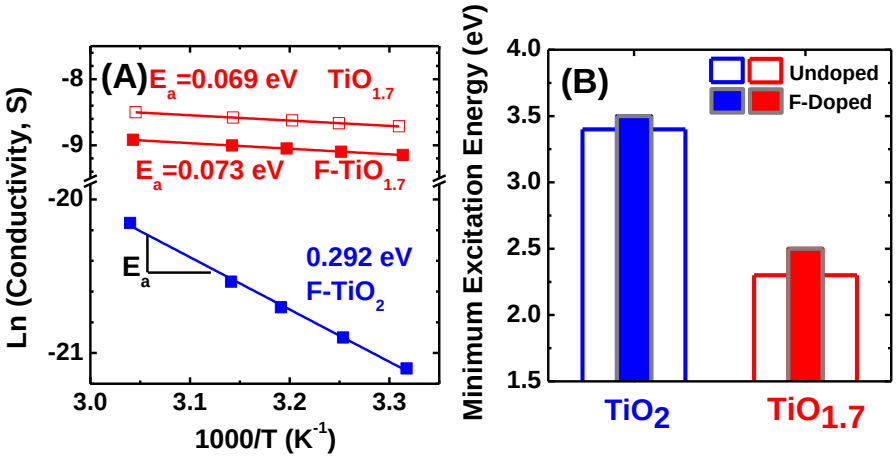

Fig. 2 (A) *Arrhenius plots showing the activation energy for charge transport in $TiO_{1.7}$ and TiO_2. Because TiO_2 without F is highly insulating, the Arrhenius curve could not be accurately measured for this sample. The different activation energies for conduction in $TiO_{1.7}$ and TiO_2 confirm different transport channels as depicted in Fig. 3A.* **(B)** *Minimum excitation energy having a fixed absorption coefficient of 2×10^4 cm^{-1}. This measurement reflects the decrease in bandgap energy for the reduced oxide and shows the difference in the energy of free electrons in the two supports.*

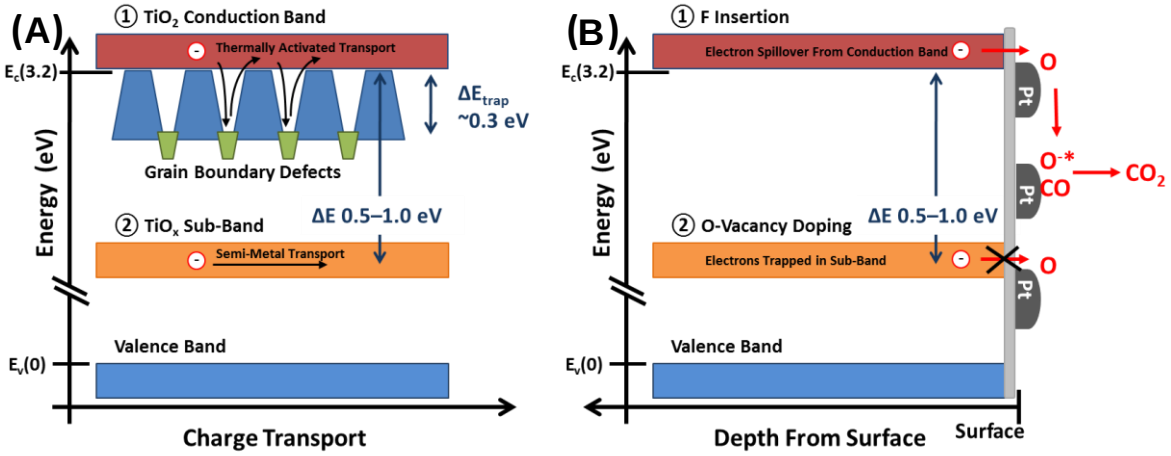

Fig. 3 (A) *Band diagram depicting two types of transport in titanium oxide. Sub-band defect states in the reduced oxide provide a semi-metal transport channel. In stoichiometric TiO_2, transport occurs in the actual conduction band. Due to grain boundary defects, conduction band transport is thermally activated as charges trap and de-trap at grain boundaries.* **(B)** *Schematic depicting why electronic activation is possible by F doping and not by O-vacancy doping. Although a high density of free charge carriers exist in the reduced oxide, these carriers reside in the sub-band located ~0.5–1.0 eV below the conduction band edge. At this low energy, the electrons cannot activate surface O for reaction with CO. However, in stoichiometric TiO_2, electrons reside in the true conduction band. Charge transfer from the conduction band results in electronic activation of surface O for CO_2 formation.*

decreased the surface electron density in the oxide support resulting in a slightly reduced reaction rate. However, because the majority of electrons in these supports reside in the sub-oxide band at an energy that is presumably too low to induce chemistry, changes in electron density have a minimal effect on the reaction rate. In the case of TiO_2 where free carriers reside in the conduction band from which they can spillover to adsorbates, an increase of surface electron density induced by F correlates with a significant increase in catalytic activity by electronic activation.

We propose that the mechanism for electronic activation is electron spillover from TiO_2 to adsorbed O to form an activated O^- intermediate that readily reacts with CO. This is depicted schematically in Fig. 3B. In the case of O vacancy doping, the energy of the sub-oxide band is 0.5–1.0 eV below the conduction band edge. This energy is much higher than kT (≥13 kT at a reaction temperature of 443 K). Consequently, a reaction pathway that is electronically activated by free carriers in the conduction band of TiO_2 would not be thermally accessible until a temperature of ~6,000 K. However, because F insertion to TiO_2 increases the surface concentration of free electrons without formation of any mid-gap states, free electrons reside in the actual conduction band making this material an electronically active support for CO oxidation.

XPS and reaction kinetics provide evidence that electronic activation by the F-doped support occurs by electron spillover to surface O. Fresh catalysts prepared and treated under reaction conditions for 1 h at 373, 473, or 573 K showed significant changes in the O 1s spectrum that correlate with deactivation of the undoped catalyst. Fig. 4A shows the O 1s XPS spectrum for the Pt/TiO_2 catalyst following reaction at various temperatures. The surface O peak at high binding energy (~532.5 eV) increased with reaction temperature. The XPS spectra for the F-doped analog of this catalyst (not shown here) were identical to those shown in Fig. 4A. Fig. 4B shows how the formation of surface O affects the activity of the undoped catalyst. Initially we observe a TOF of ~25 min^{-1} at 443 K; however, following reaction at high temperature (543 K), the catalyst deactivated by a factor of four. The initial activity was restored after removal of surface O by reaction with CO. Treatment in O_2 again resulted in catalyst deactivation by the formation of surface O.

We do not entirely understand the mechanism of catalyst deactivation by surface O, but at present we suggest the following: Surface O is an inactive species occupying catalytic sites, so deactivation is simply a result of blocking active sites with strongly bound O. Additionally, O acts as an electron acceptor, so it is possible that deactivation by surface O is partly an electronic phenomenon. Surface O may bind and localize free electrons in the titanium oxide support that are necessary for activating the catalytic reaction. This suggests that O activation is rate limiting for CO oxidation and is consistent with the idea that electronic activation by the F-doped TiO_2 sample occurs by electron spillover to adsorbed O to form an activated O^- intermediate. Fig. 4C provides further evidence for this theory.

Fig. 4C shows time dependent reaction rate measurements for Pt on each TiO_X stoichiometry and on F-doped TiO_2. Each undoped catalyst deactivated by 20–36% during 1 h under reaction conditions. However, Pt supported on F-doped TiO_2 showed a 49% rate increase. We propose that these kinetics correspond to the formation of surface O during the reaction and

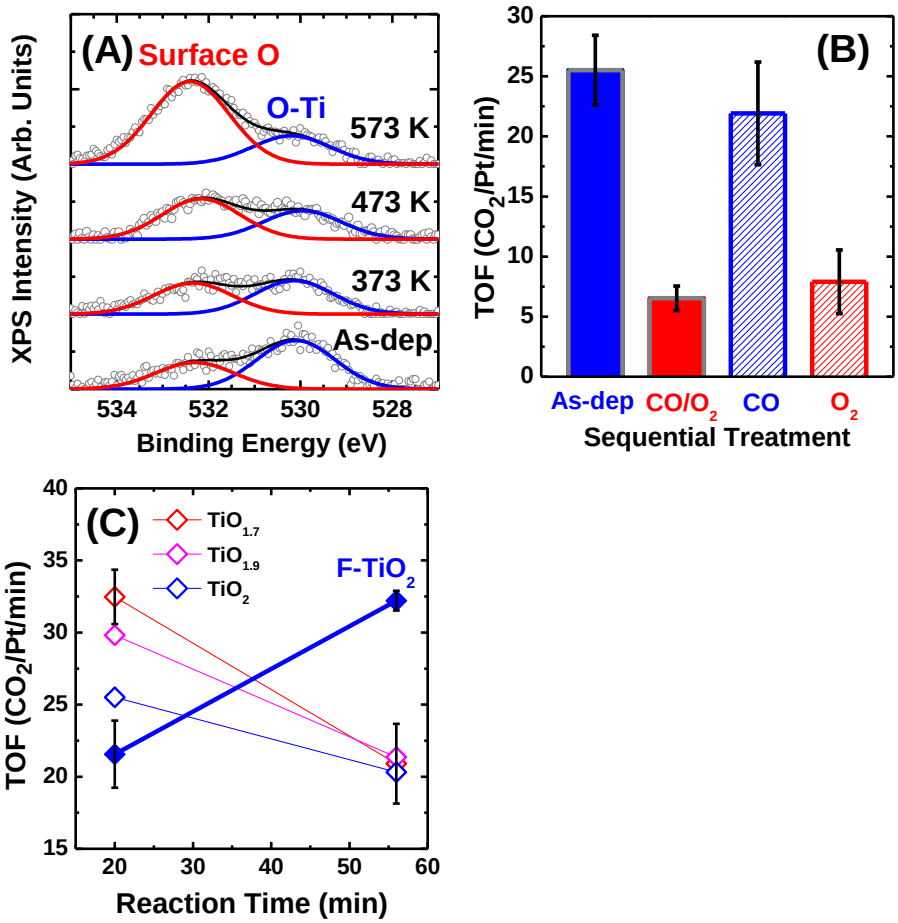

Fig. 4 (A) *O 1s XPS spectrum for the Pt/TiO_2 catalyst as-deposited (As-dep) and after 1 h under reaction conditions at 373, 473, and 573 K. The growth of surface O at high binding energy (~532.5 eV) occurs with increasing reaction temperature.* **(B)** *Turnover frequency (TOF) data revealing the role of surface O to deactivate the undoped catalyst for CO oxidation. Following reaction at elevated temperature, the catalyst deactivated by a factor of four. Removal of surface O by 100 Torr CO at 523 K restored the initial activity. Treatment in 100 Torr O_2 at 523 K again produced surface O resulting in deactivation.* **(C)** *Turnover frequency (TOF) data showing a change in catalyst activity at 443 K over 1 h. In all cases except for the Pt/TiO_2-F, the catalyst deactivated over this time. However, in the case of Pt supported on F-doped TiO_2, the activity increased by 49, indicating that the highly n-type support can electronically activate surface O as it forms for reaction with CO.*

the ability or inability of electrons from the oxide support to activate it for CO_2 formation. The high energy of the electrons in the F-doped stoichiometric support is responsible for enhancing the catalytic activity by electron spillover. However, this effect cannot occur with catalysts containing high concentrations of O vacancies. Although there is a high density of free carriers in these supports, they are trapped in the sub-oxide band structure.

We also investigated the stability of F in reaction conditions at 373, 473, and 573 K. XPS showed that F concentration decreased with increasing reaction temperature and was undetectable after 1 h at 573 K. Fig. 5 shows the F to Ti atomic ratio for F-doped TiO_2 as fabricated and after 1 h in reaction conditions at each of the three treatment temperatures. Although the surface F concentration began to decreases even at 473 K, it was still present at significant levels. Consequently, we safely assume that F remained in the support throughout the duration of the reaction rate measurements shown above which took place at 443 K.

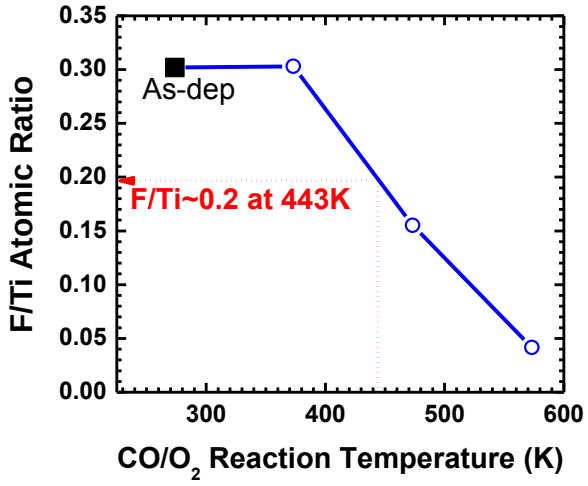

Fig. 5 *F to Ti atomic ratio in F-doped TiO2 as-deposited (As-dep) and after 1 h in reaction conditions at 373, 473, and 573 K. The atomic ratio is based on the integrated intensity of the F 1s and the Ti 2p XPS spectra and corrected for sensitivity factors. The F concentration decreases at increasing temperature, but F is still present up to 473 K.*

6.5 Conclusions

We achieved approximately twofold increase in the reaction rate of CO oxidation on a Pt/TiO_2 catalyst when the TiO_2 is made n-type by F doping. A correlation of this effect with the electronic structure of titanium oxide indicates that the mechanism responsible for increased catalytic activity is activation of surface O by electron spillover from the oxide support.

Noting that certain catalytic reactions proceed by charged intermediates, it seems intuitive that hot carriers can activate non-thermal reaction pathways by spillover to surface adsorbates. Hot carriers are difficult to generate in a metal catalyst because of their fast relaxation times. However, n-type doping of oxide semiconductors is a feasible method for supplying charges of controlled energy to a catalytic interface. This unique utility of oxides also enlightens the widely studied strong metal-support interaction (SMSI), in which the properties of an oxide used to support metal clusters strongly influences the activity and selectivity of the catalyst system.

This result demonstrates that tuning the electronic structure of metal-oxide semiconductors used as catalyst supports can provide access to reaction pathways that on other catalysts would not be thermally accessible. This ability implicates applications in many other

charge mediated processes, including energy conversion reactions, electrochemical processes, solid acid/base catalysis, and selective partial oxidation chemistry.

6.6 References

(1) Schwab, G. M. *Transactions of the Faraday Society* **1946**, *42*, 689.
(2) Tauster, S. J.; Fung, S. C.; Garten, R. L. *Journal of the American Chemical Society* **1978**, *100*, 170.
(3) Tauster, S. J.; Fung, S. C.; Baker, R. T. K.; Horsley, J. A. *Science* **1981**, *211*, 1121.
(4) Tauster, S. J. *Accounts of Chemical Research* **1987**, *20*, 389.
(5) Somorjai, G. A.; Li, Y. *Introduction to surface chemistry and catalysis*; 2nd Edition ed.; Johns Wiley & Sons, Inc.: Hoboken, NJ, 2010.
(6) Boffa, A.; Lin, C.; Bell, A. T.; Somorjai, G. A. *Journal of Catalysis* **1994**, *149*, 149.
(7) Vannice, M. A.; Sen, B. *Journal of Catalysis* **1989**, *115*, 65.
(8) Lin, S. D.; Sanders, D. K.; Albert Vannice, M. *Applied Catalysis A: General* **1994**, *113*, 59.
(9) Malathi, R.; Viswanath, R. P. *Applied Catalysis A: General* **2001**, *208*, 323.
(10) Oh, S. H.; Eickel, C. C. *Journal of Catalysis* **1988**, *112*, 543.
(11) Zhu, H.; Qin, Z.; Shan, W.; Shen, W.; Wang, J. *Journal of Catalysis* **2004**, *225*, 267.
(12) Chen, M. S.; Goodman, D. W. *Science* **2004**, *306*, 252.
(13) Goodman, D. *Catalysis Letters* **2005**, *99*, 1.
(14) Enache, D. I.; Edwards, J. K.; Landon, P.; Solsona-Espriu, B.; Carley, A. F.; Herzing, A. A.; Watanabe, M.; Kiely, C. J.; Knight, D. W.; Hutchings, G. J. *Science* **2006**, *311*, 362.
(15) Landon, P.; Collier, P. J.; Papworth, A. J.; Kiely, C. J.; Hutchings, G. J. *Chemical Communications* **2002**, 2058.
(16) Landon, P.; Collier, P. J.; Carley, A. F.; Chadwick, D.; Papworth, A. J.; Burrows, A.; Kiely, C. J.; Hutchings, G. J. *Physical Chemistry Chemical Physics* **2003**, *5*, 1917.
(17) Fu, Q.; Saltsburg, H.; Flytzani-Stephanopoulos, M. *Science* **2003**, *301*, 935.
(18) Edwards, J. K.; Solsona, B. E.; Landon, P.; Carley, A. F.; Herzing, A.; Kiely, C. J.; Hutchings, G. J. *Journal of Catalysis* **2005**, *236*, 69.
(19) Fan, S.; Yi, J.; Wang, L.; Mi, Z. *Reaction Kinetics and Catalysis Letters* **2007**, *92*, 175.
(20) Vernon, P. D. F.; Green, M. L. H.; Cheetham, A. K.; Ashcroft, A. T. *Catalysis Letters* **1990**, *6*, 181.
(21) Ashcroft, A. T.; Cheetham, A. K.; Green, M. L. H.; Vernon, P. D. F. *Nature* **1991**, *352*, 225.
(22) Nakagawa, K.; Ikenaga, N.; Suzuki, T.; Kobayashi, T.; Haruta, M. *Applied Catalysis A: General* **1998**, *169*, 281.
(23) Haruta, M. *Cattech* **2002**, *6*, 102.
(24) Pietron, J. J.; Stroud, R. M.; Rolison, D. R. *Nano Letters* **2002**, *2*, 545.
(25) Molina, L. M.; Rasmussen, M. D.; Hammer, B. *Journal of Chemical Physics* **2004**, *120*, 7673.
(26) Akubuiro, E. C.; Verykios, X. E. *Journal of Catalysis* **1988**, *113*, 106.
(27) Bonn, M.; Funk, S.; Hess, C.; Denzler, D. N.; Stampfl, C.; Scheffler, M.; Wolf, M.; Ertl, G. *Science* **1999**, *285*, 1042.
(28) Lambert, R. M.; Cropley, R. L.; Husain, A.; Tikhov, M. S. *Chemical Communications* **2003**, 1184.

(29) Zhang, Y.; Kolmakov, A.; Chretien, S.; Metiu, H.; Moskovits, M. *Nano Letters* **2004**, *4*, 403.
(30) Zhang, J.; Liu, X.; Blume, R.; Zhang, A. H.; Schlogl, R.; Su, D. S. *Science* **2008**, *322*, 73.
(31) Kaden, W. E.; Wu, T. P.; Kunkel, W. A.; Anderson, S. L. *Science* **2009**, *326*, 826.
(32) Zhang, Z.; Yates, J. T. *Journal of the American Chemical Society* **2010**, *132*, 12804.
(33) Park, J. Y.; Somorjai, G. A. *Chemphyschem* **2006**, *7*, 1409.
(34) Cox, P. A. *Transition Metal Oxides An Introduction to their Electronic Structure and Properties*; Clarendon Press: Oxford, 1992.
(35) Seo, H.; Baker, L. R.; Hervier, A.; Kim, J.; Whitten, J. L.; Somorjai, G. A. *Nano Letters* **2010**, *11*, 751.

Chapter 7

Controlling the Selectivity of Methanol Oxidation on Platinum Catalysts by Tuning the Electronic Structure of a Titanium Oxide Support by Fluorine Doping

7.1 Abstract

Platinum films of thickness 1 nm were deposited by electron beam evaporation onto 100-nm-thick titanium oxide films (TiO_x) with variable oxygen vacancy concentrations and fluorine (F) doping. Methanol oxidation on the platinum films produced formaldehyde, methyl formate, and carbon dioxide. F-doped samples demonstrated significantly higher activity for methanol oxidation when the TiO_x was stoichiometric (TiO_2), but lower activity when it was non-stoichiometric ($TiO_{1.7}$ and $TiO_{1.9}$). These results correlate with the chemical behavior of the same types of catalysts in CO oxidation. Fluorine doping of stoichiometric TiO_2 also increased selectivity toward partial oxidation of methanol to formaldehyde and methyl formate, but had an opposite effect in the case of non-stoichiometric TiO_x. Introduction of oxygen vacancies and fluorine doping both increased the conductivity of the TiO_x film. For oxygen vacancies, this occurred by the formation of a conduction channel in the bandgap, whereas in the case of fluorine doping, F acted as an n-type donor, forming a conduction channel at the bottom of the conduction band, about 0.5-1.0 eV higher in energy. The higher energy electrons in F-doped stoichiometric TiO_x led to higher turnover rates and increased selectivity toward partial oxidation of methanol. This correlation between electronic structure and turnover rate and selectivity indicates that the ability of the support to transfer charges to surface species controls in part the activity and selectivity of the reaction.

7.2 Introduction

Heterogeneous catalysts often consist of metal nanoparticles dispersed over an oxide support. While the oxide is usually inert by itself, it may affect the catalyst's behavior in significant ways, a phenomenon known as strong metal support interaction.[1,2] This phenomenon is in part attributed to charge transfer involving the oxide support.[3] For example, it has been observed that partially covering Rh foil with an oxide enhanced the reaction rates for hydrogenation of CO and CO_2,[4] despite the fact that the oxide was not active by itself and blocked the active Rh sites. The enhancement factor was found to correlate with the Lewis acidities of the oxides used, i.e., their ability to accept a charge. These results suggest that modifying the conditions for charge transfer from the oxide support may yield significant changes in catalytic behavior.

In the present study, methanol oxidation was carried out over Pt/TiO_2 catalysts for which the oxide was modified by introducing oxygen vacancies and fluorine dopant. It is reported that fluorine doping of stoichiometric TiO_2 allows the oxide to transfer an electron to an adsorbate.

This activates one or multiple steps in the reaction, leading to a significant increase both in turnover frequency and selectivity toward the partial oxidation products, formaldehyde and methyl formate. The present study is the first to correlate a change in selectivity due to doping of the oxide support with the charge transfer properties of the oxide. Results indicate that reaction selectivity is controlled, to a significant extent, by charge transfer from the oxide.

The aforementioned results are consistent with a previous study of CO oxidation on Pt/TiO_x catalysts.[5] In that study, TiO_x films were annealed under different conditions to obtain various stoichiometries, i.e., $TiO_{1.7}$, $TiO_{1.9}$, and TiO_2, as determined by X-Ray photoelectron spectroscopy (XPS). Introducing oxygen vacancies into TiO_2 leads to the formation of electronic states in the bandgap about 0.5–1.0 eV below the bottom of the conduction band.[6,7] These midgap states act as a conduction channel, and the conductivity of the film increases by orders of magnitude.[8,9]

One titanium oxide film of each sample was also doped in SF_6 plasma, yielding six types of oxide support: $TiO_{1.7}$, $TiO_{1.9}$, and TiO_2, both doped and undoped. Fluorine was found to bind to Ti by filling oxygen vacancies, slightly offsetting the increased conductivity.[9] However, F also acts as an n-type donor, forming donor levels just below the conduction band. For TiO_2, this increases conductivity by forty-fold (Fig. 1B). In the presence of oxygen vacancies, the vacant midgap states 0.5–1.0 eV below the bottom of the conduction band capture any donor electrons, and F doping slightly decreases the conductivity of the $TiO_{1.7}$ and $TiO_{1.9}$ films.[9]

While both oxygen vacancies and fluorine doping can increase the film conductivity, the resulting conduction channels are about 1.0 eV apart in energy. This difference correlates with the surface chemistry of the Pt/TiO_x catalysts. Although the turnover frequency (TOF) increases by nearly two-fold when stoichiometric TiO_2 is F-doped, no such increase is observed with the non-stoichiometric $TiO_{1.7}$ and $TiO_{1.9}$ films (Fig. 1A).

Kinetic measurements of this particular system indicated that O poisons the reaction in this range of temperature and pressure. As a result, the increase in turnover may be attributed to electron transfer from the oxide to surface O, activating it for reaction with CO. Non-stoichiometric TiO_x does not show this effect because the conduction channel formed by midgap states is much lower in energy. Electrons in those states have insufficient energy to transfer to surface O.

The above information suggests that the turnover rates of a catalyst can be tuned by modifying the electronic structure of the support. An important contribution of the present investigation is the proof that the same method can be used to tune selectivity, a metric of great importance in industrial catalysis. Methanol oxidation (Scheme 1) was chosen for this purpose because it is relatively simple (only three different products are produced under the conditions of this study) and turnover can easily be measured at 333 K. At this temperature, the fluorine concentration in the TiO_2 lattice is stable.[5] The reaction begins with the adsorption of methanol that leads to the formation of methoxy, which then dehydrogenates to form formaldehyde that can either bind with O to form CO_2, or with methoxy to form methyl formate.[10] Methyl formate conversion to CO_2 was not observed at 333 K. This reaction is of major industrial relevance, because it is the primary method of producing formaldehyde,[11] also forming the basis of operation of the direct methanol fuel cell.[12] In the former, methanol must only be partially

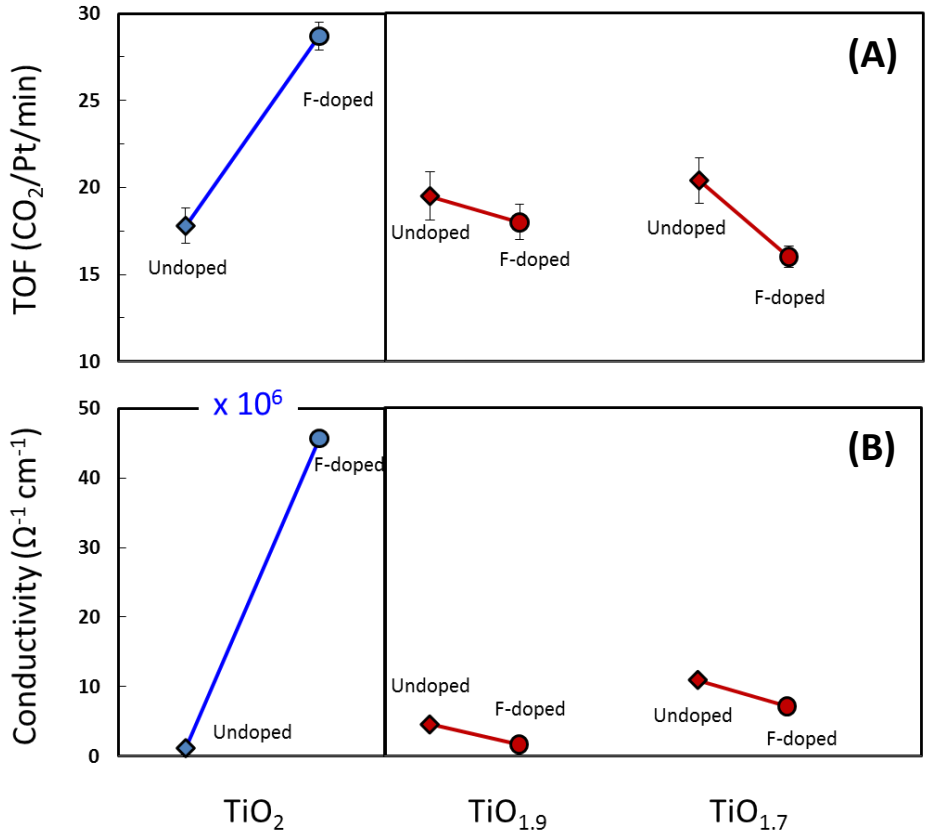

Fig. 1 (A) *Turnover frequencies (TOF) for Pt/TiO_x catalysts identical to those of the present study reported for CO oxidation.*[5] *Fluorine doping only shows a significant effect for stoichiometric TiO_2. Reaction occurred at 443 K under conditions of 40 Torr CO, 100 Torr O_2, and 620 Torr He. TOF data represent stable rates obtained after 30 min in reaction conditions, when deactivation had stopped.* **(B)** *Surface conductivity measurements for the same set of TiO_x supports prior to Pt deposition.*[5] *The numbers for TiO_2 and F-doped TiO_2 have been magnified by a factor of 10^6 for clarity.*

oxidized, whereas in the latter, the energy efficiency is maximized if the oxidation is carried out to form only CO_2; hence the need for selectivity control.

7.3 Experimental

7.3.1 Catalyst Preparation

Thin films of TiO_x with variable O vacancy concentrations were used as supports of the Pt catalyst. These films were deposited on Si(100) wafers by direct current (DC) magnetron sputtering under conditions of 400 W plasma power, 450 V bias voltage, and Ar and O_2 gas flow rates of 50 and 3 sccm, respectively.

The Si(100) wafers had a 500-nm-thick thermally grown SiO_2 film, while the thickness of the TiO_2 films was equal to 100 nm. As-deposited titanium oxide films were highly O deficient. The O concentration in the films was controlled by rapid thermal annealing in O_2 at temperatures

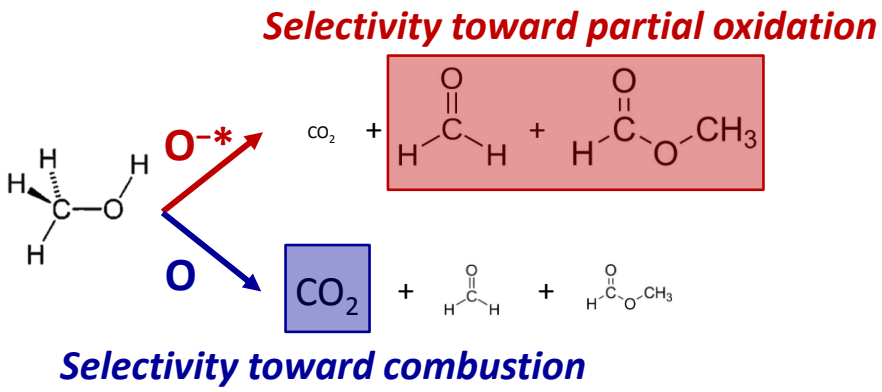

Scheme 1

between 623 and 773 K. To avoid variations in grain size due to the different annealing temperatures, all samples were first annealed in N_2 at 773 K. TiO_x films of three different stoichiometries were prepared for this study, i.e., TiO_2, $TiO_{1.9}$, and $TiO_{1.7}$. These stoichiometries were determined from the ratio of Ti^{3+} and Ti^{4+} in the Ti 2p XPS spectra.[9]

Fluorine doping was accomplished by plasma treatment in N_2 gas and trace amounts of sulfur hexafluoride (SF_6), introduced into the chamber by flowing a 9:1 mixture of SF_6 and O_2, followed by pumping to a chamber base pressure of 5 mTorr. A low background pressure of SF_6 remained in the chamber after pumping. N_2 gas was then introduced at a flow rate of 80 sccm for plasma treatment under conditions of 20 W power and 130 V DC substrate bias. XPS analysis of the F-doped samples did not reveal any S traces.[9] One of the two samples of each TiO_X stoichiometry was plasma treated, resulting in six supports for subsequent Pt deposition, i.e., TiO_2, $TiO_{1.9}$, and $TiO_{1.7}$, each with and without F doping. All substrates were stored in dry N_2 between the time of fabrication and the reaction rate measurements.

Pt nanoparticles were deposited onto TiO_x/Si(100) substrates by electron-beam evaporation. This deposition method was selected instead of colloidal synthesis to avoid the presence of an insulating polymer capping agent between the Pt nanoparticles and the oxide support. During electron beam evaporation, the chamber base pressure was less than 10^{-5} Torr. The average Pt film thickness, monitored by a quartz crystal microbalance, was equal to about 1 nm.

7.3.2 Reaction Rate Measurements

Reaction rates of methanol oxidation on each of the six catalysts described above were measured with a batch mode reactor equipped with a boron nitride substrate heater and a metal bellows circulation pump for gas mixing. In reaction, gas pressures were set at 10 Torr CH_3OH and 50 Torr O_2 in He background, while the temperature was fixed at 333 K. All of the samples showed significant deactivation (up to two orders of magnitude) in the first 60 min of reaction, thereafter producing stable rates for several hours. Rates reported here refer to the steady-state rates obtained after initial deactivation.

Turnover rates were measured by a gas chromatograph (GC) with a thermal conductivity detector. Selectivities were estimated after calibrating the detector's response by injecting known amounts of CO_2 and methyl formate. Because it was difficult to obtain formaldehyde in pure form, the same calibration could not be performed. Therefore, the thermal conductivity of formaldehyde was assumed to be the same as that of methyl formate.

Formaldehyde and methyl formate are treated together and referred to as partial oxidation products. For some samples, the production rate of formaldehyde was less than its consumption rate, leading to a negative turnover number. That rate was counted as contributing negatively to selectivity for partial oxidation. Selectivities reported here should not be compared directly to other results in the literature, and are only used for relative comparisons between samples of this study.

Reaction rates are presented in the form of turnover frequencies (i.e., number of CO_2 molecules per Pt site per minute). Error bars represent a 95% confidence interval based on the rate of production normalized by the estimated number of Pt sites. Assuming a Pt(111) surface of uniform structure, the number of Pt sites was determined as the number of Pt atoms over the catalyst area. Although this is an approximate calculation, it provides consistent normalization to catalyst area and a reasonable estimate of the absolute turnover rate.

7.4 Results and Discussion

Methanol oxidation was carried out on Pt/TiO_x catalysts that differed only in the preparation of the oxide support. As mentioned earlier, the oxide support was modified by oxygen vacancy doping and fluorine doping. Fig. 2 shows the effect of these treatments on the turnover frequencies of the three products, CO_2, formaldehyde, and methyl formate. The graph shows the difference between turnover frequencies of F-doped and undoped samples, □(TOF). In the case of stoichiometric TiO_2, fluorine doping increased activity – TOF increased by 71% for CO_2, two-fold for formaldehyde, and four-fold methyl formate. An opposite trend was observed for non-stoichiometric TiO_2, i.e., $TiO_{1.9}$ and $TiO_{1.7}$. Variation in oxygen vacancy concentration also exhibited a significant effect on activity, although a clear trend cannot be established.

A similar fluorine effect was observed when measuring the selectivity of the reaction. Fig. 3 shows the percentage of partial oxidation products (combining formaldehyde and methyl formate) obtained in reaction, as opposed to the total oxidation product, CO_2. For stoichiometric TiO_2, fluorine doping increased the selectivity toward partial oxidation from 17 to 35%, whereas for non-stoichiometric TiO_2, selectivity toward partial oxidation decreased as a result of fluorine doping.

The effects of fluorine doping observed here are consistent with a previous study dealing with CO oxidation.[5] In that study, the same catalysts produced turnover frequencies for CO oxidation that correlated strongly with the conductivities of the TiO_x films prior to Pt deposition (Fig. 1). Selectivities and turnover frequencies reported here for methanol oxidation also correlate with conductivity measurements (Fig. 1B), suggesting that the same phenomenon governs the effect of fluorine in both reactions.

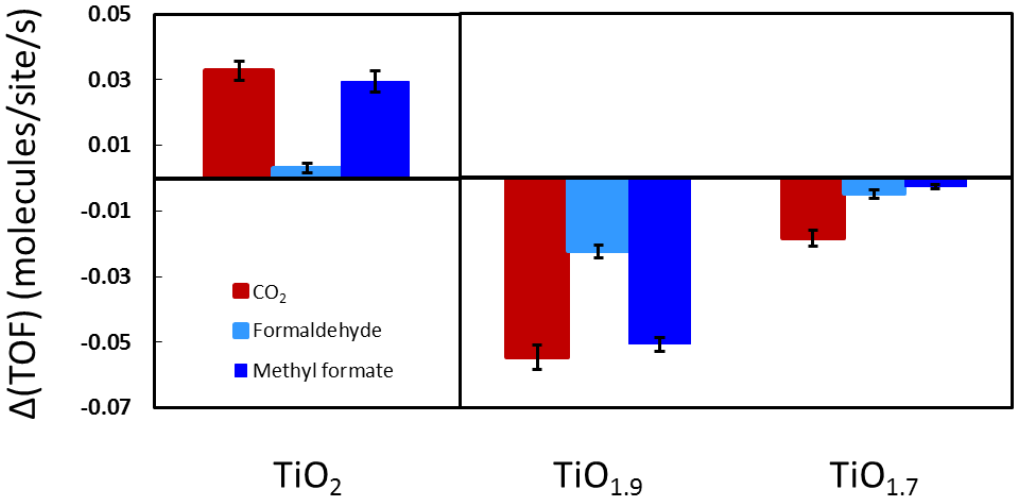

Fig. 2 *Change in turnover frequency Δ(TOF) of CO_2, formaldehyde, and methyl formate products of methanol oxidation over Pt catalysts on six different TiO_x supports: $TiO_{1.7}$, $TiO_{1.9}$, and TiO_2, both doped and undoped. Δ(TOF) denotes the difference in turnover frequency between F-doped and undoped TiO_x supports. Error bars represent 95% confidence intervals. Measurements were obtained at 333 K under reaction conditions of 10 Torr CH_3OH, 50 Torr O_2, and 720 Torr He.*

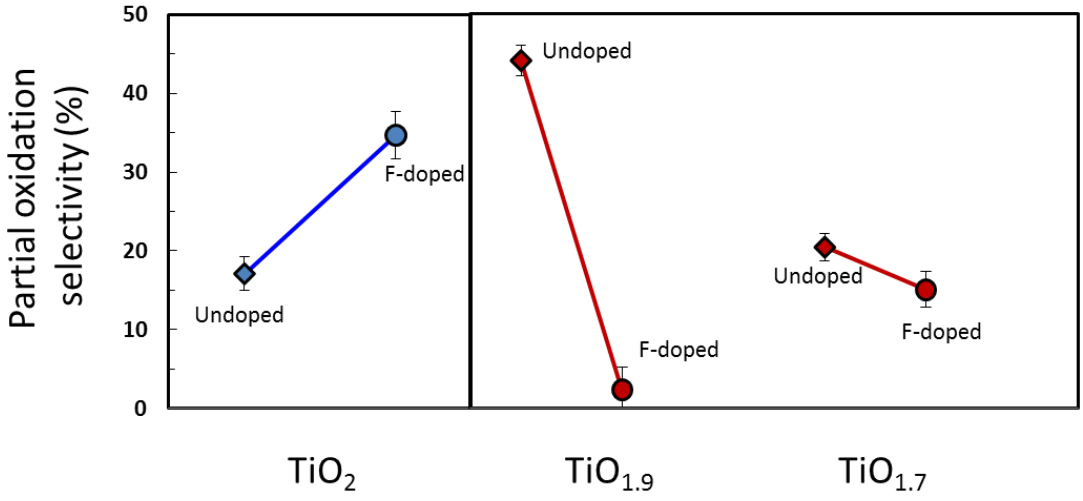

Fig. 3 *Selectivity toward partial methanol oxidation of F-doped and undoped Pt/TiO_x catalysts. Partial oxidation products refer to formaldehyde and methyl formate, as opposed to total oxidation that produces CO_2.*

Differences in activities observed in this study can be explained by considering the charge transfer mechanism in non-stoichiometric and F-doped stoichiometric TiO_2, shown schematically in Fig. 4. TiO_2 has a bandgap of 3.2 eV, and the density of electronic states in the bandgap, by definition, is very low for stoichiometric TiO_2. Oxygen vacancies introduced into the lattice give rise to energy levels in the bandgap (midgap states) between 0.5 and 1.0 eV

below the bottom of the conduction band,[6] increasing dramatically the conductivity of the material (Fig. 1B). Fluorine binding to Ti at O vacancy sites partially passivates these midgap states, resulting in lower conductivity.[9] However, in the case of stoichiometric TiO_2, where there are no midgap states, fluorine acts as an n-type dopant, creating donor states just below the conduction band. This increases conductivity by a factor of 40 (Fig. 1B).

Both oxygen vacancy doping and fluorine doping produce a population of surface electrons available for conduction. These electrons may also transfer to nearby adsorbate orbitals, provided they are close in energy. For CO oxidation, this charge transfer occurs in F-doped stoichiometric TiO_2 from the oxide to surface O, which activates the O to react with CO, leading to increased turnover rate.[5] For oxygen-vacancy doped TiO_2, midgap electrons produced from oxygen doping are lower in energy by 0.5-1.0 eV. Because these electrons cannot transfer to surface O, an increase in turnover is not observed. The effect of fluorine is observed under steady-state conditions, excluding the possibility of charge accumulation. Therefore, the charged intermediate must return its additional electron to the oxide support before desorbing as a CO_2 molecule. Such a scheme of CO oxidation on platinum has been described in a previous theoretical study.[13] In the last step of the reaction, a charged CO_2^- intermediate simultaneously undergoes desorption and loss of an electron to yield CO_2.

In the case of methanol oxidation, it is likely that the same activation of a surface species is responsible for the increased turnover and the shift in selectivity toward formaldehyde and methyl formate. Further experiments must be carried out to identify which species on the surface is activated by the support.

A sharp decrease in turnover rate (up to two orders of magnitude) was observed after approximately 60 min in reaction with each sample, regardless of oxidation state or doping, due to CO poisoning of the Pt layer. Initial rates obtained before the deactivation did not show a dependence on the TiO_2 substrate, and the turnover frequencies reported here refer to the steady-state rates obtained after initial deactivation.

Deactivation was found to be reversible. When the sample was cooled down to room temperature, the gases pumped out, and the reaction restarted, original rates were restored, and the same deactivation occurred after about 60 min, without any significant change in turnover rates. CO produced from methanol oxidation is known to poison Pt.[14] When 0.5 Torr of CO was added to the reaction mixture, turnover rates at 333 K decreased below the detection limit. After the surface was cooled down to room temperature, the reactor evacuated, and a new reaction was initiated on the same sample without any CO, the turnover rate was restored to its previous value. This suggests that, although CO was not produced in amounts detectable by GC, it resulted in Pt poisoning. The reversibility of poisoning indicates that, even at room temperature, a monolayer of CO is easily removed when the reaction is stopped, in agreement with earlier observations.[15]

7.5 Conclusions

Methanol oxidation over Pt/TiO_x catalysts showed that fluorine doping of stoichiometric TiO_2 increases the selectivity toward the formation of formaldehyde and methyl formate from 17 to 35%. The activities and selectivities of the fabricated Pt/TiO_x samples closely followed the conductivities of F-doped TiO_x films, similar to CO oxidation. This effect is likely due to an

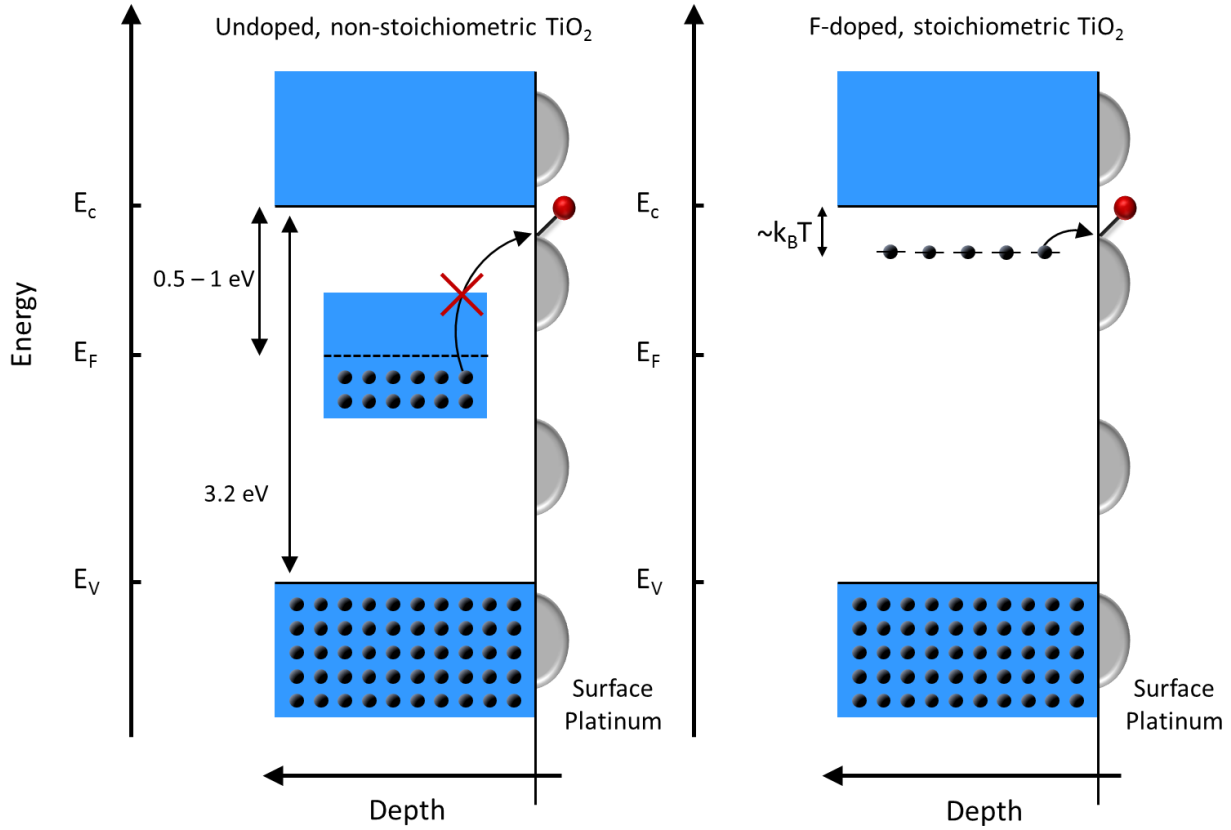

Fig. 4 *Schematic of charge transfer mechanism in non-stoichiometric TiO_x and F-doped stoichiometric TiO_2. In the presence of midgap states, electron transfer from the oxide to an adsorbate species involves an electron with energy between 0.5 and 1.0 eV below the bottom of the conduction band. In the case of F-doped TiO_2, donor electrons occupy states at the bottom of the conduction band that were previously not thermally accessible. These higher energy electrons may transfer to an adsorbate species, resulting in higher turnover frequency and enhanced selectivity toward partial oxidation. (E_c, E_F, and E_v denote conduction, Fermi, and valence energy levels, respectively.)*

increased electron population in the conduction band of the oxide, allowing for charge transfer that activated a surface species. The present study is the first to show that the electronic structure of the oxide support can be tuned to control the oxidation pathways on catalyst surfaces.

7.6 References

(1) Schwab, G.-M. *Discussions of the Faraday Society* 1950, *8*, 166.
(2) Tauster, S. J.; Fung, S. C.; Garten, R. L. *J. Am. Chem. Soc.* 1978, *100*, 170.
(3) Jochum, W.; Eder, D.; Kaltenhauser, G.; Kramer, R. *Topics in Catalysis* 2007, *46*, 49.
(4) Boffa, A. B.; Lin, C.; Bell, A. T.; Somorjai, G. A. *Catalysis Letters* 1994, *27*, 243.
(5) Baker, L. R.; Hervier, A.; Seo, H.; Kennedy, G.; Komvopoulos, K.; Somorjai, G. A. *J. Phys. Chem. C* 2011, *115*, 16006.
(6) Cronemeyer, D. C. *Phys. Rev.* 1959, *113*, 1222.

(7) Asahi, R.; Morikawa, T.; Ohwaki, T.; Aoki, K.; Taga, Y. *Science* 2001, *293*, 269.
(8) Bilmes, S. A.; Mandelbaum, P.; Alvarez, F.; Victoria, N. M. *J. Phys. Chem. B* 2011, *104*, 9851.
(9) Seo, H.; Baker, L. R.; Hervier, A.; Kim, J.; Whitten, J. L.; Somorjai, G. A. *Nano Lett.* 2011, *11*, 751.
(10) Outka, D. A.; Madix, R. J. *J. Am. Chem. Soc.* 2011, *109*, 1708.
(11) Weissermel, K.; Arpe, H.-J. *Industrial organic chemistry*; Wiley-VCH, 2003.
(12) Surampudi, S.; Narayanan, S. R.; Vamos, E.; Frank, H.; Halpert, G.; LaConti, A.; Kosek, J.; Prakash, G. K. S.; Olah, G. A. *Journal of Power Sources* 1994, *47*, 377.
(13) Maximoff, S. N.; Head-Gordon, M. P. *Proceedings of the National Academy of Sciences* 2009, *106*, 11460.
(14) Beden, B.; Hahn, F.; Leger, J.-M.; Lamy, C.; Lopes, M. I. dos S. *Journal of Electroanalytical Chemistry and Interfacial Electrochemistry* 1989, *258*, 463.
(15) Zhang, C.; He, H. *Catalysis Today* 2007, *126*, 345.

Chapter 8

Furfuraldehyde Hydrogenation on Titanium Oxide-Supported Platinum Nanoparticles Studied by Sum Frequency Generation Vibrational Spectroscopy: Acid–Base Catalysis Explains the Molecular Origin of Strong Metal–Support Interactions

8.1 Abstract

This work describes a molecular-level investigation of strong metal–support interactions (SMSI) in Pt/TiO_2 catalysts using sum frequency generation (SFG) vibrational spectroscopy. This is the first time that SFG has been used to probe the highly selective oxide–metal interface during catalytic reaction, and the results demonstrate that charge transfer from TiO_2 on a Pt/TiO_2 catalyst controls the product distribution of furfuraldehyde hydrogenation by an acid–base mechanism. Pt nanoparticles supported on TiO_2 and SiO_2 are used as catalysts for furfuraldehyde hydrogenation. As synthesized, the Pt nanoparticles are encapsulated in a layer of poly(vinylpyrrolidone) (PVP). The presence of PVP prevents interaction of the Pt nanoparticles with their support, so identical turnover rates and reaction selectivity is observed regardless of the supporting oxide. However, removal of the PVP with UV light results in a 50-fold enhancement in the formation of furfuryl alcohol by Pt supported on TiO_2, while no change is observed for the kinetics of Pt supported on SiO_2. SFG vibrational spectroscopy reveals that a furfuryl-oxy intermediate forms on TiO_2 as a result of a charge transfer interaction. This furfuryl-oxy intermediate is a highly active and selective precursor to furfuryl alcohol, and spectral analysis shows that the Pt/TiO_2 interface is required primarily for H spillover. Density functional calculations predict that O-vacancies on the TiO_2 surface activate the formation of the furfuryl-oxy intermediate via an electron transfer to furfuraldehyde, drawing a strong analogy between SMSI and acid–base catalysis.

8.2 Introduction

Strong metal–support interactions (SMSI) refer to the ability of a seemingly inert oxide to have a dominant effect on the catalytic properties of a supported metal nanoparticle.[1-4] Tauster and Fung first used the term SMSI to refer to the dramatic loss of chemisorption sites observed for noble metal catalysts supported on titanium oxide after reduction.[2] In their studies, Tauster and Fung showed evidence for a strong bonding interaction between metal nanoparticles and a reduced titanium oxide support, and they used the term SMSI to refer directly to this bonding interaction.[4] However, because this metal–support interaction is closely linked to the catalytic properties of the metal involved, the definition of SMSI has since expanded to broadly refer to support-induced changes in the catalytic activity and selectivity of metal nanoparticles. SMSI plays an important role to enhance many catalytic reactions, including CO oxidation,[5-9] CO and CO_2 hydrogenation,[10,11] hydroformylation,[12] and partial hydrogenation reactions.[13-17] The ability

of an oxide support to mediate the catalytic behavior of a supported metal nanoparticle is an important area in catalysis with both scientific and commercial significance. However, more than 30 years since its discovery, the mechanism of SMSI catalysis remains an open question.

A number of studies show that the support plays an important role in activating the C=O bond. A correlation of the catalyst activity for C=O bond hydrogenation with the Lewis acidity of the oxide empirically shows that charge transfer between the C=O bond and cationic sites in the oxide controls C=O bond activation.[11,18-20] This observation points out a similarity between SMSI and acid–base catalysis. In acid–base catalysis, the generation of ionic reaction intermediates determines the reaction rate and selectivity because the charged intermediate is highly active for a specific reaction pathway.[21-23] In SMSI the oxide appears to play a similar role: electron transfer between a reactant molecule and the oxide support leads to the formation of a charged reaction intermediate that may be highly selective to a specific reaction pathway. This hypothesis, which explains why SMSI can dramatically enhance the rate of a single reaction pathway, is confirmed in this study by direct observation of reaction intermediates on supported metal catalysts. These results show that SMSI catalysis is a subclass of acid–base chemistry where the flow of charge determines both reaction rate and selectivity.

In the current study, Pt nanoparticles supported on TiO_2 and SiO_2 serve as catalysts for furfuraldehyde hydrogenation. The Pt/SiO_2 catalyst serves a reference state, because SiO_2 is not SMSI active.[3] We investigate the effects of the support on the catalyst selectivity and correlate kinetic measurements with the surface intermediates observed by sum frequency generation (SFG) vibrational spectroscopy. SFG vibrational spectroscopy has been previously used to observe surface reaction intermediates on metal single crystals and shape controlled metal nanoparticles.[24-27] In this study, SFG is used for the first time to study, at a molecular level, how an oxide support controls the selectivity of a metal nanoparticle.

We find that initially the support has no effect on the reaction kinetics. This is because a layer of poly(vinylpyrrolidone) (PVP) encapsulates the Pt nanoparticles and insulates the Pt from the oxide support. However, by controlled removal of the PVP using UV light,[28] direct contact between the nanoparticles and the oxide support results in a new Pt/support interface. In the case of Pt/TiO_2, this interface leads to a 50-fold enhancement in the formation of furfuryl alcohol, while the Pt/SiO_2 interface has no effect on the reaction kinetics. By SFG we observe that a furfuryl-oxy intermediate forms on the TiO_2 as a result of a Lewis acid–base interaction with the furfuraldehyde molecule. This furfuryl-oxy intermediate is a highly active and selective precursor to furfuryl alcohol. Spectral analysis reveals that the Pt/TiO_2 interface is required primarily for H_2 spillover from the Pt. Density functional calculations identify O-vacancies on the TiO_2 surface as the catalytically active site and show that the barrier to C=O bond hydrogenation is dramatically decreased as a result of furfural bonding at the reduced Ti^{3+} sites surrounding an O-vacancy. This represents a detailed molecular understanding of the support-enhanced reaction mechanism for an SMSI catalyst and demonstrates a strong similarity between SMSI and acid–base catalysis.

8.3 Experimental

8.3.1 Catalyst Preparation

To study support effects, 2-dimensional model catalysts were prepared by depositing Pt nanoparticles onto two different metal-oxide thin films. SiO_2 and TiO_2 served as the two supports. As synthesized, the Pt nanoparticles were encapsulated in a layer of PVP. This capping layer prevented actual contact between the Pt nanoparticle and the oxide support. However, by photodecomposition of the PVP, the Pt nanoparticles were brought into contact with the oxide support. By controlling the degree of contact between the particle and the support, the effect of the oxide-metal interface on catalytic activity and selectivity was studied.

The Pt nanoparticles were synthesized from chloroplatinic acid hexahydrate and PVP in a 1:4 mass ratio. In a small beaker, 110 mg of chlorplatinic acid was dissolved in 10 mL ethylene glycol. In a separate beaker, 440 mg of PVP was dissolved in 10 mL of ethylene glycol. Once in solution, the two mixtures were combined into a 50 mL two-neck round bottom flask fitted with an Ar flow. The solution was purged under vacuum for 15 min. The vessel was then heated to 438 K for 1 h with vigorous mixing under a flow of Ar. The resulting nanoparticles were precipitated with acetone and washed three times with ethanol and hexanes. The nanoparticles were then suspended in chloroform for Langmuir Blodgett (LB) deposition. Transmission electron microscopy (TEM) showed that the particles were 4.6 ± 2.8 nm.

Two substrates were used to support the nanoparticles: SiO_2 and TiO_2. For reaction studies, a Si(100) wafer with a 500 nm thermally grown oxide served as the SiO_2 support. The TiO_2 support consisted of a 50 nm TiO_2 thin film deposited on the SiO_2 substrate by electron beam evaporation. Following deposition, the TiO_2 thin film was annealed at 773 K in O_2. Analogous samples were prepared for sum frequency generation spectroscopic studies. For these samples, an optically transparent substrate was needed. A sapphire window rather than a Si wafer served as the substrate. A 50 nm thin film of SiO_2 or TiO_2 was deposited on the sapphire window by electron beam evaporation, again followed by annealing at 773 K in O_2 to ensure oxide stoichiometry.

The LB technique was then used to deposit a monolayer of the Pt nanoparticles onto the metal-oxide supports. This technique has been described previously in detail.[25,29] In short, a suspension of nanoparticles in chloroform is dispersed onto a water surface (18 MΩ). Time is given for the chloroform to evaporate, leaving a 2-dimensional dispersion of nanoparticles on the water surface. The film is then compressed with a mobile barrier, and the surface pressure is monitored as a function of decreasing surface area. The surface pressure corresponds to the density of nanoparticles on the water. When the desired surface pressure is reached, a substrate is pulled out from under the surface of the water, and the film of nanoparticles is deposited onto the substrate. The final density of nanoparticles on the substrate can be controlled by controlling the surface pressure during deposition. A surface pressure of 14 mN/m was used for these studies, and films were deposited using a Nima 611 LB trough. Filter paper served as the surface tension probe. Prior to LB deposition the substrate was cleaned for 1 h in Nochromix solution. TEM showed that the area coverage for Pt on the substrate following LB was approximately 30%.

Immediately prior to reaction, the samples were exposed to UV light in air to photodecompose the PVP layer that encapsulated the nanoparticles. Two low-pressure mercury (Hg) lamps (Lights Sources Inc., model number GPH357T5VH/4P) were used as the UV source; the Hg lamp emitted two lines: 184 and 254 nm. The two lamps were positioned parallel to each other 2.5 cm apart in a clean Al box. The sample was positioned 1.2 cm below the lamps. By varying the time of UV exposure, it was possible to control the amount of PVP removed from the Pt nanoparticles. This cleaning is the combined effect of direct photodecomposition of the PVP as well as oxidation of the PVP by ozone produced by the 184 nm Hg line.[28]

8.3.2 Activity and Selectivity Measurements

A stainless steel batch mode reactor was used to determine the reaction rates and selectivity of furfuraldehyde hydrogenation for Pt supported on SiO_2 and TiO_2 with varying degrees of PVP cap removal. The catalyst was heated with a boron nitride substrate heater to a reaction temperature of 393 K. A metal bellows circulation pump provided gas mixing. Gas pressures were 1 Torr furfuraldehyde, 100 Torr H_2, and 659 Torr He. The furfuraldehyde was purified by freeze-pump-thaw cycles. Each catalyst was tested for 8 h and reaction products were monitored as a function of time using a gas chromatograph with a flame ionization detector.

To calculate a turnover frequency (TOF) for each catalyst, it was necessary to determine the number of Pt active sites. Because ethylene hydrogenation is insensitive to Pt structure[30] and support,[11] the number of active sites for each catalyst was determined by measuring the rate of ethylene hydrogenation and normalizing to a known TOF.[31] Ethylene hydrogenation was run on each catalyst following furfuraldehyde hydrogenation in a separate but identical reactor, and catalysts were stored under N_2 between reactions. The catalyst temperature for the ethylene reaction was 298 K, and gas pressures were 10 Torr ethylene and 100 Torr H_2 in a background of He.

Turnover frequencies for furfuraldehyde hydrogenation are based on the reaction rate, measured from a fit to peak area versus time, and normalized to the number of active sites as determined by ethylene hydrogenation. Selectivity measurements for furfuraldehyde hydrogenation are calculated as the TOF of a given product normalized to the combined TOF of all products. Error bars represent 95% confidence intervals for these measurements.

8.3.3 Sum Frequency Generation Vibrational Spectroscopy

Sum frequency generation (SFG) is a second order, nonlinear process that probes the $X^{(2)}$ tensor. Because $X^{(2)}$ is zero for centrosymmetric media, SFG is only sensitive to a break in inversion symmetry which usually occurs at a surface or interface. Consequently, SFG is useful for obtaining vibrational spectra of surfaces. In this study, SFG is used to obtain the vibrational spectra of molecules on the catalyst surface during reaction. Comparison of reaction intermediates on Pt nanoparticles supported on SiO_2 and TiO_2 demonstrates that a unique reaction pathway is active on the Pt/TiO_2 catalyst.

For SFG experiments, an active/passive mode-locked Nd:YAG laser (Leopard D-20, Continuum) produced a 20 ps pulse at a 20 Hz repetition rate. The fundamental output at 1064 nm was passed through an optical parametric generator/amplifier to generate a tunable infrared (IR) beam (2700–3600 cm^{-1}) and a second harmonic visible (VIS) beam (532 nm). The IR

(100 μJ) and VIS (100 μJ) beams were spatially and temporally overlapped on the back surface of a sapphire window containing the Pt nanoparticles supported on SiO_2 or TiO_2 thin films. The VIS and IR beam were incident on the sample at 40° and 50° degrees, respectively, relative to surface normal. The generated SFG signal was then collected and sent to a photomultiplier tube. A gated integrator was used to enhance the signal-to-noise. To collect a spectrum, the IR beam was scanned across the spectral range of interest. All experiments were performed in the ppp polarization combination.

The beams were directed onto the sample using a sapphire prism as shown in Fig. 1. A solution of deuterated polystyrene (d8) in deuterated decalin (d18) served as an index matching liquid that did not interfere with transmission of the IR beam at the C-H stretch frequency. The catalyst surface was pressed into thermal contact with an aluminum heating block to heat the catalyst to reaction temperature. A recess in the heating block allowed for the flow of reaction gasses across the catalyst surface. A metal bellows circulation pump provided gas mixing. A gas tight seal was made between the sapphire window and the heating block using a Kalrez O-ring.

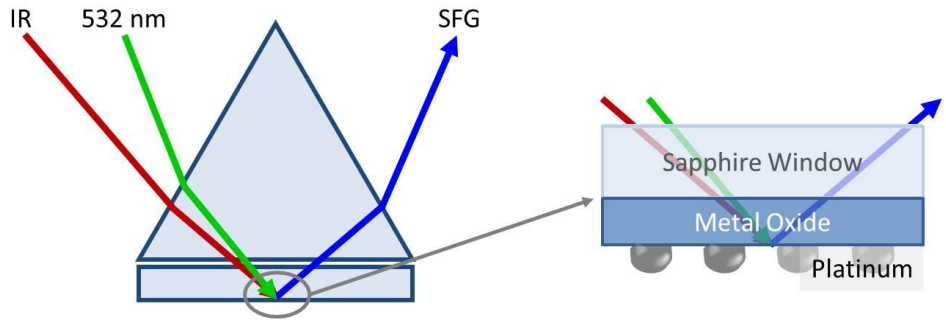

Fig. 1 *Diagram showing how a sapphire prism directed the VIS and IR beams onto the catalyst surface for SFG vibrational spectroscopy. The catalyst was prepared on the back side of a sapphire window and consisted of a thin film of either SiO_2 or TiO_2 acting as a support for Pt nanoparticles.*

8.3.4 Density Functional Theory Calculations

The calculation is performed using the VASP code based on the density functional theory. For the exchange-correlation functional, the generalized gradient approximation (GGA) of Perdew-Burke-Ernzerhof (PBE) is used. The projector augmented-wave pseudopotentials are used with an energy cutoff of 400 eV for the plane-wave basis functions. To simulate the molecule absorption on the TiO_2 surfaces, a slab model is used with 6 Ti–O double layers (about 20 Angstrom thick) and 10 Angstrom vacuum layer, and a 1×2 supercell (about 10 Angstrom by 8 Angstrom) in the x-y plane. The Brillouin zone integration is carried out using 2×2×1 Monkhorst–Pack k-point meshes.

8.4 Results and Discussion

8.4.1 PVP Cap Blocks Strong Metal–Support Interactions

Although many reaction products exist for furfuraldehyde hydrogenation depending on the pressure and temperature conditions,[17] we observed only four products which we break into

two reaction pathways as shown in Scheme 1. The first pathway is decarbonylation to produce furan. Along this same pathway, furan can further hydrogenate to form tetrahydrofuran (THF) or further decarbonylate to form propylene.[27] The second reaction pathway is selective C=O bond hydrogenation to produce furfuryl alcohol.

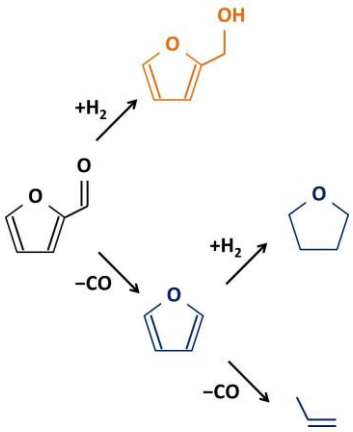

Scheme 1

Fig. 2 demonstrates that the Pt/TiO_2 interface plays a major role in the production of furfuryl alcohol. Each plot shows the formation of reaction products as a function of time. Parts A and B show the results for PVP-capped Pt nanoparticles supported on TiO_2 and SiO_2, respectively. The PVP-capped particles show identical catalytic activity regardless of the support, indicating that the presence of the PVP cap prevents actual contact between the Pt nanoparticles and the oxide support. Parts C and D show the results for the same catalysts following removal of the PVP cap by UV treatment. The cleaned nanoparticles on TiO_2 show a 50-fold enhancement in the production of furfuryl alcohol which we attribute to the contact between the Pt and TiO_2 following the removal of PVP. However, the cleaned nanoparticles on SiO_2 show similar activity and selectivity to the capped nanoparticles, indicating that the Pt/SiO_2 interface does not play an important role in this reaction.

8.4.2 PVP Cap Removal by UV Cleaning

Fig. 3A shows the C to Pt and the N to Pt atomic ratios of an LB film of nanoparticles as a function of UV treatment time measured by X-ray photoelectron spectroscopy (XPS). Both C and N signals decrease relative to the Pt signal with UV exposure, indicating that the PVP cap is being removed from the Pt nanoparticles. In this experiment the nanoparticles are supported on a doped Si wafer without any oxide layer to avoid charging during XPS measurements. The activity of the Pt nanoparticles increases by a factor of ~5 with UV treatment time as determined by ethylene hydrogenation, indicating that more Pt sites become available as the cap is removed. The number of active sites after UV cleaning does not vary between TiO_2 and SiO_2 showing that the UV cleaning does not depend on the nanoparticle support. Fig. 3B schematically depicts the effect of UV cleaning on the supported nanoparticles. As the PVP cap is removed, two important effects are observed: (1) the number of accessible Pt sites increases, so the activity of the catalyst for ethylene hydrogenation increases, and (2) the Pt nanoparticles come into contact with the oxide support. Electron microscopy shows that size and shape monodispersity of the

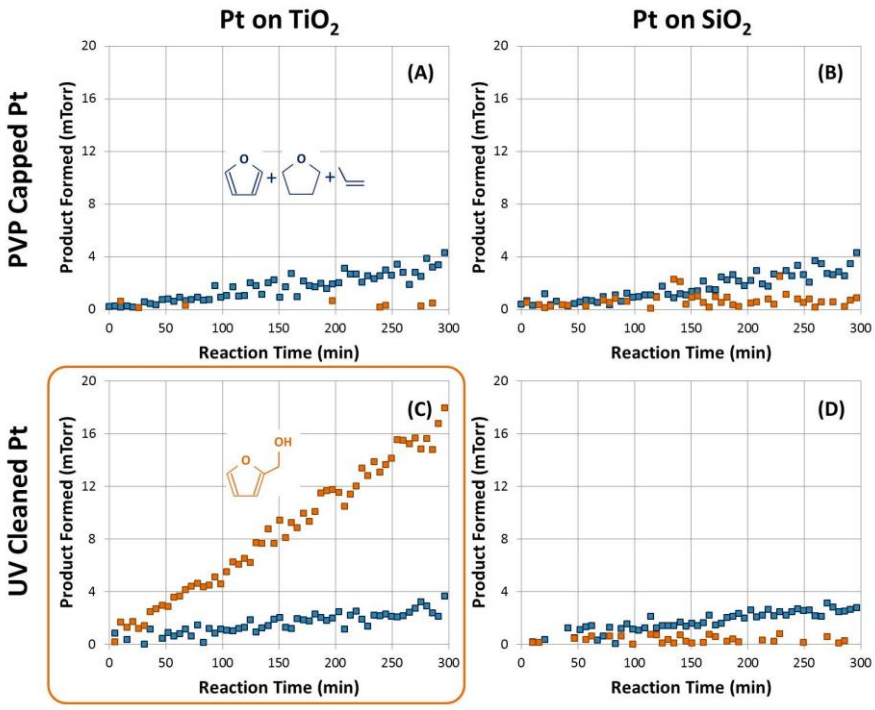

Fig. 2 *Formation of reaction products as a function of time on four Pt nanoparticle catalysts. Parts* **(A)** *and* **(B)** *show results for PVP-capped Pt nanoparticles supported on TiO_2 and SiO_2, respectively. Parts* **(C)** *and* **(D)** *show results for identical catalysts following 3 h UV cleaning to remove the PVP cap. Furfuryl alcohol is shown in orange, and decarbonylation products (i.e. furan, THF, and propylene) are shown in blue. The support has no effect on the activity or selectivity of the capped particles. However, following UV cleaning, the formation of furfuryl alcohol is selectively enhanced on the Pt/TiO_2 catalyst.*

UV-cleaned nanoparticles is lost during reaction because the uncapped nanoparticles are not as thermally stable as the PVP-capped nanoparticles.

8.4.3 Role of Pt/TiO_2 Interface on Reaction Kinetics and Selectivity

Fig. 4 shows TOF of furfuraldehyde to decarbonylation products (i.e. furan, THF, and propylene) and to furfuryl alcohol as a function of UV treatment time for Pt on TiO_2 (A) and SiO_2 (B). The activity of each catalyst is normalized to the number of active sites measured by ethylene hydrogenation. Initially, the PVP-capped Pt does not produce any furfuryl alcohol regardless of the support. However, as the Pt is brought into close interaction with the TiO_2 by UV cleaning, the activity for furfuryl alcohol production increases. Pt supported on SiO_2 does not produce any furfuryl alcohol outside of measurement error even after extensive UV cleaning. The data show that Pt activity for decarbonylation does not depend on the support, indicating that the oxide/metal interface has no effect on this reaction pathway.

Fig. 5 shows the selectivity of Pt supported on TiO_2 (A) and SiO_2 (B) as a function of UV treatment time. The selectivity of the Pt/TiO_2 catalyst for furfuryl alcohol increases with PVP removal, reaching ~90% after 180 min UV cleaning. This is a dramatic change in reaction selectivity changing from ~100% decarbonylation products on the capped nanoparticles to ~90%

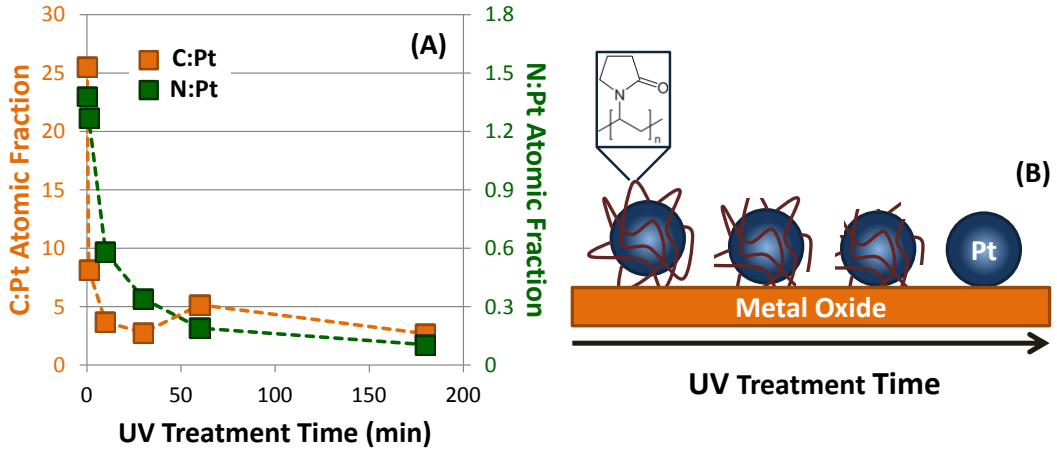

Fig. 3 (A) *C:Pt (orange) and N:Pt (green) atomic fractions for PVP-capped Pt nanoparticles as a function of UV cleaning time measured by XPS. Results indicate removal of the PVP cap from the Pt nanoparticles by UV photodecomposition.* **(B)** *Schematic showing the effects of UV cleaning on PVP-capped Pt nanoparticles. UV cleaning has two effects on the catalyst: (1) the number of available active sites per nanoparticle increases, and (2) the nanoparticles are brought into close contact with the support.*

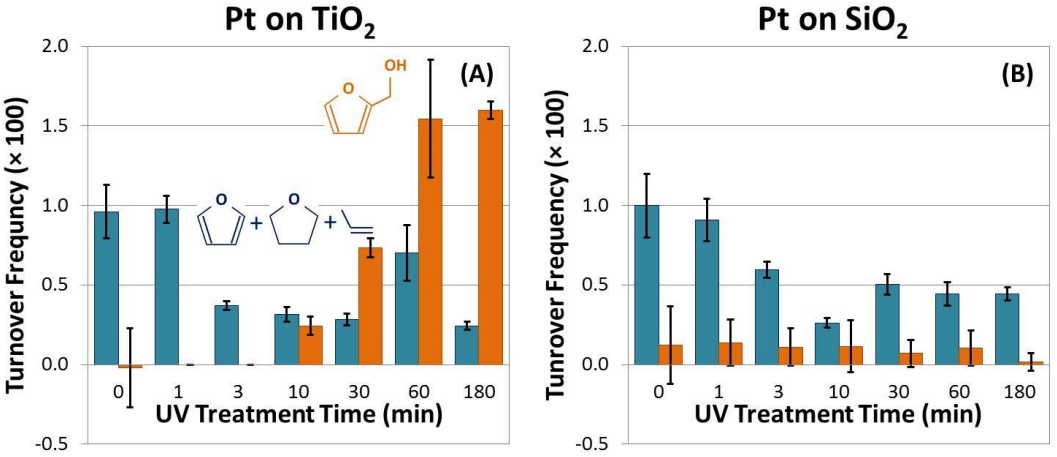

Fig. 4 *Turnover frequency (TOF) of furfuraldehyde by Pt supported on TiO_2* **(A)** *and on SiO_2* **(B)** *as a function of UV treatment time. Orange bars show the formation of furfuryl alcohol, representing selective C=O bond hydrogenation , and blue bars show the combined formation of furan, THF, and propylene, representing the decarbonylation pathway. All TOF values are normalized to the number of Pt actives sites measured by ethylene hydrogenation. Initially, no furfuryl alcohol is produced by Pt on either support. However, with UV cleaning, the formation of furfuryl alcohol is selectively enhanced on the Pt/TiO_2 catalyst.*

furfuryl alcohol on the cleaned nanoparticles. The Pt/SiO_2 catalyst shows no effect of PVP removal on the reaction selectivity and produces only decarbonylation products. These results suggest that the Pt/TiO_2 catalyst generates a unique reaction intermediate that is highly selective toward the formation of furfuryl alcohol. Below we demonstrate by SFG vibrational

spectroscopy that the production of furfuryl alcohol correlates with a furfuryl-oxy intermediate that forms on TiO_2, and this furfuryl-oxy intermediate is the selective precursor to furfuryl alcohol.

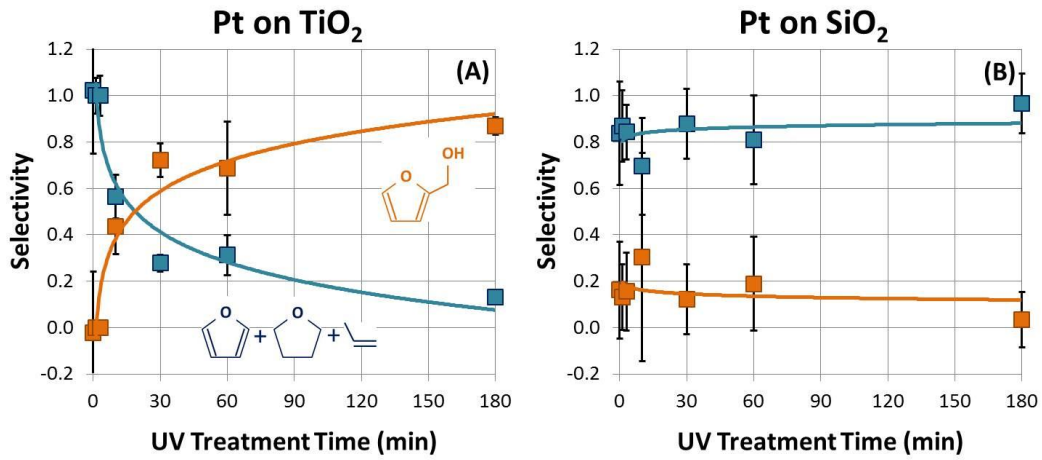

Fig. 5 *Selectivity for furfuraldehyde hydrogenation by Pt supported on TiO_2* **(A)** *and on SiO_2* **(B)** *as a function of UV treatment time. Furfuryl alcohol is shown in orange, and decarbonylation products (i.e. furan, THF, and propylene) are shown in blue. The selectivity of the Pt/TiO_2 catalyst changes dramatically with UV cleaning, going from 100% selectivity for decarbonylation products to ~90% selectivity for furfuryl alcohol. However, the Pt/SiO_2 catalyst is selective only for decarbonylation regardless of UV cleaning time.*

8.4.4 Probing Reaction Intermediates by SFG Vibrational Spectroscopy

Fig. 6 shows SFG spectra of Pt/SiO_2 (A), TiO_2 without Pt (B), and Pt/TiO_2 (C) under reaction conditions following 180 min UV cleaning. The Pt/SiO_2 catalyst shows an intense stretch at 3,030 cm^{-1}. This stretch is significantly lower frequency than the aromatic mode for the 5-membered furan ring which appears above 3,100 cm^{-1}, and it has been previously assigned in furan hydrogenation as a vinylic stretch.[27] This indicates the presence of an unsaturated furan ring with broken aromaticity. A loss of aromaticity can occur in two ways: The first is partial hydrogenation of the ring to dihydrofuran (DHF) as has been previously observed for furan hydrogenation on Pt single crystals.[27] The second is by an interaction of the furan ring with the catalyst surface via the O atom. In the present study, GC measurements confirm that no DHF forms on this catalyst which is 60% selective to furan, 20% selective to THF, and 20% selective to propylene. Consequently, we assign this vinylic stretch to a furan ring bound to the Pt surface via the O atom as depicted in Fig. 6A.

At lower temperatures we also observe a stretch at 2,765 cm^{-1} (not shown) indicative of the aldehyde C–H stretch. However, this stretch disappears upon heating to 393 K due to decarbonylation of the furfuraldehyde to furan. This process results in CO deposition on the Pt surface which acts as a poison in the subsequent hydrogenation of furan to DHF, THF, or butanol. This explains the relatively low activity of this reaction pathway in furfuraldehyde hydrogenation compared to previous results for furan hydrogenation where at these pressures and temperatures, THF and butanol would be major products.[27] An additional weak stretch appears

in Fig. 6A at 2860 cm^{-1}. We assign this stretch to the symmetric CH_3 mode from π-bonded propylene which is a 20% product on this catalyst.

Fig. 6B shows the spectrum of TiO_2 without Pt under reaction conditions. This spectrum shows two intense features. The first feature appears at 3,130 cm^{-1} and represents the aromatic stretch of the furan ring. The second feature is a located near 2,920 cm^{-1} and represents the CH_2 symmetric mode. This spectrum correlates with a furfuryl-oxy intermediate resulting from furfuraldehdye bonding to the TiO_2 via the carbonyl O atom followed by the addition of a single H atom to the carbonyl C. This furfuryl-oxy surface intermediate is shown schematically next to the spectrum in Fig. 6B and is the intermediate precursor to furfuryl alcohol formation. Although TiO_2 does not actively dissociate H_2, it is not surprising sufficient H atoms are present to produce a monolayer of furfuryl-oxy surface intermediates. This may be a result of slight H_2 dissociation at defect sites in the polycrystalline TiO_2 film, or the H atoms may come from hydroxyl groups that form on the TiO_2 surface in ambient or during UV cleaning. However, without a continual supply of H atoms from supported Pt nanoparticles, the TiO_2 substrate does not turnover.

Fig. 6C shows the spectrum of the Pt/TiO_2 catalyst during reaction. In contrast to the spectra obtained on Pt/SiO_2 and TiO_2 without Pt, the nonresonant background of the Pt/TiO_2 sample is quite high, and the resonant modes appear as negative features against the high background. This effect, which is common in SFG, is a result of the phase mismatch between the resonant and nonresonant contributions of the spectrum. In the Pt/SiO_2 sample and TiO_2 sample without Pt, the nonresonant contribution to the spectrum is low, so any phase mismatch is not noticeable. However, the nonresonant component of the Pt/TiO_2 catalyst is much greater resulting in destructive interference with the resonant vibrations. The enhanced nonresonant signal in the Pt/TiO_2 catalyst is a result of H spillover from the Pt resulting in a reduced TiO_2 support. It is well known that in TiO_2, O-vacancies act as electron donors into mid-gap states of the reduced oxide which results in a greatly enhanced surface conductivity.[32] Because the nonresonant contribution to an SFG spectrum is largely the result of free electron motion at the surface of the substrate, it is not surprising that increased TiO_2 conductivity by H_2 reduction results in a dramatic enhancement of the nonresonant signal. This effect is reversible in O_2 as shown in Fig. 7. Fig. 7 plots the magnitude of the nonresonant signal in alternating H_2 and O_2 atmospheres for several samples. An effect on the nonresonant signal intensity is only significant for the Pt/TiO_2 catalyst following UV cleaning. The same effect is not observed for the Pt/SiO_2 catalyst and is only weakly observed for the Pt–PVP/TiO_2 catalyst before cap removal. This reflects the non-reducible nature of SiO_2 as well as the necessity of removing the Pt capping agent to enable H spillover to the TiO_2.

The resonant components of the Pt/TiO_2 spectrum during reaction correlate closely with the features observed on the Pt/SiO_2 and the TiO_2 samples, and the Pt/TiO_2 spectrum appears to represent a combination of the spectrum on Pt and the spectrum on TiO_2 as shown in Fig 6C. This indicates that Pt has a similar reactivity when supported on either oxide, but that H spillover from Pt results in turnover of the furfuryl-oxy intermediate on TiO_2 to furfuryl alcohol. As shown above by kinetic measurements, this reaction pathway is ~10 times faster than the decarbonylation reaction pathway which occurs only on Pt. This result demonstrates a striking similarity between SMSI and acid–base catalysis where both processes begin by formation of a unique reaction intermediate that acts as a highly active intermediate in a selective reaction

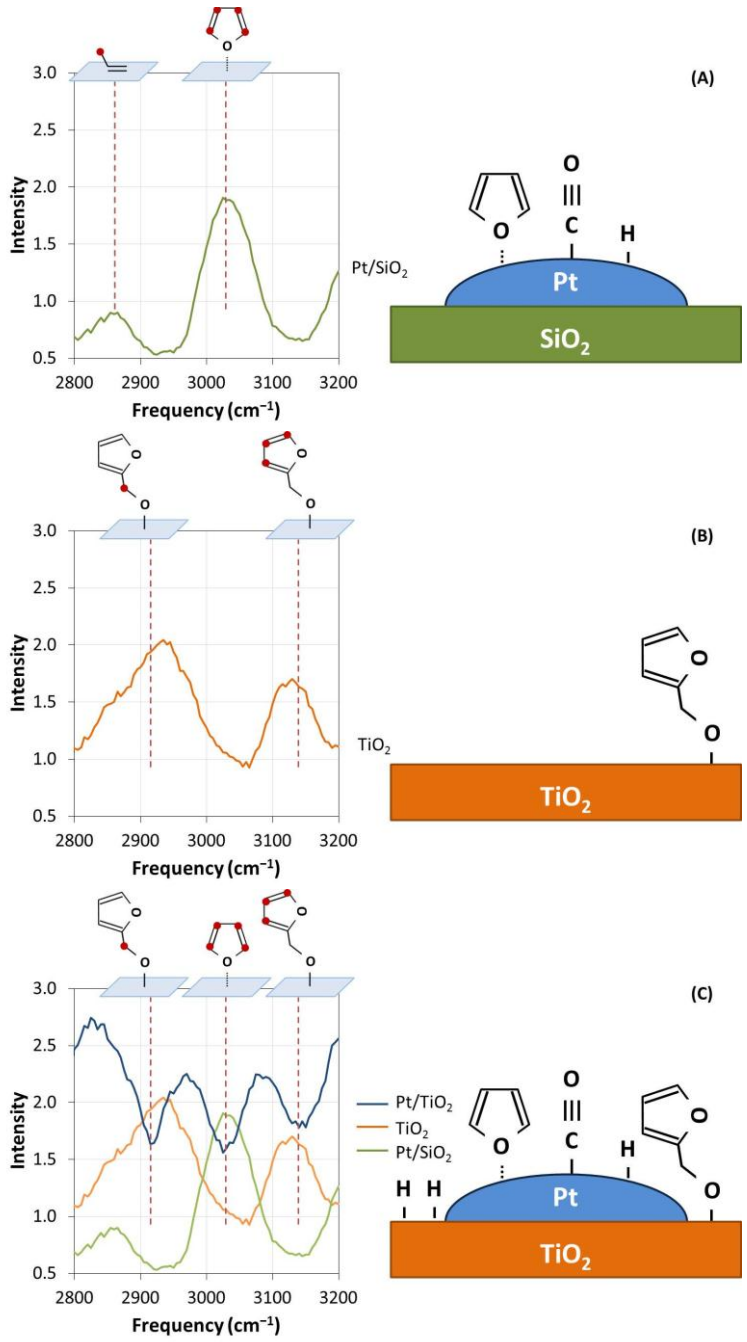

Fig. 6 *SFG spectra of Pt/SiO_2 catalyst* **(A)**, *TiO_2 support without Pt* **(B)**, *and Pt/TiO_2 catalyst* **(C)** *during reaction following 180 min UV treatment. Next to each spectrum a schematic depicts the surface intermediates represented in the spectrum, and red dots on the molecules above show the C–H bonds responsible for each vibrational mode*

pathway. In the case of SMSI, the TiO_2 support activates the furfuraldehyde molecule to form the highly selective furfuryl-oxy intermediate. The role of the crucial Pt/TiO_2 interface is simply to enable H spillover to this active intermediate.

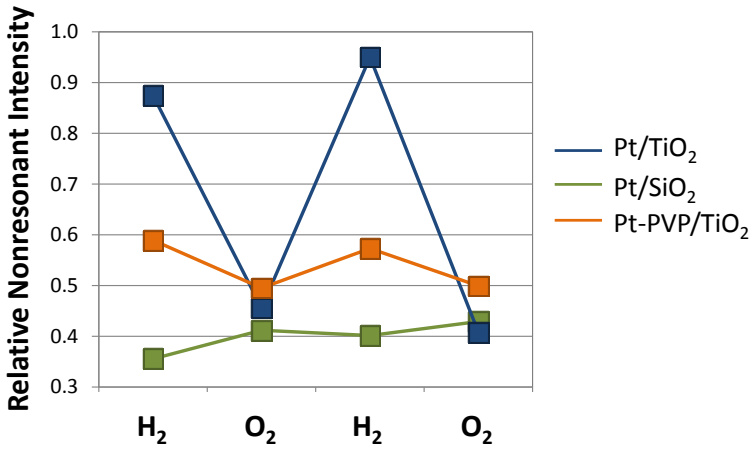

Fig. 7 *Relative nonresonant SFG intensity of a Pt/TiO_2 catalyst (blue), Pt/SiO_2 catalyst (green), and $Pt–PVP/TiO_2$ catalyst in alternating H_2 and O_2 environments (100 Torr) at 333 K. The Pt/TiO_2 and Pt/SiO_2 catalysts were UV-cleaned for 10 min (longer UV cleaning treatments do not change the results shown). The $Pt–PVP/TiO_2$ catalyst was not UV cleaned, so the PVP encapsulated the Pt nanoparticles and prevented contact between Pt and TiO_2. The nonresonant intensity is determined from the average intensity between 2,700 and 2,800 cm^{-1} where there are no resonant features. For the Pt/TiO_2 catalyst, the nonresonant background changes dramatically in H_2 and O_2. The enhanced nonresonant signal in H_2 is a result of H spillover from the Pt resulting in a reduced TiO_2 support, and this effect is reversible in O_2. The same effect is not observed for the Pt/SiO_2 catalyst and is only weakly observed for the $Pt–PVP/TiO_2$ catalyst before cap removal. This reflects the non-reducible nature of SiO_2 as well as the necessity of removing the PVP cap to enable H spillover from Pt to TiO_2.*

8.4.5 Charge Transfer from TiO_2 to Furfuraldehyde

Density functional theory (DFT) calculations indicate that O-vacancies on the reduced TiO_2 surface are the catalytically active sites. Furfuraldehyde binding on the [101] surface of anatase TiO_2 is discussed here; binding on other low-energy surfaces was considered with similar conclusions. When there is no O-vacancy on the surface, the calculations show that the furfuraldehyde molecule does not bind with either Ti cations or O anions on the surface. However, when there is an O-vacancy on the surface, furfuraldehyde binds to one of the two Ti cations closest to the vacancy site, as shown in Fig. 8, and the energy of the system decreases by 1.35 eV. The significant energy decrease associated with the binding can be understood considering that the Ti cations near the oxygen vacancy are in the reduced Ti^{3+} state, so one electron is occupying a high-energy mid-gap state near the conduction band. The binding of furfuraldehyde molecule oxidizes this cation to a Ti^{4+} state as one electron transfers to the furfuraldehyde molecule. The contour in Fig. 8 shows the charge transfer during the binding process. The electron transfers from the area around the Ti^{3+} cation (shown by green contour) to the C=O bond (shown by blue contour). As a new Ti–O bond is formed, the original C=O double bond is changed into a C–O σ bond.

In the final surface binding state, the O atom in the furfuraldehyde molecule is coordinated by Ti and C and is in a stable full-shell state. However, the negative charge

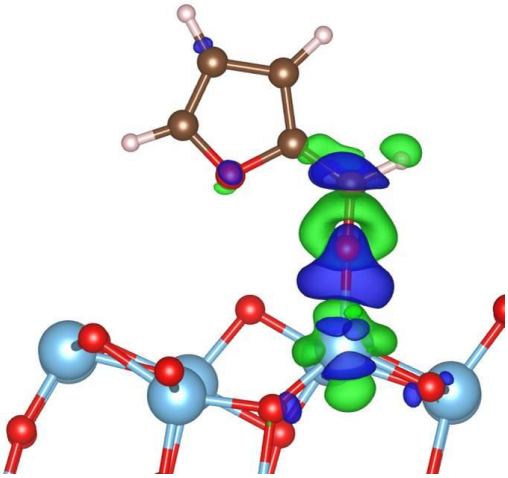

Fig. 8 *The structure plot of a furfuraldehyde molecule binding to a Ti cation at an O-vacancy site on anatase TiO_2, and the charge transfer induced by the surface binding interaction. The filled cyan, red, brown and white circles show the Ti, O, C and H atoms, respectively. The hollow green circles show the site of the O-vacancy (without the vacancy, there should be two O atoms inside the circle). The green contour shows the electron charge loss, and the blue contour shows the electron charge gain induced by the surface binding. In this charge transfer interaction, the Ti atom changes from a 3+ to a 4+ oxidation state, and the furfuraldehyde molecule acquires a negative charge. This negative charge localizes around the carbonyl C, activating it for H addition.*

localized around the C atom represents a dangling bond, which is very reactive for H binding. A direct calculation shows the energy decreases by 0.2 eV when one H atom leaves the Pt surface and binds with this reactive C atom. Consequently, this step is fast and results in the steady state coverage of furfuryl-oxy intermediates on TiO_2 observed by SFG. This model of furfuraldehyde activation at O-vacancy sites in TiO_2 is also consistent with the experimental data showing that SMSI activity correlates with H spillover which occurs only for the UV-cleaned Pt/TiO_2 catalyst. However, in the case of a free furfuraldehyde molecule (not bound to the TiO_2 surface), there is an energy cost of 2.3 eV for a H atom from the Pt surface to bind to the carbonyl C of a furfuraldehyde molecule. Obviously, this is impossible from a thermodynamic point of view. Furthermore, the calculations show that furfuraldehyde does not bind with a SiO_2 surface. This is in accordance with the experimental observation that the Pt/SiO_2 catalyst is not SMSI active.

8.5 Conclusions

For furfuraldehyde hydrogenation on supported Pt, the oxide support plays a major role to determine the activity and selectivity of the catalyst. This effect, which is common to many reactions, is often referred to as a strong metal–support interaction, but a molecular-level understanding has been lacking notwithstanding the obvious scientific and practical importance. We demonstrate that when Pt nanoparticles make close contact with a TiO_2 support, the Pt/TiO_2 interface results in a new reaction pathway that is highly selective toward furfuryl alcohol formation. SFG vibrational spectroscopy shows that a furfuryl-oxy intermediate forms on TiO_2 and is the selective precursor to furfuryl alcohol. The role of the Pt/TiO_2 interface is simply to enable H spillover to this active intermediate, and this reaction pathway is ~10 faster than the

reaction rate on Pt alone. DFT calculations suggest that the formation of the active furfuryl-oxy intermediate is the result of a charge transfer interaction between the furfuraldehyde molecule and an O-vacancy site on the TiO_2 surface. In this charge transfer interaction, the furfuraldehyde molecule acquires a negative charge that localizes around the carbonyl C, activating it for H addition. These results provide a detailed picture of the molecular and electronic interactions that combine to create the SMSI phenomenon and demonstrate that acid–base interactions are the foundation for highly selective catalysis at the oxide–metal interface.

8.6 References

(1) Schwab, G. M. *Transactions of the Faraday Society* **1946**, *42*, 689.

(2) Tauster, S. J.; Fung, S. C.; Garten, R. L. *Journal of the American Chemical Society* **1978**, *100*, 170.

(3) Tauster, S. J.; Fung, S. C.; Baker, R. T. K.; Horsley, J. A. *Science* **1981**, *211*, 1121.

(4) Tauster, S. J. *Accounts of Chemical Research* **1987**, *20*, 389.

(5) Oh, S. H.; Eickel, C. C. *Journal of Catalysis* **1988**, *112*, 543.

(6) Zhu, H.; Qin, Z.; Shan, W.; Shen, W.; Wang, J. *Journal of Catalysis* **2004**, *225*, 267.

(7) Chen, M. S.; Goodman, D. W. *Science* **2004**, *306*, 252.

(8) Goodman, D. *Catalysis Letters* **2005**, *99*, 1.

(9) Baker, L. R.; Hervier, A.; Seo, H.; Kennedy, G.; Komvopoulos, K.; Somorjai, G. A. *The Journal of Physical Chemistry C* **2011**, *115*, 16006.

(10) Boffa, A. B.; Bell, A. T.; Somorjai, G. A. *Journal of Catalysis* **1993**, *139*, 602.

(11) Boffa, A.; Lin, C.; Bell, A. T.; Somorjai, G. A. *Journal of Catalysis* **1994**, *149*, 149.

(12) Yamada, Y.; Tsung, C.-K.; Huang, W.; Huo, Z.; Habas, S. E.; Soejima, T.; Aliaga, C. E.; Somorjai, G. A.; Yang, P. *Nat Chem* **2011**, *3*, 372.

(13) Vannice, M. A.; Sen, B. *Journal of Catalysis* **1989**, *115*, 65.

(14) Lin, S. D.; Sanders, D. K.; Albert Vannice, M. *Applied Catalysis A: General* **1994**, *113*, 59.

(15) Kijeński, J.; Winiarek, P. *Applied Catalysis A: General* **2000**, *193*, L1.

(16) Malathi, R.; Viswanath, R. P. *Applied Catalysis A: General* **2001**, *208*, 323.

(17) Kijeński, J.; Winiarek, P.; Paryjczak, T.; Lewicki, A.; Mikołajska, A. *Applied Catalysis A: General* **2002**, *233*, 171.

(18) Bracey, J. D.; Burch, R. *Journal of Catalysis* **1984**, *86*, 384.

(19) Sachtler, W. M. H.; Shriver, D. F.; Hollenberg, W. B.; Lang, A. F. *Journal of Catalysis* **1985**, *92*, 429.

(20) Sachtler, W. M. H.; Ichikawa, M. *The Journal of Physical Chemistry* **1986**, *90*, 4752.

(21) Jencks, W. P. *Accounts of Chemical Research* **1980**, *13*, 161.

(22) Greeley, J.; Norskov, J. K.; Mavrikakis, M. *Annu. Rev. Phys. Chem.* **2002**, *53*, 319.

(23) Olah, G. A.; Molnar, A. *Hydrocarbon Chemistry*; 2nd Edition ed.; John Wiley & Sons, Inc.: Hoboken, NJ, 2003.

(24) Bratlie, K. M.; Kliewer, C. J.; Somorjai, G. A. *The Journal of Physical Chemistry B* **2006**, *110*, 17925.

(25) Bratlie, K. M.; Komvopoulos, K.; Somorjai, G. A. *The Journal of Physical Chemistry C* **2008**, *112*, 11865.

(26) Kliewer, C. J.; Bieri, M.; Somorjai, G. A. *Journal of the American Chemical Society* **2009**, *131*, 9958.

(27) Kliewer, C. J.; Aliaga, C.; Bieri, M.; Huang, W.; Tsung, C.-K.; Wood, J. B.; Komvopoulos, K.; Somorjai, G. A. *Journal of the American Chemical Society* **2010**, *132*, 13088.

(28) Aliaga, C.; Park, J. Y.; Yamada, Y.; Lee, H. S.; Tsung, C.-K.; Yang, P.; Somorjai, G. A. *The Journal of Physical Chemistry C* **2009**, *113*, 6150.

(29) Song, H.; Kim, F.; Connor, S.; Somorjai, G. A.; Yang, P. *The Journal of Physical Chemistry B* **2004**, *109*, 188.

(30) Schlatter, J. C.; Boudart, M. *Journal of Catalysis* **1972**, *24*, 482.

(31) Kuhn, J. N.; Tsung, C.-K.; Huang, W.; Somorjai, G. A. *Journal of Catalysis* **2009**, *265*, 209.

(32) Seo, H.; Baker, L. R.; Hervier, A.; Kim, J.; Whitten, J. L.; Somorjai, G. A. *Nano Letters* **2010**, *11*, 751.

Chapter 9

The Role of an Organic Cap in Nanoparticle Catalysis: Restructuring of Carbonaceous Material Controls Catalytic Activity of Platinum Nanoparticles

9.1 Abstract

Inherent in the colloidal synthesis of nanoparticle catalysts is the presence of an organic capping agent that encapsulates the nanoparticles to prevent aggregation. However, this capping agent often remains present on the nanoparticles during catalytic reaction, and the effect of the cap on catalysis is an important question that will influence the future applications of colloidal nanoparticles. In this study, the structure of poly(vinylpyrrolidone) (PVP) ligands on Pt nanoparticles is probed using sum frequency generation (SFG) vibrational spectroscopy. While the PVP polymer is initially rigid, when the PVP is removed by UV light, carbonaceous fragments are found on the surface that dynamically restructure in H_2 and O_2. These fragments form a porous coating around the Pt in H_2 but collapse to a tightly closed shell in O_2. Using ethylene hydrogenation and methanol oxidation as a probe for the catalytic activity of the nanoparticles in H_2 and O_2, respectively, it is shown that the structure of these carbonaceous fragments controls the catalytic activity of the nanoparticles across several orders of magnitude. Kinetic experiments on thermally-cleaned PVP-capped and oleic acid-capped nanoparticles show that these findings apply to multiple capping agents and cleaning methods. This work highlights the dominant role of an organic cap to mediate nanoparticle catalysis and provides one example where capped nanoparticles are dramatically better catalysts than their uncapped analogues.

9.2 Introduction

Traditional methods for catalyst preparation (i.e. incipient wetness and ion exchange) use the reduction of a metal salt inside of a mesoporous oxide.[1,2] The result is a high surface area catalyst consisting of metal particles with a broad distribution of sizes and morphologies. This type of polydisperse heterogeneous catalyst masks the structure sensitivity inherent in heterogeneous catalysis[3-6] because of the impossibility of selecting nanoparticles of a single size or shape. Recent advances in nanoscience have shown that colloidal synthetic methods can produce monodisperse nanoparticles with well-defined sizes and shapes.[7-11] This advance marked a new era in heterogeneous catalysis where monodisperse nanoparticles serve as model catalysts,[12-14] and these catalysts have shown that size and shape control the catalytic activity and selectivity for many reactions.[15-21] These results indicate that colloidal nanoscience is an important tool for the development of new highly selective catalysts necessary to minimize the environmental impact and improve the economic efficiency of numerous commercial chemical processes.

In colloidal synthetic methods, nanoparticles are necessarily encapsulated in an organic polymer or surfactant. This organic capping agent lowers the surface energy of the nanoparticle to prevent aggregation of the particles;[11] the cap may also help to control the size and shape of the nanoparticles.[22] This gives rise to an important question regarding the effect of the organic cap on the catalytic properties of the nanoparticles. It is traditionally thought that the cap acts as a site blocking agent and lowers the metal surface area available for catalytic reaction.[23] In this light, it has been assumed that colloidal preparation methods are impractical for commercial catalytic applications because the presence of the capping agent decreases the apparent metal dispersion. However, this is an incomplete assumption based on a model that considers the cap as a passive coating rather than a dynamic shell that can adjust under reaction conditions. It has been observed in the case of Pt–dendrimer complexes that the dendrimer structure, which is highly sensitive to gas/liquid conditions, controls access to the Pt surface.[24] Although the dendrimer blocks the Pt surface in air, it adopts an open structure in water that allows ready access of gasses to the Pt surface. Despite the importance of this effect for nanoparticle catalysis, little effort has been made to directly probe the role of the nanoparticle cap to mediate surface adsorption and catalytic activity. The lack of activity in this area is largely due to the predetermination that an organic cap necessarily hinders nanoparticle catalysis.

Because of the high surface energy of metals, it is impossible to maintain a clean metal surface, even under conditions of ultra-high vacuum. With this in mind, it is clear that even catalysts prepared by traditional methods also become "capped" with undefined surface species as these catalysts quickly become contaminated in ambient conditions or during reaction.[25] Accordingly, the capping agents of colloidal nanoparticles may be desirable because they represent a well-controlled passivation layer which, if carefully selected, may not prevent catalysis under reaction conditions. This concept is also reminiscent of homogeneous catalysis where ligands are used to tune the activity and selectivity of single metal ions,[26] and several examples demonstrate that similar effects are possible on metal clusters and nanoparticles.[27,28]

The present work investigates the role of poly(vinylpyrrolidone) (PVP) to mediate the catalytic properties of encapsulated Pt nanoparticles. We probe the molecular structure of the PVP cap by sum frequency generations (SFG) vibrational spectroscopy. Ethylene hydrogenation and methanol oxidation serve as model reactions to probe the catalytic activity in reducing and oxidizing conditions, respectively. The results show that the PVP cap is sterically rigid and maintains a constant structure regardless of gas environment. However, when the PVP is removed by photodecomposition using UV light, carbonaceous fragments are found on the surface that reversibly restructure in H_2 and O_2. In O_2 atmosphere, these carbonaceous fragments form a tightly closed shell around the nanoparticles that blocks catalytic activity, but this shell opens in H_2. As a result, the PVP-capped nanoparticles are more than 10 times more active for methanol oxidation than their cleaned analogues, while the UV-cleaned nanoparticles are more than 10 times more active for ethylene hydrogenation. Kinetic experiments on thermally-cleaned PVP-capped and oleic acid (OA)-capped nanoparticles show similar results indicating that these findings apply to multiple capping agents and cleaning methods. This work highlights the dominant role of organic material (controlled or otherwise) to mediate nanoparticle catalysis and provides one example where capped nanoparticles are dramatically better catalysts than their cleaned analogues.

9.3 Experimental

9.3.1 Nanoparticle Synthesis

The Pt nanoparticles were synthesized from chloroplatinic acid hexahydrate and PVP in a 1:4 mass ratio. In a small beaker, 110 mg of chlorplatinic acid was dissolved in 10 mL ethylene glycol. In a separate beaker, 440 mg of PVP was dissolved in 10 mL of ethylene glycol. Once in solution, the two mixtures were combined into a 50 mL two-neck round bottom flask fitted with an argon flow. The solution was purged under vacuum for 15 min. The vessel was then heated to 438 K for 1 h with vigorous mixing under a flow of argon. The resulting nanoparticles were precipitated with acetone and washed three times with ethanol and hexanes. The nanoparticles were then suspended in chloroform. Transmission electron microscopy (TEM) showed that the particles were 4.6 ± 2.8 nm.

To investigate the effect of different capping agents and cleaning methods on reaction kinetics, Pt nanoparticles were synthesized using an alternate method where the capping agent is added after synthesis. This allowed us to add different capping agents to identical nanoparticle aliquots to isolate the cap as the sole variable between two nanoparticle samples.[23] In a small beaker, 350 mg of chloroplatinic acid was dissolved in 17.5 mL ethylene glycol. In a separate beaker, 350 mg of NaOH was dissolved in 17.5 mL ethylene glycol. Once in solution, the two mixtures were combined in a 50 mL two-neck flask fitted with an argon flow. The solution was purged under vacuum for 15 min. The vessel was then heated to 433 K for 3 h with vigorous mixing under a flow of argon. Aliquots (2 mL) of the resulting nanoparticles were precipitated with 2 M HCl, and then re-dispersed in 2 mL ethanol containing 10 mg of either PVP or OA. TEM showed that the particles were 1.7 ± 0.8 nm.

9.3.2 Langmuir Blodgett Deposition

Formation of 2-dimensional films of monodisperse nanoparticles to serve as model catalysts is routinely achieved by Langmuir Blodgett deposition. This technique has been described previously in detail.[12,29] In short, a suspension of nanoparticles in chloroform is dispersed onto a water surface (18 MΩ). Time is given for the chloroform to evaporate, leaving a 2-dimensional dispersion of nanoparticles on the water surface. The film is then compressed with a mobile barrier, and the surface pressure is monitored as a function of decreasing surface area. The surface pressure corresponds to the density of nanoparticles on the water. When the desired surface pressure is reached, a substrate is pulled out from under the surface of the water, and the film of nanoparticles is deposited onto the substrate. The final density of nanoparticles on the substrate can be controlled by controlling the surface pressure during deposition. A surface pressure of 14 mN/m was used for these studies, and films were deposited using a Nima 611 LB trough. Filter paper served as the surface tension probe.

The substrate used to support the nanoparticles was a TiO_2 thin film (50 nm) deposited on a Si(100) wafer with a thermally grown SiO_2 layer (500 nm). The TiO_2 thin film was deposited on the SiO_2/Si wafer by electron beam evaporation from an oxide source without any substrate heating. Following deposition, the TiO_2 thin film was annealed at 773 K in O_2 to increase crystallinity and ensure a fully oxidized stoichiometry. Analogous samples were prepared for sum frequency generation spectroscopic studies. For these samples, an optically transparent

substrate was needed. A sapphire window rather than a Si wafer served as the substrate. A TiO_2 thin film (50 nm) was deposited on the sapphire window by electron beam evaporation, again followed by annealing at 773 K in O_2. The LB technique was then used to deposit a monolayer of the Pt nanoparticles onto the TiO_2 thin films. Electron microscopy showed that the area coverage for Pt on the substrate following LB was 30–50%. In some cases, TiO_2 used as a Pt support plays an active role in the catalytic chemistry. However, the conclusions reported here are not substrate dependent, and kinetic results have been obtained for identical nanoparticles supported on SiO_2 substrates, and no significant differences were observed.

LB deposition is challenging for OA-capped Pt nanoparticles owing to the high hydrophobicity of the OA. Consequently, for investigating the role of different capping agents, drop cast films of nanoparticles on a TiO_2 substrate were used as catalysts for both the PVP- and OA-capped samples.

9.3.3 UV Cleaning

Immediately prior to reaction, the samples were exposed to UV light in air to remove the PVP capping layer. Two low-pressure mercury (Hg) lamps (Lights Sources Inc., model number GPH357T5VH/4P) were used as the UV source; the Hg lamp emitted two lines at 184 and 254 nm. The two lamps were aligned parallel to each other 2.5 cm apart in a clean Al box. The sample sat 1.2 cm below the lamps. By varying the time of UV exposure, it was possible to control the amount of PVP removed from the Pt nanoparticles. This cleaning is the combined effect of direct photodecomposition of the PVP and oxidation of the PVP by ozone produced from the 184 nm Hg line.[30]

X-ray photoelectron spectroscopy (XPS) was used to observe the removal of PVP from the Pt nanoparticles after UV cleaning. Spectra were obtained using a Physical Electronics system (PHI 5400 ESCA/XPS) with an Al anode source. The analyzer was positioned at 50° relative to sample normal. The C 1s, N 1s, and Pt 4f peak areas were fit and normalized by the appropriate sensitivity factors to obtain the surface C:Pt and N:Pt atomic fractions as a function of UV exposure time. Measurements showed that 90% of the C was removed from the Pt following 3 h UV exposure.

Thermal cleaning in air was used as an alternative to UV cleaning for drop cast samples. For thermal cleaning, the samples were placed in a tube furnace and heated to a desired temperature for 16 h. The PVP- and OA-capped samples were treated at 473 and 573 K, respectively to remove the two capping agents that show different thermal stabilities.

9.3.4 Sum Frequency Generation Vibrational Spectroscopy

Sum frequency generation (SFG) is a second order, nonlinear process that probes the $X^{(2)}$ tensor. Because $X^{(2)}$ is zero for centrosymmetric media, SFG is only sensitive to a break in inversion symmetry which usually occurs at a surface or interface.[31] Consequently, SFG is useful for obtaining vibrational spectra of surfaces. In this study, SFG is used to obtain the vibrational spectrum of the nanoparticle capping layer in H_2 and O_2 atmospheres.

For SFG experiments, an active/passive mode-locked Nd:YAG laser (Leopard D-20, Continuum) produced a 20 ps pulse at a 20 Hz repetition rate. The fundamental output at 1064

nm was passed through an optical parametric generator/amplifier to generate a tunable infrared (IR) beam (2700–3600 cm^{-1}) and a second harmonic visible (VIS) beam (532 nm). The IR (100 μJ) and VIS (100 μJ) beams were spatially and temporally overlapped on the back surface of a sapphire window containing the Pt nanoparticles. The VIS and IR beams were incident on the sample at 40° and 50° degrees, respectively, relative to surface normal. The generated SFG signal was then collected and sent to a photomultiplier tube. A gated integrator was used to enhance the signal-to-noise. To collect a spectrum, the IR beam was scanned across the spectral range of interest. All experiments were performed in the ppp polarization combination.

The beams were directed onto the sample using a sapphire prism. A solution of deuterated polystyrene (d8) in deuterated decalin (d18) served as an index matching liquid between the prism and substrate that did not interfere with transmission of the IR beam at the C-H stretch frequency. The catalyst surface was pressed into thermal contact with an aluminum heating block to heat the catalyst to the desired temperature. A recess in the heating block allowed for the flow of gasses across the catalyst surface. A metal bellows circulation pump provided gas mixing. A gas tight seal was made between the sapphire window and the heating block using a Kalrez O-ring.

9.3.5 Kinetic Measurements

A stainless steel batch mode reactor was used to determine the reaction rates for ethylene hydrogenation and methanol oxidation on the Pt nanoparticle catalysts before and after UV cleaning. The catalyst temperature was controlled with a boron nitride substrate heater. A metal bellows circulation pump provided gas mixing. For ethylene hydrogenation, gas pressures were 10 Torr ethylene and 100 Torr H_2 in a background of He, and the catalyst temperature was 298 K. For methanol oxidation, gas pressures were 10 Torr methanol and 50 Torr O_2 in a background of He, and the catalyst temperature was 333 K. The methanol was purified by freeze-pump-thawing cycles. Each catalyst was tested for 2 h, and reaction products were monitored as a function of time using a gas chromatograph with a thermal conductivity detector.

9.4 Results and Discussion

Fig. 1A shows the SFG spectra of PVP-capped Pt nanoparticles in sequential gas environments. As the gas environment is initially cycled between H_2 and O_2, the SFG signal is higher in O_2 and decreases in H_2 corresponding to a structural reconfiguration of PVP on the Pt. Because of selection rules, SFG is sensitive not only to the individual molecular susceptibilities, but also to the net susceptibility of the entire ensemble of molecules at an interface. This net susceptibility depends strongly on the relative orientation of molecules at the interface. It is usually assumed that systems showing greater SFG signal intensity have a more highly ordered interface than those showing weaker intensity because a net disorder leads to canceling out of signal from individual molecular oscillators. Accordingly, we assign the loss of signal intensity going from O_2 to H_2 atmosphere as H_2-induced disordering of the PVP. However, after the first H_2/O_2 cycle, the PVP settles into a relatively stable configuration on the Pt, and minimal restructuring occurs as the gas environment continues to change between reducing and oxidizing conditions.

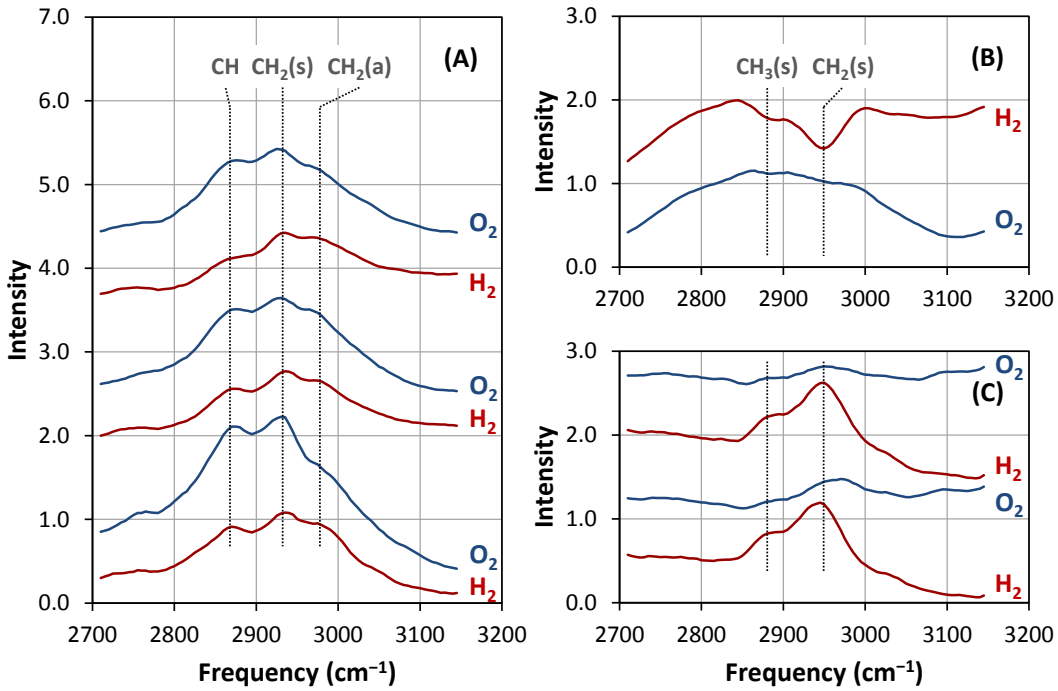

Fig. 1 *SFG spectra of the PVP-capped Pt nanoparticles before UV cleaning* **(A)** *and after UV cleaning for 10 min* (**B** *and* **C**)**.** *Spectra were obtained in 100 Torr of H_2 or O_2 in a background of Ar at 60 °C. A boxcar average over 5 data points improved signal-to-noise. In* **(A)** *and* **(C)** *the spectra are arbitrarily offset for clarity and were obtained sequentially from bottom to top.* **(B)** *shows the raw spectra with no offset of UV-cleaned nanoparticles first in H_2 then in O_2. The spectrum obtained in H_2 shows a much higher nonresonant intensity with resonant features appearing as dips in the high background. This is a result of the phase mismatch between the resonant and nonresonant contributions of the spectrum. By subtracting the raw spectra from a baseline obtained in Ar, the negative features are inverted to appear positive for clarity (shown in* **C***). Analysis of the resonant features in these spectra shows that before UV cleaning the PVP has a conformation that does not significantly change depending on the gas environment. However, following UV cleaning, carbonaceous fragments are found on the surface that are dynamic and reversibly restructure in H_2 and O_2.*

This is in strong contrast to spectra shown on identical nanoparticles following UV cleaning to remove PVP from the Pt surface. Fig. 1B shows the raw spectra of UV-cleaned nanoparticles first in H_2 then in O_2. The spectrum obtained in H_2 shows a much higher nonresonant intensity with resonant features appearing as negative peaks against the high background. This effect, which is common in SFG, is a result of the phase mismatch between the resonant and nonresonant contributions of the spectrum. By subtracting the raw spectra from a baseline obtained in Ar, the negative features are inverted to appear positive for clarity (see Fig. 1C). The enhanced nonresonant signal of the UV-cleaned catalyst is a result of H spillover from the Pt resulting in a reduced TiO_2 support, and the effect is completely reversible in O_2. In the PVP-capped sample, the nonresonant contribution to the spectrum is low even in H_2 because the PVP blocks H spillover to the TiO_2.

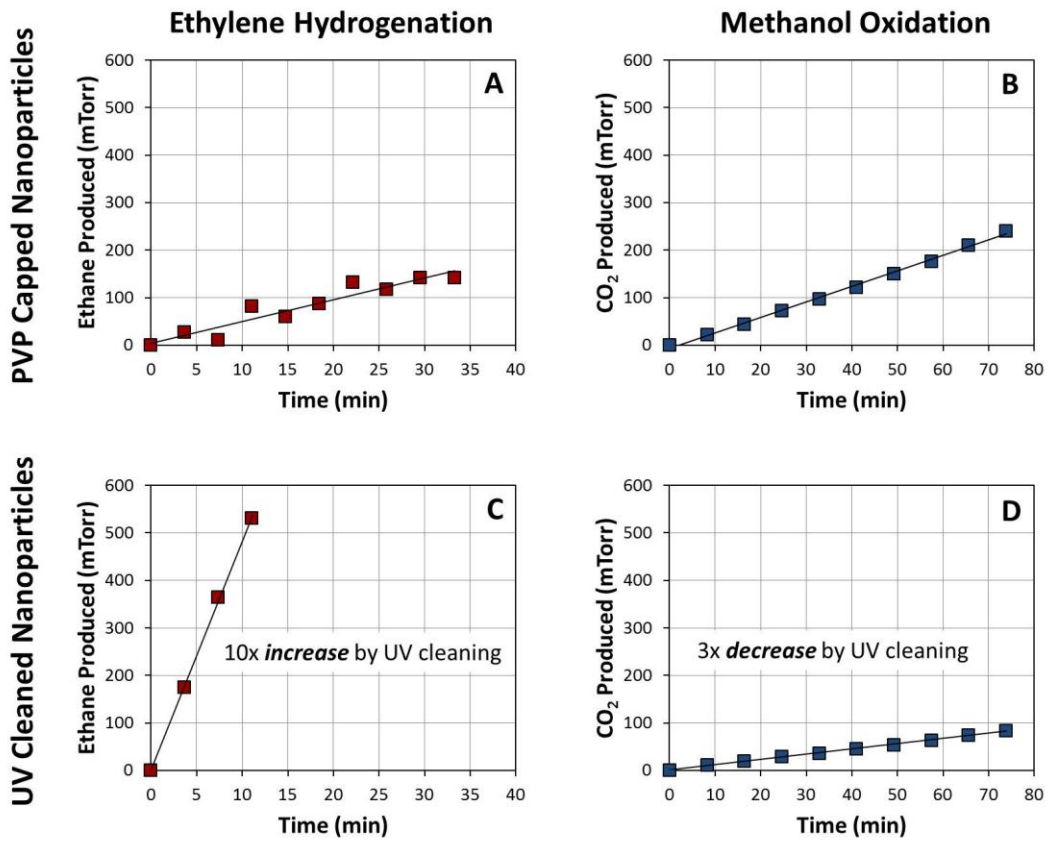

Fig. 2 *Formation of reaction products as a function of time on the Pt nanoparticles for ethylene hydrogenation and methanol oxidation before UV cleaning (***A** *and* **B***) and after UV cleaning for 10 min (***C** *and* **D).** *These results show that UV cleaning has a diverging effect on the rates of ethylene hydrogenation which increases by a factor of 10 and methanol oxidation which decreases by a factor of 3. Only CO_2 production is shown for methanol oxidation. However, formaldehyde was also produced as a minor product before and after UV cleaning.*

Fig. 1C shows that as the atmosphere is cycled between H_2 and O_2, carbonaceous fragments are present on the Pt surface, and these fragments reversibly restructure, adopting a structure that is strongly SFG active in H_2, and a structure which is almost entirely SFG inactive in O_2. It may be tempting to conclude that O_2 reacts with the remaining cap on the Pt surface to catalyze its complete removal. However, this is not the case as can be seen by the reversible appearance of the molecular vibrations when H_2 is re-introduced to the system. This change occurs reversibly over multiple cycles with no sign of signal decrease over time that would suggest eventual removal of the carbonaceous fragments.

It is also evident that the vibrational modes observed following UV cleaning are not the same as those observed from the intact PVP cap. Initially the vibrational modes observed on PVP-capped Pt (see Fig. 1A) match closely the assignments previously reported by infrared and Raman for PVP-Pt complexes.[32] Following UV cleaning, the peaks observed are attributable to CH_2 and CH_3 symmetric stretching modes outside of a 5-membered ring. It is also important to note that XPS measurements indicate that the surface C has decreased more than 85% compared

to the fully-capped nanoparticles following UV cleaning. It is not definitive whether the carbonaceous fragments observed by SFG after cleaning are photodecomposition products of PVP, or if they represent contamination of the UV-cleaned Pt surface, which would be unavoidable in ambient. However, it is clear that additional UV cleaning does little to remove these species.

Fig. 2 shows the catalytic activity of the Pt nanoparticles for ethylene hydrogenation and for methanol oxidation before and after UV cleaning. We selected these two reactions because they operate at low temperature (i.e., 298 K and 333 K, respectively) and allowed us to observe the effects of the cap structure on the catalytic activity of the nanoparticles in H_2 and O_2 atmospheres. The PVP-capped Pt nanoparticles are active for both reactions as shown in Fig. 2A and B. However, following UV cleaning, the activity of the nanoparticles for ethylene hydrogenation and methanol oxidation diverge. Fig. 2C and D show that following UV cleaning, the rate of ethylene hydrogenation increases by a factor of 10 while the rate of methanol oxidation decreases by a factor of 3. This represents a 30-fold divergence on the effect of UV cleaning for these two reactions.

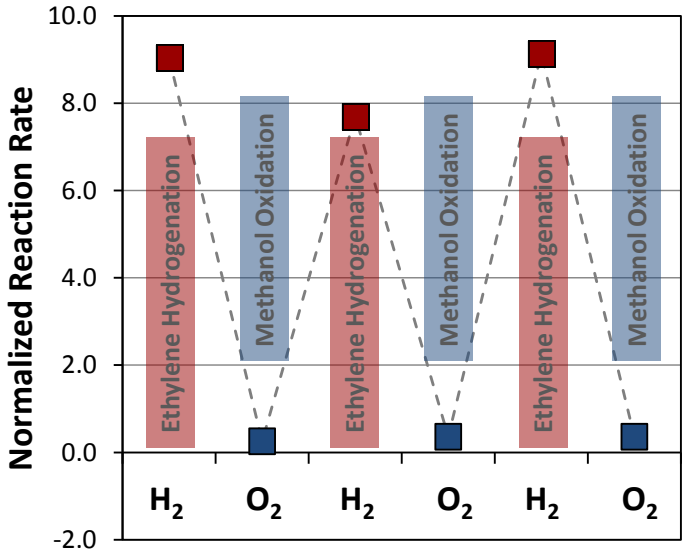

Fig. 3 *The reaction rates for ethylene hydrogenation and methanol oxidation on a single catalyst following UV cleaning for 10 min. The reaction rates are normalized to the initial rate for each reaction before UV cleaning. The results show that the diverging effect of UV cleaning on the two reactions is reversible and appears to correlate with the restructuring of carbonaceous fragments on the Pt surface observed by SFG.*

Fig. 3 shows the activity of the catalyst following UV cleaning where the catalyst is cycled several times between ethylene hydrogenation and methanol oxidation. The rates are normalized to the initial rate for each reaction prior to UV cleaning. It can be seen that the rates for both reactions are reversibly affected by the removal of the PVP cap. In the case of ethylene hydrogenation, this is easily understood based on the increased number of Pt sites available following PVP removal. In the case of methanol oxidation, it is surprising that cap removal would have a negative effect on the catalytic activity. It appears that the structure of the

carbonaceous fragments observed on the Pt following UV cleaning controls the catalytic properties of the uncapped nanoparticles. We suggest that these carbonaceous fragments which do little to prevent access to the Pt in H_2 atmosphere, collapse to a tightly closed shell around the Pt in O_2 atmosphere.

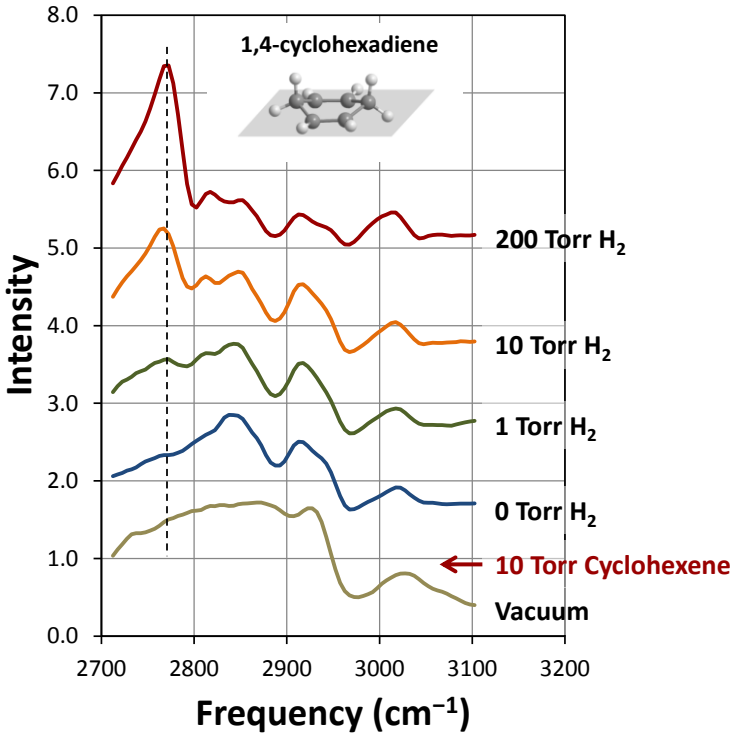

Fig. 4 *SFG spectra of 10 Torr cyclohexene in increasing H_2 pressure on Pt nanoparticles after UV cleaning for 60 min. In this experiment, the nanoparticles are supported directly on a SiO_2 prism. Cyclohexene dehydrogenates on Pt to form a 1,4-cyclohexadiene surface intermediate that is characterized by a strong feature in the SFG spectrum at 2,760 cm^{-1}. This feature is known to form on an atomically clean Pt surface even in the absence of H_2. In this case, the feature is initially absent from the spectrum, but grows in with increasing H_2 pressure. This indicates that H_2 is needed to open the carbonaceous shell on the UV-cleaned Pt nanoparticles and allow cyclohexene to access the Pt.*

To confirm this model in which carbonaceous fragments form a porous Pt coating in H_2 but collapse to a tightly closed shell in O_2, we used cyclohexene to probe the accessibility of reactants to the Pt surface. Cyclohexene forms a 1,4-cyclohexadiene surface intermediate on Pt.[33] This is a dehydrogenation product of the cyclohexene and forms even in the absence of H_2. The 1,4-cyclohexadiene species has a distinct molecular vibration at 2,760 cm^{-1} which is spectrally well resolved from any resonant modes of the capping agent. Consequently, cyclohexene represents a suitable probe molecule. To avoid changes in the nonresonant background with changing H_2 pressure, this experiment was performed using Pt nanoparticles supported directly on an SiO_2 prism. Fig. 4 shows the results of this experiment. When cyclohexene is introduced in the gas phase to UV-cleaned Pt nanoparticles, no 1,4-cyclohexadiene is observed in the SFG spectrum. Only weak features at 2,840 and 2,910 cm^{-1}

appear which we attribute to physisorbed cyclohexene. However, as the H_2 pressure is increased from 0 to 200 Torr, a strong feature at 2,760 cm^{-1} grows in corresponding to 1,4-cyclohexadiene. Because this feature forms on an atomically clean Pt single crystal surface even in the absence of H_2,[33] we conclude that for the UV-cleaned nanoparticles H_2 is needed to open the carbonaceous shell and allow cyclohexene to access the Pt. It is important to note that in this experiment the nanoparticles were pre-reduced with H_2, so that the oxidation state of Pt is not changing.

Fig. 5A shows the effect of UV cleaning time on the activity of the Pt nanoparticles for ethylene hydrogenation and methanol oxidation. The activity for each reaction is normalized to the initial activity of the PVP-capped nanoparticles before UV cleaning. For ethylene hydrogenation the rate increases with increased cleaning time, while for methanol oxidation the rate decreases with increased cleaning time. Following 3 h there is a 200-fold divergence of the rates for these two reactions. This suggests that with increased cleaning, the carbonaceous shell on the Pt nanoparticles becomes tighter and tighter in O_2; however, it can continue to open in H_2 allowing access to the Pt. In fact, the ethylene hydrogenation rate after UV cleaning is slightly greater than expected based on the geometric surface area of the Pt as determined by TEM. This suggests that the carbonaceous fragments have almost no site blocking effect in H_2. Fig. 5B shows the corresponding C and N surface concentrations as a function of UV cleaning time measured by XPS. After 30 min, the concentration of N is below the limit of detection by XPS. The C concentration also levels off after 30 min to a steady value representing only 10% of the initial C. Again it is impossible to distinguish if this C is a decomposition product of the PVP or if it is contamination of the cleaned Pt surface.

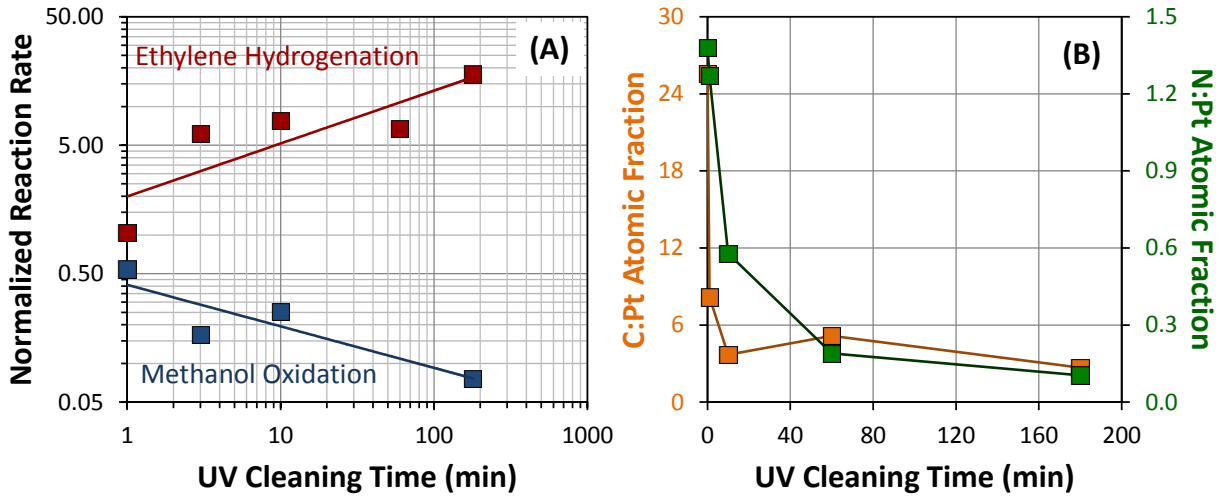

Fig. 5 (A) *Reaction rates as a function of UV cleaning time for ethylene hydrogenation and methanol oxidation. The reaction rates are normalized to the initial rate for each reaction before UV cleaning. The results show that the rates of the two reactions continue to diverge with increased cleaning time, eventually showing a 200-fold difference in activity.* **(B)** *C:Pt and N:Pt atomic fractions measured by XPS as a function of UV cleaning time. The N concentration on the surface drops below the limit of detection after 30 min of UV cleaning. The C concentration on the surface also levels off at a value representing only 10% of the initial C from the PVP capping layer.*

To determine if the formation of this carbonaceous shell is a general phenomenon, we synthesized Pt nanoparticles using an alternate method where the capping agent is added after synthesis. This allowed us to add different capping agents to identical nanoparticle aliquots to isolate the cap as the sole variable between two nanoparticle samples. For this experiment, PVP and oleic acid (OA) were used as capping agents in two separate aliquots, and the activity of these catalysts were monitored for ethylene hydrogenation and methanol oxidation before and after cleaning. In this case, thermal oxidation in a tube furnace was used for cap removal rather than UV cleaning. The OA-capped nanoparticles were cleaned at 473 K, but the PVP-capped nanoparticles required thermal treatment at 573 K for PVP removal consistent with previous work on the thermal degradation of Pt–PVP complexes.[32] Following cleaning the PVP- and OA-capped nanoparticles showed a 100-fold and 30-fold increased activity for ethylene hydrogenation, respectively.

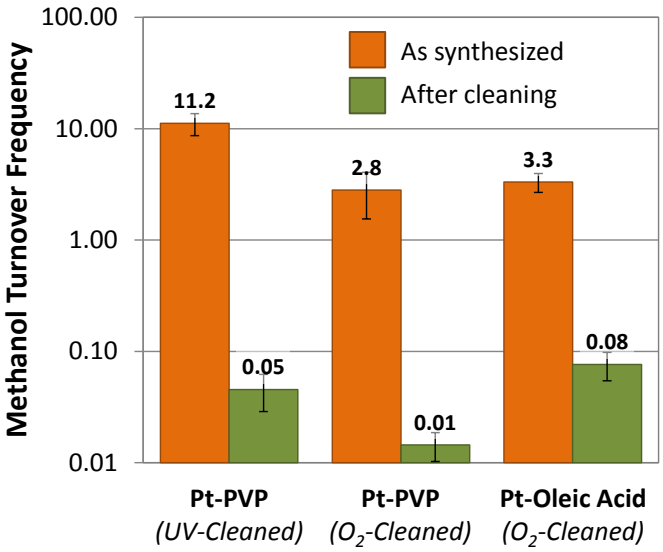

Fig. 6 *Methanol oxidation turnover frequency (TOF) for Pt nanoparticle catalysts before and after cap removal. TOF is given as the number of methanol molecules converted per Pt site per s. The number of platinum sites was determined from the measured rate of ethylene hydrogenation using a known TOF. Consequently, each bar shows the methanol oxidation rate relative to the ethylene hydrogenation rate on the same catalyst. Data is shown for all three types of nanoparticles studied (i.e., UV-cleaned Pt–PVP, thermally-cleaned Pt–PVP, and thermally-cleaned Pt–OA). Noting that this graph is on a log-scale, the Pt activity for methanol oxidation is shown to decrease for each catalyst by a factor of between 50 and 250 following cap removal.*

Fig. 6 shows the effect of cap removal on the activity for methanol oxidation. In this figure, the methanol oxidation rate for each catalyst is represented as a turnover frequency normalized to the number of Pt active sites determined by ethylene hydrogenation.[23] Consequently, each bar shows the methanol oxidation rate relative to the ethylene hydrogenation rate on the same catalyst. Data is shown for all three types of nanoparticles studied (i.e., UV-cleaned Pt–PVP, thermally-cleaned Pt–PVP, and thermally-cleaned Pt–OA). Noting that this graph is on a log-scale, the Pt activity for methanol oxidation is shown to decrease for each

catalyst by a factor of between 50 and 250 following cap removal. Because these values are normalized to the catalyst activity for ethylene hydrogenation, this cannot be the result of nanoparticle sintering. It seems clear that for methanol oxidation, the capped nanoparticles are dramatically more active than their cleaned analogues, and this finding applies to multiple capping agents and cleaning methods.

9.5 Conclusions

These results demonstrate the important role of an organic cap to mediate the catalytic properties of colloidal nanoparticles. We studied the effect of UV cap removal on the catalytic activity of PVP-capped Pt nanoparticles for ethylene hydrogenation and methanol oxidation. UV cleaning effectively removes the PVP cap from the Pt, but SFG shows that carbonaceous fragments are still present on the nanoparticles. These carbonaceous fragments are dynamic and appear to block Pt active sites in during methanol oxidation but not during ethylene hydrogenation. We propose a model where a carbonaceous shell forms on the Pt nanoparticle that is tightly closed in O_2 but becomes permeable in H_2. To support this model, cyclohexene served as a probe molecule to show that following UV cleaning, reactant molecules can only access the Pt when H_2 is present to open the carbonaceous shell. Kinetic measurements on PVP- and OA-capped nanoparticles cleaned by thermal oxidation show that this effect applies to multiple capping agents and cleaning methods. This work highlights the important role of an organic cap in nanoparticle catalysis and provides one example where capped nanoparticles are dramatically better catalysts than their cleaned analogues.

9.6 References

(1) *Preparation of Solid Catalysts*; Ertl, G.; Knozinger, H.; Weitkamp, J., Eds.; Wiley-VCH: Weinheim, Germany, 1999.
(2) Tsoncheva, T.; Dal Santo, V.; Gallo, A.; Scotti, N.; Dimitrov, M.; Kovacheva, D. *Appl Catal a-Gen* **2011**, *406*, 13.
(3) Strongin, D. R.; Carrazza, J.; Bare, S. R.; Somorjai, G. A. *Journal of Catalysis* **1987**, *103*, 213.
(4) McCrea, K. R.; Parker, J. S.; Somorjai, G. A. *The Journal of Physical Chemistry B* **2002**, *106*, 10854.
(5) Andersson, M. P.; Abild-Pedersen, E.; Remediakis, I. N.; Bligaard, T.; Jones, G.; Engbwk, J.; Lytken, O.; Horch, S.; Nielsen, J. H.; Sehested, J.; Rostrup-Nielsen, J. R.; Norskov, J. K.; Chorkendorff, I. *Journal of Catalysis* **2008**, *255*, 6.
(6) Kliewer, C. J.; Bieri, M.; Somorjai, G. A. *Journal of the American Chemical Society* **2009**, *131*, 9958.
(7) Ahmadi, T. S.; Wang, Z. L.; Green, T. C.; Henglein, A.; El-Sayed, M. A. *Science* **1996**, *272*, 1924.
(8) Peng, X.; Wickham, J.; Alivisatos, A. P. *Journal of the American Chemical Society* **1998**, *120*, 5343.
(9) Puntes, V. F.; Krishnan, K. M.; Alivisatos, A. P. *Science* **2001**, *291*, 2115.
(10) Oh, M.; Mirkin, C. A. *Nature* **2005**, *438*, 651.
(11) Yin, Y.; Alivisatos, A. P. *Nature* **2005**, *437*, 664.
(12) Song, H.; Kim, F.; Connor, S.; Somorjai, G. A.; Yang, P. *The Journal of Physical Chemistry B* **2004**, *109*, 188.

(13) Rioux, R. M.; Song, H.; Hoefelmeyer, J. D.; Yang, P.; Somorjai, G. A. *The Journal of Physical Chemistry B* **2004**, *109*, 2192.
(14) Song, H.; Rioux, R. M.; Hoefelmeyer, J. D.; Komor, R.; Niesz, K.; Grass, M.; Yang, P.; Somorjai, G. A. *Journal of the American Chemical Society* **2006**, *128*, 3027.
(15) Bratlie, K. M.; Lee, H.; Komvopoulos, K.; Yang, P.; Somorjai, G. A. *Nano Letters* **2007**, *7*, 3097.
(16) Kuhn, J. N.; Huang, W.; Tsung, C.-K.; Zhang, Y.; Somorjai, G. A. *Journal of the American Chemical Society* **2008**, *130*, 14026.
(17) Grass, M.; Rioux, R.; Somorjai, G. *Catalysis Letters* **2009**, *128*, 1.
(18) Grass, M. E.; Joo, S. H.; Zhang, Y.; Somorjai, G. A. *The Journal of Physical Chemistry C* **2009**, *113*, 8616.
(19) Kliewer, C. J.; Aliaga, C.; Bieri, M.; Huang, W.; Tsung, C.-K.; Wood, J. B.; Komvopoulos, K.; Somorjai, G. A. *Journal of the American Chemical Society* **2010**, *132*, 13088.
(20) Witham, C. A.; Huang, W.; Tsung, C.-K.; Kuhn, J. N.; Somorjai, G. A.; Toste, F. D. *Nat Chem* **2010**, *2*, 36.
(21) Alayoglu, S.; Aliaga, C.; Sprung, C.; Somorjai, G. *Catalysis Letters* **2011**, *141*, 914.
(22) Zhang, Y.; Grass, M. E.; Kuhn, J. N.; Tao, F.; Habas, S. E.; Huang, W.; Yang, P.; Somorjai, G. A. *Journal of the American Chemical Society* **2008**, *130*, 5868.
(23) Kuhn, J. N.; Tsung, C.-K.; Huang, W.; Somorjai, G. A. *Journal of Catalysis* **2009**, *265*, 209.
(24) Albiter, M. A.; Crooks, R. M.; Zaera, F. *The Journal of Physical Chemistry Letters* **2009**, *1*, 38.
(25) Lu, J.; Fu, B.; Kung, M. C.; Xiao, G.; Elam, J. W.; Kung, H. H.; Stair, P. C. *Science* **2012**, *335*, 1205.
(26) Gorin, D. J.; Sherry, B. D.; Toste, F. D. *Chemical Reviews* **2008**, *108*, 3351.
(27) Li, Y.; Liu, J. H.-C.; Witham, C. A.; Huang, W.; Marcus, M. A.; Fakra, S. C.; Alayoglu, P.; Zhu, Z.; Thompson, C. M.; Arjun, A.; Lee, K.; Gross, E.; Toste, F. D.; Somorjai, G. A. *Journal of the American Chemical Society* **2011**, *133*, 13527.
(28) Mitsudome, T.; Mikami, Y.; Matoba, M.; Mizugaki, T.; Jitsukawa, K.; Kaneda, K. *Angewandte Chemie International Edition* **2012**, *51*, 136.
(29) Bratlie, K. M.; Komvopoulos, K.; Somorjai, G. A. *The Journal of Physical Chemistry C* **2008**, *112*, 11865.
(30) Aliaga, C.; Park, J. Y.; Yamada, Y.; Lee, H. S.; Tsung, C.-K.; Yang, P.; Somorjai, G. A. *The Journal of Physical Chemistry C* **2009**, *113*, 6150.
(31) Shen, Y. R. *The principles of nonlinear optics*; Wiley-Interscience, 2003.
(32) Borodko, Y.; Habas, S. E.; Koebel, M.; Yang, P.; Frei, H.; Somorjai, G. A. *The Journal of Physical Chemistry B* **2006**, *110*, 23052.
(33) Yang, M.; Chou, K. C.; Somorjai, G. A. *The Journal of Physical Chemistry B* **2003**, *107*, 5267.

Chapter 10

Removing Poly(vinylpyrrolidone) from Size-Controlled Platinum Nanoparticles for Catalytic and Sum Frequency Generation Spectroscopic Studies: Solvent Cleaning as an Alternative to UV Cleaning

10.1 Abstract

Recent work with nanoparticle catalysts reveals that size and shape control on the nanometer scale allows for control of reaction rate and selectivity. Additionally, it has been shown that SFG vibrational spectroscopy is a powerful tool for studying heterogeneous catalysis because it allows for the observation of surface intermediates during catalytic reactions. To control the size and shape of catalytic nanoparticles, an organic ligand acts as a cap to stabilize the nanoparticle during synthesis. The presence of an organic cap presents two major challenges to SFG and catalytic reaction studies: First, the presence of the cap may block active sites on the nanoparticle reducing the catalytic activity. Second, the cap often shows a strong signal in the SFG spectrum, making the observation of reaction intermediates on the nanoparticles difficult or impossible. In this work, we consider two methods for cleaning Pt nanoparticles capped with poly(vinylpyrrolidone) (PVP): solvent cleaning and UV cleaning. We find that both UV cleaning and solvent cleaning make it possible to observe reaction intermediates by SFG. However, we find that the solvent cleaning method produces nanoparticles that are stable in reaction conditions, while UV cleaning of the nanoparticles leads to particle agglomeration during reaction. This understanding makes it possible now to study size- and shape-induced nanoparticle selectivity with SFG vibrational spectroscopy.

10.2 Introduction

Sum frequency generation (SFG)[1,2] vibrational spectroscopy is an interface-specific, second order optical process that measures the vibrational spectrum of molecules on a surface or at an interface. It has been shown that SFG vibrational spectroscopy is a powerful tool for studying heterogeneous catalysis because it allows for the observation of surface intermediates during catalytic reactions. Previously this technique has been applied to studying reactions occurring on both single crystal catalysts[3-5] and 2-dimensional films of nanoparticle catalysts[6,7]. Recent work with nanoparticle catalysts reveals that size and shape control on the nanometer scale allows for control of reaction selectivity.[8-10] This is a major advance for heterogeneous catalysis, and motivates the present effort to observe reaction intermediates on size- and shape-controlled nanoparticles under reaction conditions.

A major challenge of these studies is to observe the reaction intermediates on the background of molecular stretches that originate from the organic capping layer of the nanoparticles. Nanoparticles require a layer of organic ligands to stabilize both its size and shape. However, the organic cap has two major effects on the catalytic reaction studies. First,

the presence of the cap may block active sites on the nanoparticle reducing the catalytic activity. Second, the cap often shows a strong signal in the SFG spectrum, making the observation of reaction intermediates on the nanoparticles difficult or impossible. Common capping agents, including poly(vinylpyrrolidone) (PVP),[11] cetyltrimethylammonium bromide (CTAB),[12] tetradecyltrimethylammonium bromide (TTAB),[13] hexadecylamine (HDA),[14] and oleylamine[15], produce signal in the aliphatic range making it difficult, if not impossible, to identify C-H vibrations of reactive catalytic intermediates.

In previous studies, UV light has been used to clean the organic cap from the nanoparticles.[14,15] The results of these studies show that UV treatment increases the catalytic activity of the nanoparticles and minimizes C-H vibrations, leaving a clean background for observing reaction intermediates by SFG. The present study focuses on a comparison between this UV method for cleaning the nanoparticles and a simpler, yet effective method, namely, solvent washing to remove excess capping from the nanoparticles. In our studies, we use Pt nanoparticles capped with PVP. We find that both UV cleaning and solvent cleaning make it possible to observe reaction intermediates by SFG. However, we find that the solvent cleaning method produces nanoparticles that are stable in reaction conditions, while UV cleaning of the nanoparticles leads to particle agglomeration during reaction. This advance makes it possible now, for the first time, to study size- and shape-induced nanoparticle selectivity with SFG vibrational spectroscopy.

The cyclohexene (C_6H_{10}) hydrogenation reaction is a good candidate for SFG analysis because its intermediates have unique and well-documented[5,16-20] vibrational signatures. Three different reaction intermediates of cyclohexene hydrogenation exist on Pt and are easily identifiable from the SFG spectrum: 1,4-cyclohexadiene (1,4-CHD), 1,3-cyclohexadiene (1,3-CHD) and the π-allyl intermediate. The spectrum of 1,4-CHD has a single peak at 2760 cm^{-1} corresponding to a strongly red-shifted CH_2 asymmetric stretch. 1,3-CHD has three CH_2 stretches (2830, 2875, 2900 cm^{-1})[17]. The π-allyl has a strong CH_2 asymmetric stretch at 2920 cm^{-1} and a weak symmetric CH_2 stretch at 2840 cm^{-1}. Using cyclohexene hydrogenation on Pt as a model reaction, we investigate the catalytic activity and vibration spectra of solvent-cleaned Pt nanoparticles under reaction conditions and compare these results with PVP-capped nanoparticles and UV-cleaned nanoparticles.

10.3 Experimental

10.3.1 Nanoparticle Synthesis

4.2 nm Pt particles were synthesized using 100 mg chloroplatinic acid hexahydrate ($H_2Pt(IV)Cl_6 \cdot 6H_2O$, 37.5% metal basis, Sigma Aldrich), 440 mg PVP (29 K, Sigma Aldrich), and 20 mL ethylene glycol (ReagentPlus, Sigma Aldrich). The mixture was combined in a 25 mL round bottom flask, pumped to remove air and flushed with Ar. The flask was then placed in an oil bath at 165 °C for 1 h under Ar flow.

3.0 nm Pt nm nanoparticles[21] were synthesized using 40 mg ammonium tetrachloroplatinate(II) ($(NH_4)_2Pt(II)Cl_4$), 220 mg PVP (29 K, Sigma Aldrich), and 20 mL ethylene glycol (ReagentPlus, Sigma Aldrich). The mixture was combined in a 25 mL round

bottom flask, pumped to remove air and flushed with Ar. The flask was then placed in an oil bath at 165 °C for 30 min under Ar flow.

1.7 nm Pt particles[22] were synthesized by combining 250 mg chloroplatinic acid hexahydrate ($H_2Pt(IV)Cl_6 \cdot 6H_2O$, 37.5% metal basis, Sigma Aldrich), 25 mL ethylene glycol (ReagentPlus, Sigma Aldrich) and 0.00625 g NaOH under Ar at 433 K for 1 h. After synthesis, the particles were precipitated with 1.0 M HCl and then combined with PVP.

The nanoparticles of each size were separated from the ethylene glycol synthesis mixture by precipitation with acetone and centrifugation at 4000 RPM for 5 min. The nanoparticles were then dissolved by sonication in 20 mL of ethanol and then mixed with 25 mL of hexane and centrifuged again for precipitation. This process was repeated 3 times to remove ethylene glycol and excess chloroplatinic acid from the synthesis. In this paper,we refer to these nanoparticles as fully-capped.

10.3.2 Solvent Cleaning

For the 4.2 and 3.0 nm nanoparticles solvent cleaning consisted of five additional cycles of ethanol washing followed by precipitation in hexane for a total of eight ethanol washes. Following these cycles of ethanol washing, the particles were further washed 2 times, once in chloroform and once in isopropyl alcohol.

1.7 nm Pt retain less PVP and do not require as many washing cycles. These particles were washed only one additional time in ethanol for a total of four ethanol washes. If washed more times, the nanoparticles aggregated in solution.

10.3.3 Langmuir-Blodgett (LB) Film Deposition

Particles were dissolved in a 50/50 ethanol/chloroform mixture before being deposited onto a water surface for LB deposition.[23] For LB deposition, a suspension of nanoparticles in the ethanol/chloroform mixture is dispersed onto a water surface. Time is given for the organic solvent to evaporate, leaving a 2-dimensional dispersion of nanoparticles on the water. The film is then compressed, and the surface pressure is monitored. The surface pressure corresponds to the density of nanoparticles on the water. When the desired surface pressure is reached, the SFG prism is pulled out from under the surface of the water, and the film of nanoparticles is deposited onto the substrate. For SFG experiments, a surface pressure of 20 dyn/cm were used for LB films. Film deposition on TEM grids was achieved by dropping the grid on the compressed LB film for 10 sec followed by retrieval with tweezers. For TEM experiments, a surface pressure of only 8 dyn/cm was used. The lower density used in TEM experiments provided better images and more clear visibility of nanoparticle aggregation that occurred for some samples during catalytic reaction. The Nima 611 LB trough was used for all experiments with filter paper as the surface tension probe.

10.3.4 UV Cleaning

Two low-pressure mercury lamps (Lights Sources Inc., model number GPH357T5VH/4P) were used for UV treatment inside a clean aluminum box. Samples were

placed 5 mm below one lamp and exposed to 254 and 185 nm irradiation for the specified period of time.

10.3.5 Sum Frequency Generation (SFG)

A mode-locked Nd:YAG dye laser (Continuum D-20) with a fundamental output of 1064 nm, 20 Hz repetition rate and 20 picosecond pulse width was used for all experiments described herein. A frequency doubling crystal is used to generate the fixed visible (532 nm) from the fundamental beam. An optical parametric generator/amplifier produces tunable infrared (2680 to 3180 cm^{-1}) corresponding to stretching modes of aliphatic and aromatic groups. Visible and infrared beams are spatially and temporally overlapped at the base of the prism with angles 65 and 42°, respectively, to achieve total internal reflection. Visible and infrared beam powers were both 130 μJ before entering the prism. All experiments are performed with the ppp polarization combination. Polished fused silica equilateral (60°) prisms (ISP Optics) were used for all experiments. SFG photons are detected using a photomultiplier tube with a gated boxcar integrator. Samples probed by SFG consist of a nanoparticle film deposited on the prism surface. This film is probed under reaction conditions at pressures up to 1 atm.[24]

10.3.6 Transmission Electron Microscopy

Transmission electron microscopy (TEM) images of LB films were performed on a JOEL 2100 microscope operated at 200 kV. Silicone (SiO) films on copper grids (Electron Microscopy Sciences) were used as substrates for all TEM images presented. Scanning Electron Microscope (SEM) images were taken with a Zeiss Gemini Ultra-55 microscope on thermally grown silica (SiO_2) substrates.

10.3.7 Kinetic Measurements

Turnover rates were measured using a Hewlett-Packard 5890 Series II gas chromatagraph connected to a circulating batch reactor. The ST-123 column was used to measure ethylene hydrogenation rate and the XY3928 column was used for cyclohexene hydrogenation.

10.4 Results and Discussion

10.4.1 PVP Removal is Necessary to Detect Reaction Intermediates on Pt Nanoparticles

The capping agent presents a challenge for SFG studies on colloidal nanoparticle catalysts because signal from the cap often overlaps with signal from the reactive intermediate of interest. Even if the cap did not interfere with the detection of reaction intermediates, it still physically blocks much of the available catalyst surface, preventing adsorption of reactants at high surface coverage. We find that in the presence of H_2, PVP disorders dramatically, such that the background signal produced by the cap is greatly reduced (see Fig. 1A). However, even in the absence of a background signal from the PVP, no signal is observed from a reaction intermediate during cyclohexene hydrogenation (see Fig. 1B). This is because very little adsorption of cyclohexene occurs because the disordered PVP still blocks the majority of Pt sites.

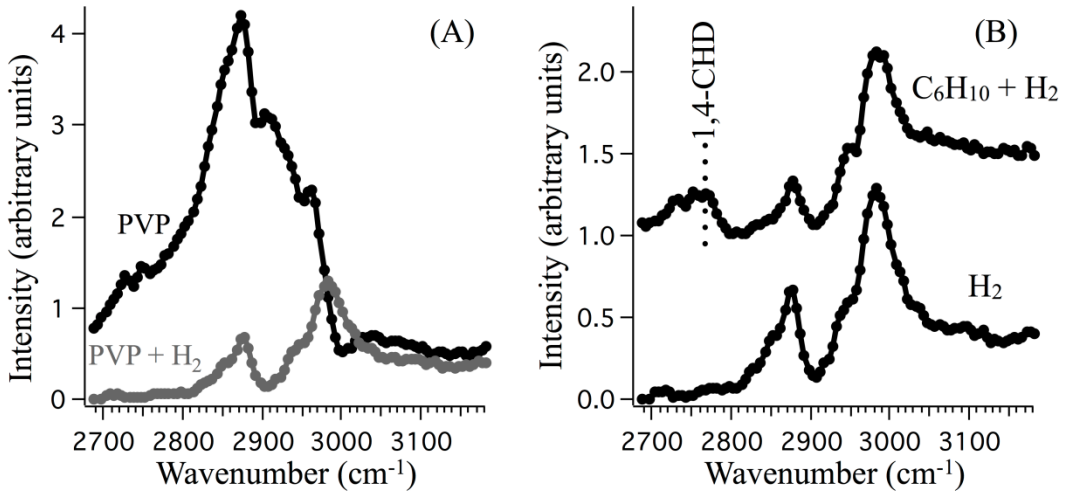

Fig. 1 *SFG spectra for 4.2 nm Pt nanoparticles fully-capped with PVP at 295 K. The film is exposed to an inert atmosphere (760 Torr Ar), H_2 (200 Torr H_2, 560 Torr Ar) and cyclohexene hydrogenation conditions (10 Torr C_6H_{10}, 200 Torr H_2, 560 Torr Ar). Spectra are offset for clarity in right plot. Unlabeled features are attributed to PVP.*

Contrast these results from capped nanoparticles with the results from solvent-cleaned nanoparticles. In the case of solvent-cleaned nanoparticles, there is still a strong signal from the PVP (see Fig. 2A). This is because solvent cleaning does not remove all the PVP from the nanoparticles; if it did, the particles would aggregate in solution. As in the case of the fully-capped particles, the signal from the PVP diminishes in H_2 due to the disordering effect (see Fig. 2A). However, the major difference between the capped particles and the solvent-cleaned particles is obvious from the spectrum taken under reaction conditions (see Fig. 2B). In the case of solvent-cleaned nanoparticles, the 1,4-CHD intermediate is clearly visible indicating significant adsorption on the Pt surface. From this we conclude that although the solvent-cleaned particles are still lightly capped with PVP, there are sufficient Pt sites available for catalysis to occur and to observe the reaction intermediates by SFG.

Because the peak of 1,4-CHD occurs at a unique location compared to other aliphatic vibrations, it is certain that it arises from a chemisorbed reaction intermediate on the surface of Pt and not from the PVP. Interestingly, cyclohexene is introduced with H_2, PVP peaks are further decreased from the level observed with only H_2. This suggests 1,4-CHD may displace PVP from the Pt surface into an even more disordered geometry. Spectra were also taken during cyclohexene hydrogenation on 1.7 and 3.0 nm Pt particles. These spectra (not shown) also indicate the formation of the 1,4-CHD surface intermediate. 1.7 nm Pt particles retain less PVP than large particles and do not require as much solvent cleaning as the large particles to observe the surface intermediate (see Experimental Section for details).

The role of solvent cleaning to increase the Pt surface area is intuitive. However, the role of the H_2 to decrease the background signal produced by the PVP is less obvious, so we discuss it now in detail. H_2 dramatically lowers the signal from PVP on both fully-capped and solvent-

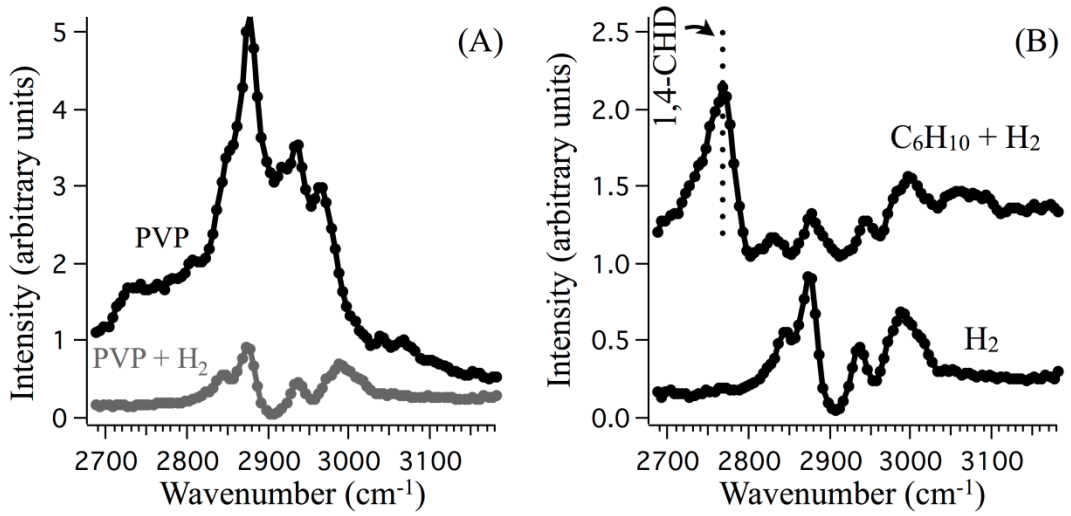

Fig. 2 *SFG spectra for solvent-cleaned 4.2 nm Pt nanoparticles at 295 K. The film is exposed to an inert atmosphere (760 Torr Ar), H_2 (200 Torr H_2, 560 Torr Ar) and cyclohexene hydrogenation conditions (10 Torr C_6H_{10}, 200 Torr H_2, 560 Torr Ar). Spectra are offset for clarity in right plot. Unlabeled features are attributed to PVP.*

cleaned nanoparticles. Under an inert atmosphere of Ar gas, the full signal of PVP capping is strong for both types. However, adding H_2 reduces the signal of PVP to relatively weak peaks located at 2850 cm^{-1} (CH_2-s, chain), 2870 cm^{-1} (CH_2-s, ring), 2930 cm^{-1} (CH_2-a, ring) and 2990 cm^{-1} (CH_2-a, ring).[25]

Selection rules of SFG indicate decreasing concentration or increasing disorder reduce SFG signal. The effect of concentration on the spectral intensity is intuitive, but it is important here to emphasize the effect of molecular ordering on the spectral intensity. Because SFG vibrational spectroscopy is a coherent process, it is not only sensitive to the individual molecular susceptibilities, but also to the net susceptibility of the entire ensemble of molecular oscillators. Consequently, if molecules on a surface are highly disordered, the net ensemble will not produce a strong SFG signal, even if the concentration is high.

The following two examples emphasize this concept: In a recent study,[26] the ordering of self-assembled monolayers of C_{60} functionalized phosphoric acid was tuned by varying fluorination of the phosphoric acid alkyl chain. For certain F/C_{60} ratios, SFG intensity from C_{60} molecules decreased even as surface density increased. This effect is attributed to disordering of the self-assembled monolayer. In another case,[5] the observed peaks from the π-allyl intermediate on Pt(111) increased in intensity by eight times when pressure was changed from ambient to ultra-high vacuum. Although the surface concentration did not increase in vacuum relative to ambient pressure, an increase in order strongly contributed to the signal enhancement. We conclude that the addition of H_2 disorders PVP on Pt as indicated by a decrease in SFG signal of ~90%. This spectral change is reversible, and if the cell is evacuated back to vacuum, the full signal of PVP reappears.

UV light at 254 and 185 nm is known to photo-decompose organic material, including PVP, through photolysis and ozonolysis mechanisms.[27] Accordingly, UV cleaning is proposed[28] as a viable method for removing the PVP cap from Pt nanoparticles, but the effects of UV cleaning are on the catalytic behavior of the Pt nanoparticles are not fully understood.

Fig. 3 shows SFG spectra of PVP-capped Pt nanoparticles after 180 min UV exposure. The spectrum of the Pt nanoparticles in Ar (Fig. 3A) shows a significant signal reduction in the aliphatic range compared to the fully-capped or solvent-cleaned nanoparticles under the same condition. This is due to the photodecomposition of PVP by the UV light. XPS data substantiates the idea of PVP removal by UV cleaning; XPS shows that the C content on the Pt nanoparticles decreased by 90% following UV cleaning. However, when the UV-cleaned nanoparticles are exposed to H_2, the signal in the aliphatic range increases significantly. This suggests that although UV cleaning removes the majority of the PVP, it leaves a C shell that reacts with H_2. This observation highlights the difficulty of preparing atomically clean Pt nanoparticles by UV cleaning. We find that even extensive cleaning by UV light, fails to remove a C shell that subsequently reacts with H_2. This shell appears to be a dynamic actor in the catalytic reaction, and further studies are in progress to probes the effect of the C shell on Pt catalysis. However, the shell does not prevent adsorption of cyclohexene, and the 1,4-CHD, 1,3-CHD, and π-allyl intermediates are all readily observed on the UV-cleaned particles under reaction conditions (see Fig. 3B).

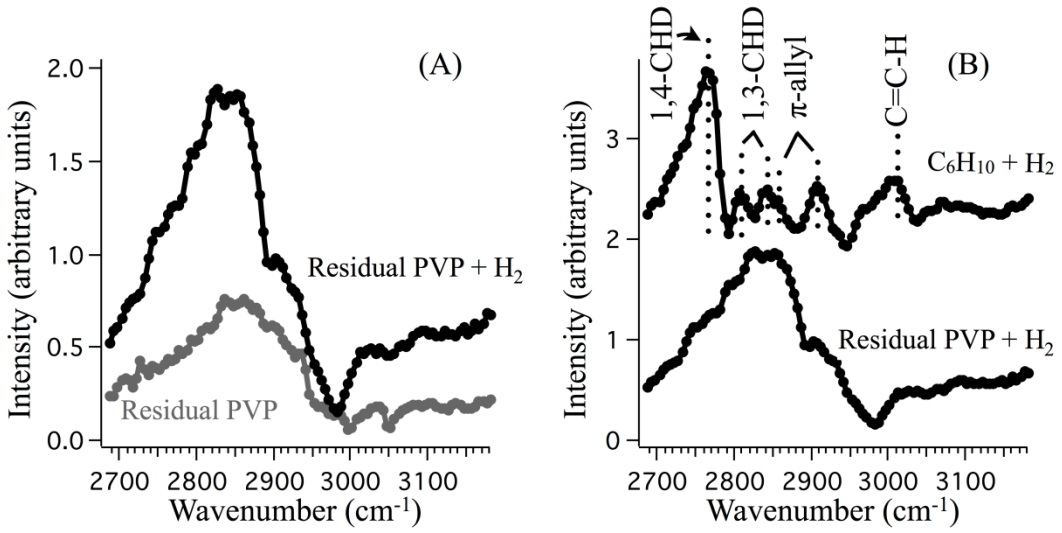

Fig. 3 *SFG spectra for UV-cleaned 4.2 nm Pt nanoparticles at 295 K. The film is exposed to an inert atmosphere (760 Torr Ar), H_2 (200 Torr H_2, 560 Torr Ar) and cyclohexene hydrogenation conditions (10 Torr C_6H_{10}, 200 Torr H_2, 560 Torr Ar). Spectra are offset for clarity in right plot.*

Fig. 4A shows the SFG of Pt nanoparticles (4.2 nm) during cyclohexene hydrogenation reaction conditions as a function of UV cleaning time, and Fig. 4B shows the C:Pt atomic ratio also as a function of UV cleaning measured by XPS. We find that with UV cleaning the PVP is removed as evidenced by a decrease in the XPS C signal. Correspondingly, we find that the

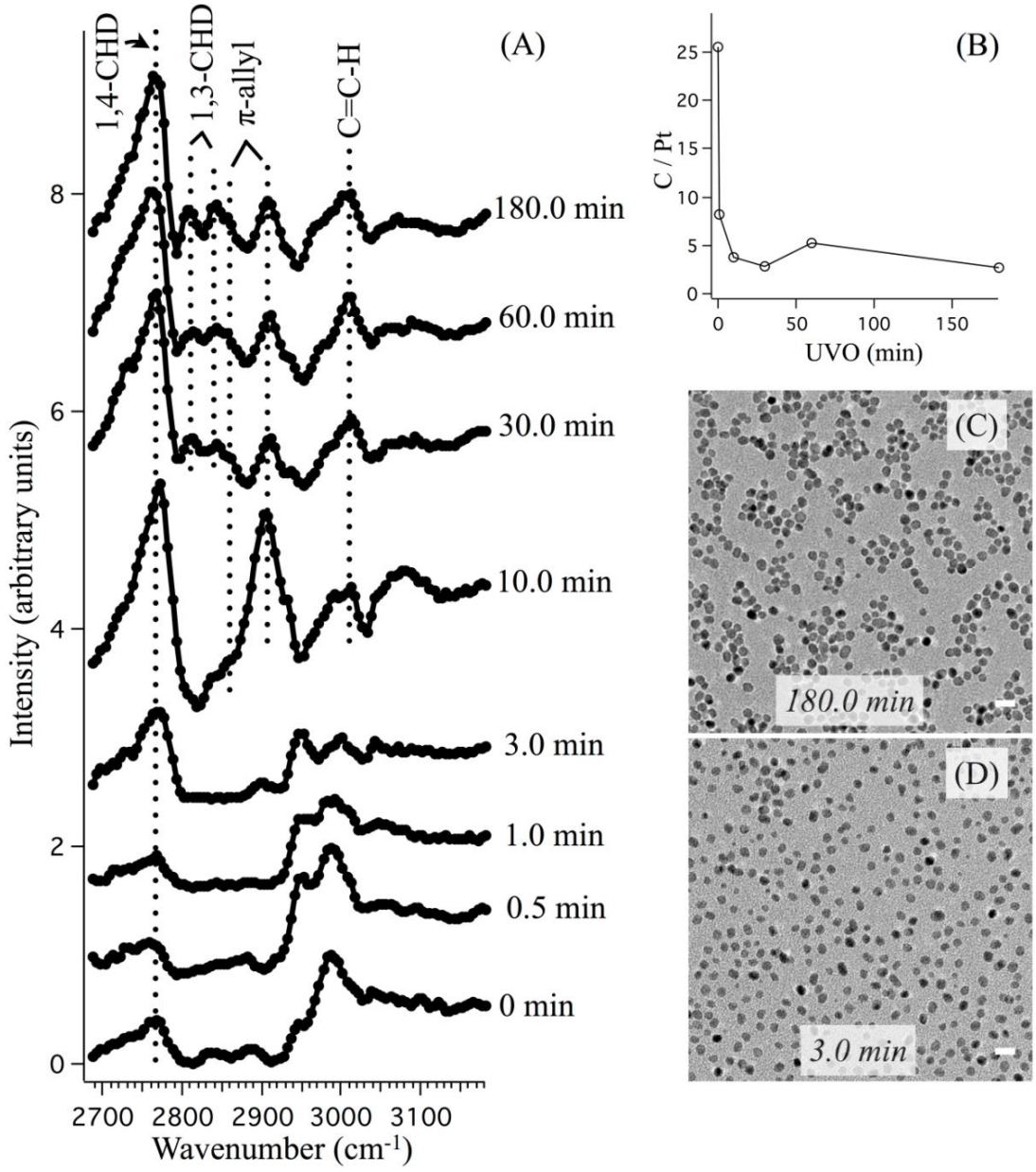

Fig. 4 *SFG spectra (A) collected at 295 K after UV treatment (0 to 180 min) under cyclohexene hydrogenation reaction conditions (10 Torr C_6H_{10}, 200 Torr H_2, 550 Torr Ar). The observed intermediates change from being exclusively 1,4-CHD (0 to 3 min) to 1,4-CHD, 1,3-CHD and the π-allyl (30 to 180 min). XPS results (B) show the C/Pt ratio as a function of UV exposure. TEM images (C, D) collected after UV show clustering following long treatment but no aggregation (scale bar = 10 nm).*

signal from reaction intermediates steadily increases as the nanoparticles are cleaned. This is most obvious in the signal from the 1,4-CHD intermediate at 2765 cm^{-1}. However, there are additional changes to the spectrum that occur with increased UV cleaning. For particles treated 0-3 min, only the 1,4-CHD is observed. After 10 min of UV cleaning, an intense new peak appears at 2900 cm^{-1} with a weak counterpart at 2850 cm^{-1}, revealing the π-allyl adsorption geometry. With UV cleaning times from 30 to 180 min, the π-allyl signal decreases and weak peaks appear indicating 1,3-CHD. To observe each of these three intermediates on the Pt[111] single crystal, the temperature must change from 303 to 483 K.[20]

We have confirmed by TEM (see Fig. 4C and D) that the nanoparticles are morphologically stable during these experiments that were performed only at low temperature (298 K). Consequently, we cannot attribute the change in observed intermediates to a size or shape effect. It is interesting to note that the 1,3-CHD intermediate is much more active for cyclohexene hydrogenation than the 1,4-CHD intermediate.[29] Accordingly, we would expect that the 180 min UV-cleaned nanoparticles would be more catalytically active than the fully-capped nanoparticles because the highly active 1,3-CHD intermediate is only observed on the catalyst after UV cleaning. In fact, this is true. The UV-cleaned catalyst is approximately three times more active for cyclohexene hydrogenation than the fully-capped catalyst, even after correcting for the number of Pt active sites. These spectral changes, which correlate with reaction kinetics, suggest that besides simply blocking Pt sites, the capping agent may also actively promote or inhibit the formation of certain reaction intermediates. The idea of considering the cap as an active, dynamic support for nanoparticle catalysis is an interesting direction which we hope address in the future.

10.4.2 Solvent Cleaning Preserves the Size Monodispersity of Pt Nanoparticles During Reaction

We now compare the stability of the nanoparticles under reaction conditions following solvent cleaning and UV cleaning. Fig. 5 shows TEM images of fully-capped Pt nanoparticles of three sizes (4.2 nm, 3.0 nm, and 1.7 nm) as-deposited, following UV cleaning, and following UV cleaning and exposure to H_2 at 373 K. For the 4.2 and 3.0 nm Pt nanoparticles, UV cleaning leads to aggregation of particles into clusters, but the particles are still discrete and maintain a monodisperse size distribution. However, following exposure to H_2 at 373 K, these nanoparticles melt causing a loss of size monodispersity. The 1.7 nm Pt particles are even less stable and melt after UV cleaning even before exposure to elevated temperature. Although the images shown were taken on silicone TEM grids, we have observed the same phenomenon on several other supports, including SiO_2 and TiO_2.

Fig. 5 also shows TEM images demonstrating the stability of solvent-cleaned Pt nanoparticles. These images show the solvent-cleaned nanoparticles of 4.2, 3.0, and 1.7 nm sizes following H_2 exposure at 473 K (100 K higher temperature than for the UV-cleaned nanoparticles). We see that even at 474 K the solvent-cleaned nanoparticles are completely stable. This represents a major advantage of solvent cleaning compared to UV cleaning. Although UV cleaning is effective for removing the PVP, it leads to instability of the nanoparticles in reaction conditions so size monodispersity is lost. However, solvent cleaning produces stable nanoparticle catalysts that, for the first time, will allow for SFG studies of nanoscale size effects in catalysis.

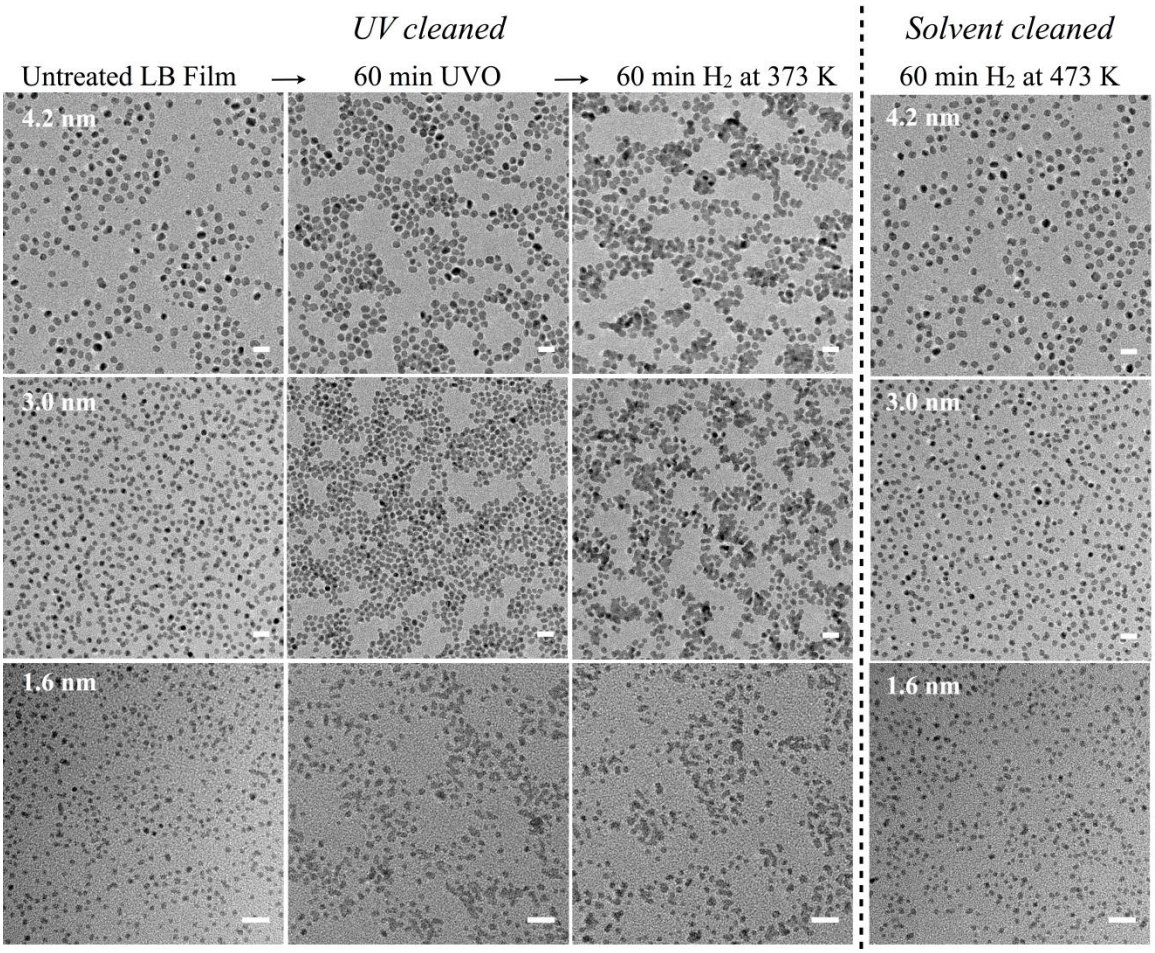

Fig. 5 *TEM images (scale bar = 10 nm) comparing UV-cleaned and solvent-cleaned Pt nanoparticles before and after reaction. For 4.2 and 3.0 nm nanoparticles, 60 min UV causes clustering where neighboring nanoparticles move close to one another while still maintaining size. Under hydrogenation reaction conditions (200 Torr H_2, 560 Torr Ar, 373 K), clustered nanoparticles often fuse and make much larger particles. Spherical 1.7 nm nanoparticles aggregate immediately under 60 min UV. In contrast, solvent-cleaned nanoparticles are unchanged up to at least 473 K with H_2 (200 Torr H_2 with 560 Torr Ar).*

10.4.3 Both Solvent Cleaning and UV Cleaning Increase the Number of Pt Active Sites

We also investigated the role of solvent cleaning and UV cleaning on the available surface area of the nanoparticles. For this study we used ethylene hydrogenation at 298 K as a way to probe the number of Pt active sites on a LB film. Ethylene hydrogenation is a structure-insensitive reaction with a well characterized turnover frequency (TOF) on Pt.[30] Accordingly the activity of a catalyst for ethane production from ethylene can be used to determine the approximate number of active Pt sites on the catalyst.

Fig. 6 shows the number of Pt active sites per cm^2 for LB films of fully-capped, solvent-cleaned, and UV-cleaned nanoparticles. The surface coverage of Pt nanoparticles on the LB films was controlled by the surface pressure of the nanoparticles during film deposition, and

should not vary significantly between samples. We find that at a surface pressure of 30 mN/m, there is a 30–50% surface coverage of Pt nanoparticles deposited on the substrate. Assuming a 4.2 nm spherical particle with a [111] surface, this surface coverage would indicate approximately 2×10^{15} Pt sites per cm^2 if there were no poisoning by the PVP cap.

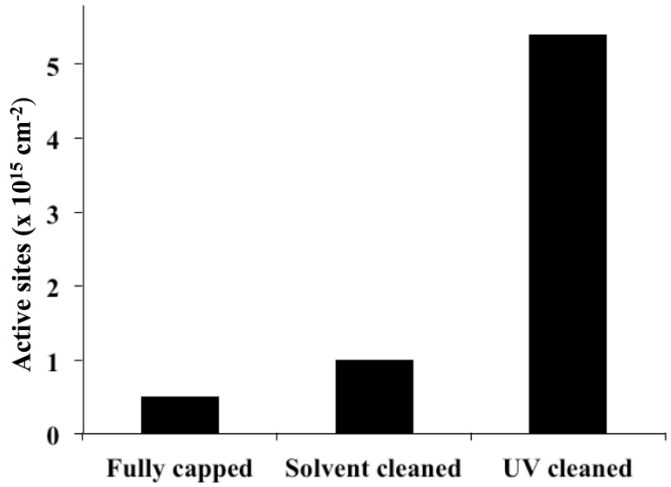

Fig. 6 *Active sites calculation based on ethylene hydrogenation rate for 4.2 nm Pt-PVP with three preparations: fully-capped, solvent-cleaned, and UV-cleaned.*

We find that the fully-capped nanoparticles show 5×10^{14} active sites per cm^2 as measured by ethylene hydrogenation which represents approximately 20% of the geometric area. The solvent-cleaned nanoparticles show 1×10^{15} active sites per cm^2, and the UV-cleaned nanoparticles show an 4×10^{15} active sites per cm^2 as measured by ethylene hydrogenation, corresponding to 40% and >100% of the geometric area, respectively. We attribute the high activity of the UV-cleaned particles to a deviation of the actual number of active sites per particle from what is expected by assuming a sphere with a perfect [111] surface. However, this comparison is still insightful and shows that while solvent cleaning increases the available number of Pt sites by a factor of 2, UV cleaning is much more effective for removing the PVP cap, increasing the number of available Pt sites by a factor of 10. This likely also explains the instability of UV-cleaned particles during reaction compared to the solvent-cleaned particles. The solvent-cleaned particles are stabilized by a significant amount of PVP that still caps more than half of the nanoparticle surface.

10.5 Conclusions

We have addressed two major challenges to observing catalytic reaction intermediates on ligand-capped nanoparticles: 1) interference by SFG signal generated by the organic cap and 2) blocking of catalytic active sites by the organic cap. We demonstrate that the under hydrogenation reaction conditions, PVP on Pt disorders such that the SFG signal in the C-H stretch range from the PVP is negligible. This provides a clean background for probing reaction intermediates by SFG. We also demonstrate that solvent cleaning of the PVP from the nanoparticles increases the number of Pt active sites. This increases both the catalytic activity of the nanoparticles and allows for sufficient signal from adsorbed reactants to probe the vibrational

spectrum of reaction intermediates by SFG. While a similar increase in catalytic activity can be obtained by UV cleaning of the Pt nanoparticles, UV cleaning leads to agglomeration of the nanoparticles during reaction at temperatures as low as 373 K. However, solvent-cleaned nanoparticles are completely stable, even in reaction conditions in excess of 473 K. Accordingly, solvent cleaning is desirable when probing nanoscale size and shape effects in nanoparticle catalysis because it allow for SFG studies without compromising the size monodispersity of the nanoparticles.

10.6 References

(1) Lambert, A. G.; Davies, P. B.; Neivandt, D. J. *Applied Spectroscopy Reviews* **2005**, *40*, 103.
(2) Shen, Y. R. *Nature* **1989**.
(3) Kliewer, C. J.; Bieri, M.; Somorjai, G. A. *Journal of the American Chemical Society* **2009**, *131*, 9958.
(4) Yang, M.; Somorjai, G. A. *Journal of the American Chemical Society* **2004**, *126*, 7698.
(5) Yang, M.; Chou, K. C.; Somorjai, G. A. *Journal of Physical Chemistry B* **2003**, *107*, 5267.
(6) Bratlie, K. M.; Komvopoulos, K.; Somorjai, G. A. *The Journal of Physical Chemistry C* **2008**, *112*, 11865.
(7) Kliewer, C. J.; Aliaga, C.; Bieri, M.; Huang, W.; Tsung, C.-K.; Wood, J. B.; Komvopoulos, K.; Somorjai, G. A. *Journal of the American Chemical Society* **2010**, *132*, 13088.
(8) Bratlie, K. M.; Lee, H.; Komvopoulos, K.; Yang, P.; Somorjai, G. A. *Nano Letters* **2007**, *7*, 3097.
(9) Kuhn, J. N.; Huang, W.; Tsung, C.-K.; Zhang, Y.; Somorjai, G. A. *Journal of the American Chemical Society* **2008**, *130*, 14026.
(10) Somorjai, G. A.; Park, J. Y. *Journal of Chemical Physics* **2008**, *128*.
(11) Borodko, Y.; Humphrey, S. M.; Tilley, T. D.; Frei, H.; Somorjai, G. A. *Journal of Physical Chemistry C* **2007**, *111*, 6288.
(12) Ullah, M. H.; Chung, W. S.; Kim, I. *Small* **2006**.
(13) Kim, J.; Chou, K. C.; Somorjai, G. A. *Journal of Physical Chemistry B* **2003**, *107*, 1592.
(14) Ramirez, E.; Erads, L.; Philippot, K. *Advanced ,Ä¶* **2007**.
(15) Zheng, H.; Smith, R. K.; Jun, Y.; Kisielowski, C. *Science* **2009**.
(16) Su, X. C.; Kung, K.; Lahtinen, J.; Shen, R. Y.; Somorjai, G. A. *Catalysis Letters* **1998**, *54*, 9.
(17) Su, X. C.; Kung, K. Y.; Lahtinen, J.; Shen, Y. R.; Somorjai, G. A. *Journal of Molecular Catalysis a-Chemical* **1999**, *141*, 9.
(18) McCrea, K. R.; Somorjai, G. A. *Journal of Molecular Catalysis a-Chemical* **2000**, *163*, 43.
(19) Yang, M.; Somorjai, G. A. *Journal of Physical Chemistry B* **2004**, *108*, 4405.
(20) Yang, M. C.; Chou, K. C.; Somorjai, G. A. *Journal of Physical Chemistry B* **2004**, *108*, 14766.
(21) Kuhn, J. N.; Tsung, C. K.; Huang, W.; Somorjai, G. A. *Journal of Catalysis* **2009**, *265*, 209.
(22) Rioux, R. M.; Song, H.; Hoefelmeyer, J. D.; Yang, P.; Somorjai, G. A. *Journal of Physical Chemistry B* **2005**, *109*, 2192.

(23) Song, H.; Kim, F.; Connor, S.; Somorjai, G. A.; Yang, P. D. *Journal of Physical Chemistry B* **2005**, *109*, 188.
(24) Kweskin, S. J.; Rioux, R. M.; Habas, S. E.; Komvopoulos, K.; Yang, P.; Somorjai, G. A. *Journal of Physical Chemistry B* **2006**, *110*, 15920.
(25) Borodko, Y.; Habas, S. E.; Koebel, M.; Yang, P. D.; Frei, H.; Somorjai, G. A. *Journal of Physical Chemistry B* **2006**, *110*, 23052.
(26) Rumpel, A.; Novak, M.; Walter, J.; Braunschweig, B. *Langmuir* **2011**.
(27) Vig, J. R. **1986**.
(28) Aliaga, C.; Park, J. Y.; Yamada, Y.; Lee, H. S.; Tsung, C. K.; Yang, P. D.; Somorjai, G. A. *Journal of Physical Chemistry C* **2009**, *113*, 6150.
(29) Yang, M.; Chou, K. C.; Somorjai, G. A. *The Journal of Physical Chemistry B* **2004**, *108*, 14766.
(30) Kuhn, J. N.; Tsung, C.-K.; Huang, W.; Somorjai, G. A. *Journal of Catalysis* **2009**, *265*, 209.

Chapter 11

Conclusions and Future Work

12.1 Electronic Oxygen Activation by Charge Transfer from the Catalyst Support

This work implicates O as an electron acceptor that gives rise to charged reaction intermediates at the metal–support interface. This appears to be true for CO oxidation and methanol oxidation where electronic activation of surface O determines both the reaction rate and the product selectivity, respectively. Chapters 3 and 4 show that O can be electronically activated by an external bias applied across a metal–support interface in a solid-state device. Chapters 5–7 demonstrate that an exactly analogous effect is possible by n-type doping the support. The exact chemical nature of the electronically active O species is not yet clear. Initial attempts have been made to characterize this species in situ using ambient pressure x-ray photoelectron spectroscopy (XPS). However, it is possible that this charged species is short lived owing to its high chemical activity, and it may not be possible to directly observe this state without time resolved spectroscopy.

Chapter 3 shows that the history of a solid-state device in reaction conditions has an important effect on the ability of external bias to electronically activate the reaction intermediates. A correlation of the electronic activity of the catalytic device with the current–voltage curves obtained during reaction suggests that the CO oxidation reaction operates in different regimes depending on the nature of the catalyst and the O intermediate. On a CO covered Pt surface, the reaction follows a Langmuir–Hinshelwood mechanism where activation of the Pt–C bond in adsorbed CO for reaction with atomic O is rate limiting. In this case, electronic activation of O has little effect on the reaction kinetics. However, the Pt catalyst oxidizes during reaction, and that the Pt–O bond in the oxide is activated by electron density from the support. Electronic activation of O atoms in Pt oxide can be understood by considering the band structure of transition metal oxides where the valence band primarily represents bonding states and the conduction band primarily represents anti-bonding states with respect to the metal–O bond.[1] Consequently, electron transfer to the conduction band of Pt oxide will weaken the Pt–O bond resulting in a catalytic reaction involving an active O^- ion from the lattice in a Mars–van Krevelen type mechanism. Time-dependent kinetics are also observed in the case of CO oxidation on Pt using F-doped TiO_2 as an electronically active support (see Chapter 6, Fig. 4C). However, in this case in situ characterization of the catalyst is more challenging because there is no circuit for probing the electronic properties of the catalyst during reaction. In both cases electron spillover to the O occurs as a result of the electric field at the metal–support interface. This field can be enhanced by an externally applied bias (Chapters 3 and 4) or by n-type doping of the support to increase the intrinsic built-in potential (Chapters 5–7). In both cases, the charge transfer results in enhanced catalytic activity for oxidative chemistry.

The methanol oxidation reaction discussed in Chapter 7 is unique in these studies because it is a multipath reaction where electronic activation controls the catalyst selectivity rather than activity. These results strongly suggest that two separate (rather than sequential) pathways exist

for formaldehyde and CO_2 formation from methanol and that electronically activated O favors the formaldehyde pathway. There are relatively few catalysts capable of the selective oxidation of primary alcohols to aldehydes using molecular O_2, and H_2O_2 or other stoichiometric O donors are often used as the oxidant to increase reaction selectivity.[2] Of course, molecular O_2 is preferred for cost and environmental concerns. However, it was recently demonstrated that certain supported catalysts can produce formaldehydes from primary alcohols at high selectivity using O_2 as the oxidant.[3] These catalysts are also shown to be highly selective for H_2O_2 synthesis from H_2 and O_2.[4] In addition, it is known that halogen-induced electronic effects in Ag/AgO catalysts dramatically increase the activity for epoxidation chemistry.[5] Based on correlation of these studies with the present work on electronic activation of O, it appears that negatively charged O represents an important reaction intermediate that may be present on many partial oxidation catalysts.

The concept of electronic activation by control of catalyst electronic structure or by external control using a catalytic solid-state device is promising for a variety of important chemical applications. Electrochemical water splitting is an important reaction for energy conversion that may benefit from these findings. While H_2 evolution occurs at high rates near the thermodynamic efficiency limit, O_2 evolution requires a significant overpotential.[6,7] Presumably, a kinetic barrier to electron transfer limits the efficiency of this half reaction. Already studies using F-doped TiO_2 as a support for Pt catalysts show that the onset potential of electrochemical CO, methanol, and water oxidation reactions can be modified by controlling the electronic structure of the TiO_2 support. In addition, the ability to reduce the overpotential using an externally applied electric field could allow for fast reaction kinetics at near thermodynamic efficiencies and would represent a significant advance toward efficient chemical energy conversion. The concept of a catalytic field effect transistor is a promising idea for this application, and a patent is pending on this process.[8]

12.2 Strong Metal–Support Interactions and Acid–Base Chemistry

This work used sum frequency generation (SFG) vibrational spectroscopy to probe the molecular nature of strong metal–support interactions (SMSI). These results from Chapter 8 show that SMSI appears to be a special case of acid–base catalysis occurring at the oxide–metal interface. Hydrogenation of furfuraldehyde to furfural alcohol requires selective C=O bond activation that occurs by charge transfer between the furfuraldehyde molecule and O vacancies in a TiO_2 support. This gives rise to a furfuryl-oxy intermediate on the TiO_2 support that is observed by SFG. This active intermediate selectively hydrogenates to furfuryl alcohol by H spillover from supported Pt, and the Pt/TiO_2 catalyst is 90% selective for this reaction. The active furfuryl-oxy intermediate does not form on a SiO_2 support, and accordingly, kinetic measurements show that the Pt/SiO_2 catalyst does not produce any furfuryl alcohol. Recent results show that Pt/TiO_2 catalysts are also SMSI active for crotonaldehyde and acetaldehyde hydrogenation reactions to produce crotyl alcohol and ethanol, respectively.

In addition to direct observation of the active furfuryl-oxy intermediate, H spillover is also directly observed by SFG as an increase in the nonresonant signal intensity from a reducible support. The increase in nonresonant signal intensity on a Pt/TiO_2 catalyst is reversible in O_2 and appears to represent an in situ marker for the SMSI state of a catalyst as originally predicted by Tauster based on chemisorption measurements.[9] Recent kinetic measurements for

furfuraldehdye hydrogenation show that CeO_2 behaves similarly to TiO_2, while Al_2O_3, ZrO_2, Nb_2O_5, and WO_3 show no SMSI effect. Current work is in progress to correlate the SMSI activity of various supports with the nonresonant SFG intensity under reaction conditions and with the reducibility of the oxide in H_2 as probed by ambient pressure XPS.

These studies demonstrate that SMSI is a special case of acid–base catalysis that strongly affects C=O bond activation. An important application of C=O bond activation is Fischer–Tropsch synthesis for the conversion of CO to higher molecular weight hydrocarbons. When synthesis gas derived from steam reforming of methane is used as the feedstock for Fischer–Tropsch synthesis, the net process represents conversion of natural gas to liquid fuels and this process promises to have enormous economic and environmental impact in the current energy market. An even more challenging chemical process is CO_2 hydrogenation for renewable energy conversion. It has been proposed that acid catalysis is capable of achieving this lofty goal, and in light of this work, this idea is deserving of considerable attention.

12.3 The Role of an Organic Cap to Mediate Nanoparticle Catalysis

Inherent in colloidal nanoparticle synthesis is the presence of an organic capping agent to stabilize the size and shape of the nanoparticles. Recent research shows that the size and shape of catalytic nanoparticles provide control of reaction rate and selectivity for numerous catalytic reactions.[10-16] However, the effect of the organic cap on the catalytic behavior of the nanoparticles has not been well established. The capping agent is usually considered to act as a site blocking agent that lowers the metal surface area available for catalytic reaction. In this light, some have assumed that colloidal nanoparticles are incompatible for commercial catalytic applications because the presence of the organic cap decreases the apparent metal dispersion.

The studies discussed in Chapters 9 and 10 use SFG to probe the structure of poly(vinylpyrrolidone) (PVP) on Pt nanoparticles under reaction conditions. The results show that the capping agent is dynamic and disorders in H_2. When the PVP is removed, carbonaceous fragments continue to occupy the catalyst surface. This carbonaceous material is also dynamic and appears to control the catalytic activity of the Pt nanoparticles across several orders of magnitude. The carbonaceous fragments on the cleaned nanoparticles are porous in H_2 but collapse in O_2 to form a tightly closed shell. Consequently, removing the organic cap increases the activity for ethylene hydrogenation, but decreases the activity for methanol oxidation. This result suggests that for oxidation reactions the organic cap is desirable because it acts as a passivation layer against surface contamination but does not prevent catalysis. These findings highlight the important role of the organic cap to mediate nanoparticle catalysis and demonstrate one example where a capped nanoparticle is much more active than its cleaned analogue.

This work is reminiscent of homogenous catalysis where ligands are used to tune the activity and selectivity of single metal ions.[17] Recent work has also shown that active involvement by a dendrimer ligand allows small Pt clusters to function as homogenous reaction catalysts.[15] These results suggest that in the future the catalytic activity and selectivity of metal clusters and nanoparticles will be controlled by carefully selected capping agents in much the same way as homogenous and biological catalysis achieves high selectivity in complex reaction pathways using a framework of organic ligands. Other applications of this work include the design of capping agents to selectively block undesired reaction pathways. For example, coke

deposition currently limits the active lifetime of many hydrocarbon catalysts. Perhaps an appropriate capping agent would passivate the metal surface against coke deposition while still allowing high activity toward hydrocarbon conversion.[18]

12.4 References

(1) Cox, P. A. *Transition Metal Oxides An Introduction to their Electronic Structure and Properties*; Clarendon Press: Oxford, 1992.

(2) Sheldon, R. A.; Kochi, J. K. *Metal-catalyzed oxidations of organic compounds: mechanistic principles and synthetic methodology including biochemical processes*; Academic Press, 1981.

(3) Enache, D. I.; Edwards, J. K.; Landon, P.; Solsona-Espriu, B.; Carley, A. F.; Herzing, A. A.; Watanabe, M.; Kiely, C. J.; Knight, D. W.; Hutchings, G. J. *Science* **2006**, *311*, 362.

(4) Edwards, J. K.; Solsona, B. E.; Landon, P.; Carley, A. F.; Herzing, A.; Kiely, C. J.; Hutchings, G. J. *Journal of Catalysis* **2005**, *236*, 69.

(5) Lambert, R. M.; Cropley, R. L.; Husain, A.; Tikhov, M. S. *Chemical Communications* **2003**, 1184.

(6) Hall, D. E. *Journal of The Electrochemical Society* **1983**, *130*, 317.

(7) Lee, J.-W.; Popov, B. *Journal of Solid State Electrochemistry* **2007**, *11*, 1355.

(8) Baker, L. R.; Seo, H.; Hervier, A.; Somorjai, G. 2011.

(9) Tauster, S. J. *Accounts of Chemical Research* **1987**, *20*, 389.

(10) Bratlie, K. M.; Lee, H.; Komvopoulos, K.; Yang, P.; Somorjai, G. A. *Nano Letters* **2007**, *7*, 3097.

(11) Kuhn, J. N.; Huang, W.; Tsung, C.-K.; Zhang, Y.; Somorjai, G. A. *Journal of the American Chemical Society* **2008**, *130*, 14026.

(12) Grass, M.; Rioux, R.; Somorjai, G. *Catalysis Letters* **2009**, *128*, 1.

(13) Grass, M. E.; Joo, S. H.; Zhang, Y.; Somorjai, G. A. *The Journal of Physical Chemistry C* **2009**, *113*, 8616.

(14) Kliewer, C. J.; Aliaga, C.; Bieri, M.; Huang, W.; Tsung, C.-K.; Wood, J. B.; Komvopoulos, K.; Somorjai, G. A. *Journal of the American Chemical Society* **2010**, *132*, 13088.

(15) Witham, C. A.; Huang, W.; Tsung, C.-K.; Kuhn, J. N.; Somorjai, G. A.; Toste, F. D. *Nat Chem* **2010**, *2*, 36.

(16) Alayoglu, S.; Aliaga, C.; Sprung, C.; Somorjai, G. *Catalysis Letters* **2011**, *141*, 914.

(17) Gorin, D. J.; Sherry, B. D.; Toste, F. D. *Chemical Reviews* **2008**, *108*, 3351.

(18) Lu, J.; Fu, B.; Kung, M. C.; Xiao, G.; Elam, J. W.; Kung, H. H.; Stair, P. C. *Science* **2012**, *335*, 1205.